

A NOVEL ULTRA-LOW REFRACTIVE INDEX NANOPOROUS DIELECTRIC  
BASED AQUEOUS CORE LIGHT WAVEGUIDE SYSTEM

---

A Dissertation  
presented to the Faculty of the Graduate School  
University of Missouri-Columbia

---

In Partial Fulfillment  
of the Requirements for the Degree

Doctor Of Philosophy

---

by

VENUMADHAV KORAMPALLY  
Dr. Shubhra Gangopadhyay, Dissertation Supervisor

DECEMBER 2007

© Copyright by Venumadhav Korampally 2007

All Rights Reserved

The undersigned, appointed by the Dean of Graduate School,  
have examined the dissertation entitled

A NOVEL ULTRA-LOW REFRACTIVE INDEX NANOPOROUS DIELECTRIC  
BASED AQUEOUS CORE LIGHT WAVEGUIDE SYSTEM

Presented by Venumadhav Korampally

A candidate for the degree of Doctor of Philosophy

And hereby certify that in their opinion it is worthy of acceptance.

---

Dr. Shubhra Gangopadhyay (Advisor),  
Department of Electrical and Computer Engineering

---

Dr. Sheila A. Grant,  
Department of Biological Engineering

---

Dr. Fan Xudong  
Department of Biological Engineering

---

Dr. Lela K. Riley  
College of Veterinary medicine

---

Dr. Jae W. Kwon  
Department of Electrical Engineering

---

Dr. Mahmoud Almasri  
Department of Biological Engineering

## AKNOWLEDGEMENTS

I would like to express my sincere gratitude to my advisor Dr. Shubhra Gangopadhyay for her continued guidance, motivation and financial support during the course of this study. She was my main motivation to enter the Ph.D degree program, her energy and enthusiasm was what kept me pushing through the many obstacles during the study. I would like to extend my special thanks to Dr. Keshab Gangopadhyay for making me a part of their family.

I would like to thank Dr. Xudong (Sherman) Fan and Dr. Sheila Grant for their useful discussions and letting me use their laboratories freely. I would like to thank Dr. Lela Riley for providing me with laboratory facilities for the PCR project and her financial support. Special thanks go to Dr. Jae Kwon and Dr. Mahmoud Almasri for their friendly discussions. I would like to thank Dr. Jinglu Tan for his assistance and valuable discussions on the mathematical modeling of the PCR device.

This project would not have seen its success without the help of my colleagues Dr. Shantanu Bhattacharya for his assistance with the PCR project, Dr. Maslina Othman for all her help with the Ellipsometer data fitting, Dr. Maruf Hossain for his kind patience and help with all the deposition equipment and all my colleagues and friends from our research group. Special thanks go to Jasenka and all other members from Dr. Grant's research group who helped me on the various biological aspects of the project.

I would like to thank the staff of UM electron microscopy core, in particular Lou Ross, for their assistance in the TEM and SEM sample preparations and imaging. My

sincere thanks go to all my friends for being there for me in times of struggle and for their continued support.

Last but not the least; I would like to thank my parents and my sister for believing in me and for their constant encouragement. Their love, patience and understanding will be cherished for the rest of my life. I would finally thank NIH and NPB for their funding support.

# TABLE OF CONTENTS

Acknowledgements.....	ii
List of Figures.....	vi
List of Tables .....	ix
Abbreviations.....	x
Abstract.....	xii
<b>CHAPTER 1: Introduction and Motivation .....</b>	<b>1</b>
1.1 Introduction.....	1
1.2 Optical Sensors .....	2
1.2.1 Fluorescence Resonance Energy Transfer (FRET).....	3
1.2.2 FRET based biosensors.....	5
1.3 Liquid core waveguides .....	7
1.3.1 Losses in a waveguide .....	9
1.3.2 The liquid core waveguides .....	12
1.4 Liquid core optical waveguides with nanoporous dielectric cladding -The Motivation.....	14
1.5 Organization of the dissertation.....	16
<b>CHAPTER 2: Nanoporous Dielectrics.....</b>	<b>18</b>
2.1 Introduction.....	18
2.2 Ordered nanoporous silica (ONPS) .....	19
2.2.1 Sol – Gel chemistry.....	22
2.2.2 Sol-gel chemistry for Ordered Nanoporous Silica structures .....	23
2.3 Nanoporous dielectrics by sacrificial porogen approach.....	25
2.4 Silica Nanoparticles based thin films as nanoporous dielectrics .....	29
2.4.1 Rapid formation of Ultra low – refractive index nanoporous dielectric films based on PMSSQ nanoparticles.....	29
2.5 Experimental.....	33
2.5.1 Preparation of the Ordered Nanoporous silica films.....	33
2.5.2 Nanoporous dielectric films through sacrificial porogen approach.....	34
2.5.3 PMSSQ nanoparticles based Nanoporous dielectrics.....	34
<b>CHAPTER 3: Device design and fabrication physical channel Design.....</b>	<b>36</b>
3.1 Device design.....	36
3.2 Device fabrication.....	37

3.2.1	Fabrication of channels in Silicon.....	37
3.2.2	Nanoporous Dielectric cladding .....	43
3.2.3	Bonding of NPS coated channels and glass.....	44
3.2.4	Fabrication of the whole device.....	47
3.3	Drawbacks of the current design.....	48
<b>CHAPTER 4:</b>	<b>Device design and fabrication virtual channel design .....</b>	<b>53</b>
4.1	Improved design.....	53
4.1.1	Description of the new design.....	54
4.1.2	Design considerations.....	56
4.1.3	Device fabrication.....	61
<b>CHAPTER 5:</b>	<b>Results and Discussion .....</b>	<b>69</b>
5.1	Overview.....	69
5.2	Nanoporous dielectrics.....	70
5.2.1	Ordered Nanoporous silica (ONPS) films .....	70
5.2.2	Nanoporous dielectric films through sacrificial porogen approach.....	72
5.2.3	PMSSQ nanoparticles based Nanoporous dielectrics.....	73
5.2.4	Liquid Core waveguide characterization .....	86
<b>CHAPTER 6:</b>	<b>Conclusions and future research .....</b>	<b>91</b>
6.1	Conclusions.....	91
6.2	Future research.....	92
6.2.1	Nanoparticle research.....	92
6.2.2	Further improvements in LCW.....	94
<b>CHAPTER 7:</b>	<b>Optimization of fabrication process for a PDMS-SOG-Silicon based PCR Micro Chip through system identification techniques .....</b>	<b>95</b>
7.1	Abstract.....	95
7.2	Introduction.....	95
7.3	Device details.....	97
7.3.1	Integration of the RTD.....	98
7.3.2	PCR Runs.....	101
7.4	Parametric identification of the System.....	102
7.4.1	Design of the perturbation signal.....	103
7.4.2	Identification of the model parameters .....	106
7.5	Results and discussion .....	106
7.5.1	Reduction of fabrication complexity .....	108
7.6	Conclusions and Future work .....	109
References.....		110
Vita.....		117

## List of Figures

Figure 1-1. The electromagnetic spectrum, adapted from W. J. Kaufmann, "Universe", [Freeman:New York].)	2
Figure 1-2 Jablonski diagram for resonance energy transfer mechanism. Obtained from <a href="http://www.olympusfluoview.com/applications/fretintro.html">http://www.olympusfluoview.com/applications/fretintro.html</a>	4
Figure 1-3. Principle underlying a typical FRET based biosensor [4]	6
Figure 1-4. Illustration of the light ray at the interface of two dielectric materials with different indices of refraction.	7
Figure 1-5. Light guiding through an optical waveguide	8
Figure 1-6. BeamProp simulation of a waveguide. a. good interface between core – cladding, b. roughness of $\pm 3\mu\text{m}$ roughness at the interface.	10
Figure 1-7. Illustration of the evanescent field. Note that it decays exponentially into the cladding material given by Eqn 1-5	11
Figure 2-1 Surfactant molecules in solution at different concentrations a. single surfactant molecule, b. surfactant molecules at low concentrations, c. surfactant molecules at the critical micellar concentration d. the cylindrical phase e. the hexagonal phase.	20
Figure 2-2. The different reactions occurring in a Sol-gel process.	23
Figure 2-3. a. Illustration of the Dip coating process.	25
Figure 2-4 Procedure for the preparation of a Nanoporous dielectric film using Polymethyl Silsesquioxane as the matrix material and EA-PPI-64 as the porogen [33].	28
Figure 2-5 a. the closed pore and b. the open pore structures for the nanoporous dielectric films by porogen approach.	29
Figure 2-6 Illustration of the PMSSQ nanoparticle dispersion formation mechanism.	32
Figure 3-1. Conceptual design of the microfabricated liquid core waveguide system	37
Figure 3-2. Process flow diagram for the etching of microchannels in silicon	39
Figure 3-3. Typical channel mask. the mask is designed to have two different channel widths. Channel widths of 400 microns and 200 microns were considered in this study.	40
Figure 3-4. Anisotropic etch profile of the channels obtained by KOH wet chemical etching.	42
Figure 3-5. Schematic of the Anodic bonding process	45
Figure 3-6. Picture of the ONPS coated borosilicate glass bonded to a silicon substrate by the anodic bonding technique	47
Figure 3-7. Fabrication of the complete Liquid core waveguide system.	48
Figure 3-8. SEM of the channel cross sections showing the non-uniform nature of the NPO coating obtained by spin coating.	51
Figure 4-1. Illustration of the confinement of the liquid column by ‘virtual channels’	55
Figure 4-2. Cross section view of the conceptual design of the liquid core waveguide	55
Figure 4-3. Forces acting on the liquid surface at the entrance of the hydrophobic region. The spacing between the substrates is ‘h’ and the width of the hydrophobic region is ‘a’	56

Figure 4-4. a. Illustrates the curvature of the liquid column confined within the hydrophilic regions b. the top view of the straight column suggesting the other principle radii $R_2$ to be $\infty$ .	58
Figure 4-5. a. Top view and b. cross sectional view of the single port device illustrating the wetting of the hydrophobic regions by water due to the surface tension forces from the virtual walls of the liquid column within the substrates.	60
Figure 4-6. Teflon pattern obtained by photoresist coating on Teflon, patterning and Teflon etching showing the unintended protrusions in the straight channels.	61
Figure 4-7. Mask design for patterning Channels on a. Silicon substrates, b. Glass substrates.	64
Figure 4-8. Fabrication flow chart for the new LCW design.	66
Figure 4-9 a Picture of the final device with PDMS spacers b. picture of the device with DI water filled channels.	68
Figure 5-1 Planar and cross sectional TEM images of the a ,b spin coated and c,d,e the Dip coated ONPS films.	70
Figure 5-2. SEM pictures of ONPS coating in the channels a. cracking in the channels, b. delamination of the films from the channels.	72
Figure 5-3. Contact angles made by the water droplet on the deposited film after various thermal treatments a. As is film (without any high temperature annealing, the film was baked at 80 C to evaporate the solvent) b. After 200 C treatment for 45 mins. c. After 300 C treatment for 45 mins.	73
Figure 5-4. High resolution SEM picture of the obtained nanoporous PMSSQ particulate based film.	74
Figure 5-5. Results of the nanoindentation test on the films.	75
Figure 5-6 C-V curves for the Nanoporous dielectric MIM structures at two different frequencies on dot1 (500 micron diameter).	77
Figure 5-7. Contact angle picture of a water droplet on the a. As prepared NPS surface showing that the surface is hydrophobic b. Aluminum surface treated NPS.	78
Figure 5-8. ATR-FTIR spectra of the NPS films after various surface treatments	79
Figure 5-9. Surface functionalization to obtain –SH functionality a. Untreated surface with predominant hydroxyl groups, b. MPTMS treated substrate.	81
Figure 5-10. Experimental set-up for the measurement of fluorescence from the protein A/AF546 tagged substrates	83
Figure 5-11. Fluorescence emission spectra of Immobilized protein A/AF546 on a. NPO coated and uncoated glass substrates (note that there is a thin coating of amorphous silicon ~ 4nm thick between the glass and the NPO layer) b. NPO Coated and uncoated Si substrates	84
Figure 5-12. Cross sectional view of a channel etched in silicon and coated with the PMSSQ nanoparticle based nanoporous dielectric.	85
Figure 5-13. Experimental setup for loss characterization of the liquid core waveguide.	87
Figure 5-14 Arrangement of the LCW device for loss characterization.	88
Figure 5-15. Waveguide loss characterization plot – Design 1	89
Figure 5-16. Illustration of the waveguiding effect. The illumination of the channels was performed transversally and the light source was moved across the width of the device from right to left traversing three liquid columns in the process.	90
Figure 5-17. Waveguide loss characterization plot – Design 2	90

Figure 6-1. Dye incorporated organosilicate nanoparticles a. scraped from films treated to 150 C for 5 hrs, b. gelled solution.....	92
Figure 6-2. TEM image of organosilicate nanorods.....	93
Figure 7-1. Schematic of the device, b. cross-sectional view of the device. ....	98
Figure 7-2. Mask design for the RTD.....	99
Figure 7-3. RTD calibration curve in arrangement 3.....	100
Figure 7-4. Schematic for the 4-wire measurement.....	101
Figure 7-5. Results of the PCR amplifications a. 1:1 sample, b. 100,000:1 sample.....	102
Figure 7-6. Temperature responses to different voltage steps. At each voltage step, the temperature of the chamber lies above the temperature of the heater. ....	103
Figure 7-7. Step response with an input voltage step of 7.5 V for the heater and chamber temperature and the corresponding curve fits.....	104
Figure 7-8. Circuit diagram for the experimental set up.....	105
Figure 7-9. PRBS temperature response of the heater side and the chamber side.....	106
Figure 7-10. Plot of the simulated response with second order model and fourth order model and the experimental data .....	107
Figure 7-11. Plot of the predicted and the measured chamber temperature values .....	108

## List of Tables

Table 5-1 Refractive index and thickness of films with and without adhesion layer .....	80
Table 7-1. Curve fit parameters .....	104

## Abbreviations

ARX- Auto regressive with exogenous inputs

ATR-FTIR- Attenuated total reflection fourier transform infrared spectroscopy

BSA- Bovine serum albumin

CMC- Critical Micellar concentration

CTAB- Cetyltrimethyl ammonium hydroxide

CV- Capacitance-Voltage

DMF- N,N-Dimethylformamide

DNA- Deoxyribonucleic acid

FRET-Fluorescence resonance energy transfer

FTIR- Fourier transform infrared spectroscopy

FTR- Frustrated total internal reflection

GMBS- N-(g-Maleimidobutyryloxy)succinimide ester

IBR- Infectious Bovine Rhinotracheitis

IPA- Isopropyl alcohol

LCW- Liquid core waveguide

MEMS- Micro electro mechanical systems

MIM- Metal-Insulator-Metal

MPTMS- Mercaptopropyl trimethoxy Silane

MSE- Mean squared error

NA- Numerical aperture

NPO- Nanoporous organosilicate

NPS- Nanoporous silica

ONPS- Ordered nanoporous silica

PBS- Phosphate buffered saline

PCR- Polymerase chain reaction

PDMS- Polydimethylsiloxane

PECVD- Plasma enhanced chemical vapor deposition

PM Acetate- Propylene Glycol methyl ether acetate

PMSSQ – Poly(methylsilsesquioxane)

PPG-Polypropylene Glycol

PRBS- Pseudo – random – binary sequence

PTFE- Poly tetrafluoroethane

RC- Resistance capacitance

RTD- Resistance temperature detector

SEM- Scanning Electron microscopy

SOG- Spin on glass

TEOS- Tetraethoxysilane

UV-Vis- Ultra Violet-Visible spectroscopy

VASE- Variable angle spectroscopic Ellipsometry

## **ABSTRACT**

### **A NOVEL ULTRA-LOW REFRACTIVE INDEX NANOPOROUS DIELECTRIC BASED ACQUEOUS CORE LIGHT WAVEGUIDE SYSTEM**

This dissertation presents the fabrication of an on-chip waveguide system capable of guiding light through aqueous solutions. The waveguide relies on total internal reflection for light propagation wherein the core of the waveguide consists of the aqueous solution and the cladding is formed by an ultra low refractive index nanoporous dielectric coating. Such waveguides are of great interest in biosensor design as water is the natural medium for any biological processes.

In this dissertation, three types of nanoporous dielectric films have been considered – the ordered nanoporous silica, nanoporous organosilicate films through porogen extraction and organosilicate nanoparticles based nanoporous films. The organosilicate nanoparticle based films have been developed during the course of this research and these films offer superior properties with respect to formation of crack free films and ultra low refractive index. The hydrophobic nature of the films requires no further surface modification in order to be applied as the cladding material for the aqueous core waveguide system. Because of their unique morphology, these films feature a large surface area and the mechanical strength of these films is higher than similar porosity films formed by porogen extraction. A hypothetical formation mechanism is described for the formation of these films.

Two types of liquid core waveguide designs are considered. In the first design, physical channels are etched in silicon substrates for liquid containment. Low refractive

index nanoporous dielectric coatings are deposited in the channels through dip/spin coating techniques. The channels are sealed with a nanoporous dielectric coated glass substrate to form the final device. The presence of surface structures in the substrate presented unique fabrication challenges for the integration of the nanoporous dielectrics. The fabrication challenges are presented along with the description and remedy.

An improved design of the liquid core waveguide is described to overcome the drawbacks of the first design. In the improved design, the requirements of physical channels are eliminated by exploiting the surface tension and capillarity properties of fluids confined to small volumes. Both the designs have been tested for waveguide performance. The waveguide losses have been greatly reduced in the improved design. The fabrication methodology employed is compatible with the standard microfabrication techniques allowing scope for mass production. In addition to these, the waveguide is designed so as to allow easy cleaning to be applied as a reusable system.

# **CHAPTER 1: INTRODUCTION AND MOTIVATION**

## **1.1 Introduction**

Life as we see it is the result of interaction of light with matter. The beautiful colors in the fall, the rainbows, and the blue sky are but some of the examples of the complex interactions taking place between light and matter at the molecular level. Our very existence depends on light as light is the primary source of energy for the universe. Thus the subject of light and its interaction with matter has interested scientists and philosophers alike and has been a topic of study for many centuries. It still is a widely pursued research area. With new experimental evidences and developments in the electromagnetic theory, by the end of the 19<sup>th</sup> century, a new perspective in the understanding of light has been formulated. Light no longer was simply seen as a ray of tiny particles (corpuscles) but looked upon with reverence as a wave.

Light was thus considered a form of an electromagnetic radiation. Electromagnetic radiations exist over a wide range of frequencies, the collection of which is called the electromagnetic spectrum. Depending on the different types of interactions with matter, the electromagnetic spectrum is subdivided into different regions. Figure 1-1 illustrates the electromagnetic spectrum and its various regions.

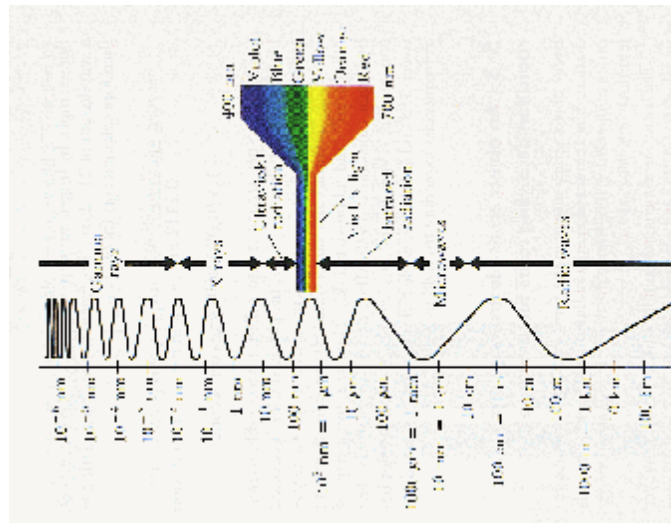


**Figure 1-1. The electromagnetic spectrum, adapted from W. J. Kaufmann, "Universe", [Freeman:New York].)**

While most commonly observed phenomenon: reflection, refraction interference, polarization could be explained by the wave theory of light, the theory nevertheless had its limitations. For instance, it could not explain the phenomenon of photoelectric effect which suggested a particle nature of light. The quantum theory of light was formed in the last century to account for it which is based on the duality of light. This theory considers light both as waves as well as a stream of mass-less particles, known as “photons”[1]. The dual nature cast new light on the ‘light – matter’ interactions providing answers to some of the previous anomalies.

## 1.2 Optical Sensors

As we have seen in the previous sections, the interaction of light with matter can have some unique implications. Different molecules interact differently with light thus a unique signature of the molecule itself can be obtained. Such aspects have been well exploited to design optical based sensors for use as bio or chemical detection. In the

recent years, research and development of highly target-specific biosensors has attained a level of paramount importance because of the increasing need for applications in national security, health care, the environment, energy, food safety, and manufacturing. Of the different transduction methods available, fluorescence based sensing is the most common method employed in the biosensor design. These sensors rely on the fluorescence resonance energy transfer (FRET) phenomenon between molecules described in detail below.

### **1.2.1 Fluorescence Resonance Energy Transfer (FRET)**

Fluorescence resonance energy transfer (FRET) is a radiationless transfer of energy from a donor fluorophore to an acceptor Fluorophore in close proximity [2]. Fluorophore can be defined as the component of a molecule which causes the molecule to be fluorescent [3]. FRET manifests as the quenching of the donor and an increased acceptor emission. The distance between the donor and the acceptor Fluorophores play an important role in determining the FRET efficiency [3]. The range over which efficient energy transfer takes place is extremely sensitive to the distance between the donor and the acceptor Fluorophores and is limited to approximately 10nm. This aspect of FRET has important applications in studying molecular interactions.

In addition to the distance constraints, there are many other factors that influence the efficiency and the transfer rate of FRET. The extent of overlap of the donor emission with the absorption spectra of the acceptor, the donor fluorescence life time [3] are some of the other important factors influencing the FRET activity. The donor fluorescence life time has to be long enough for the even to occur. Figure 1-2 gives the Jablonski diagram for the resonance energy transfer

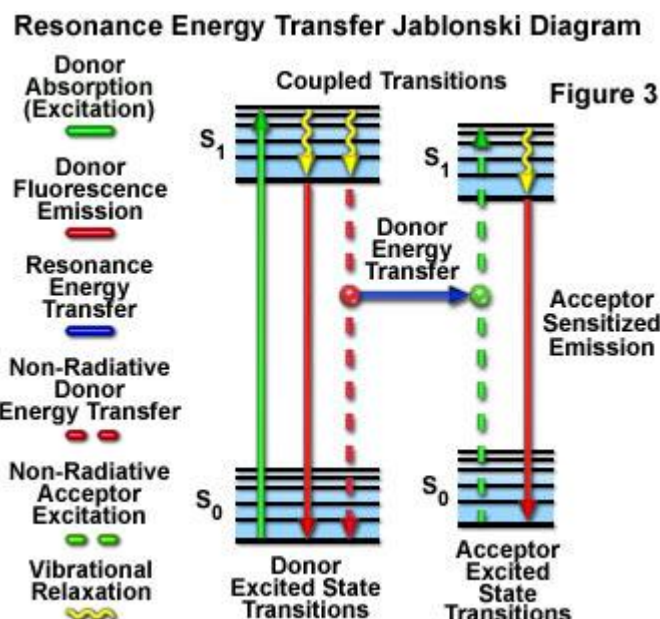


Figure 1-2 Jablonski diagram for resonance energy transfer mechanism. Obtained from <http://www.olympusfluoview.com/applications/fretintro.html>

The theory of FRET was initially proposed by Theodor Förster in the late 1940s which described the molecular interactions leading to FRET. Long range dipole intermolecular couplings between the donor and the acceptor are said to be the cause for the energy transfer. The equations governing the energy transfer rate during a FRET activity is given below:

$$K_T = \left(\frac{1}{t_D}\right) \cdot \left[\frac{R_0}{r}\right]^6 \quad 1-1$$

Where  $K_T$  is the energy transfer rate,  $t_D$  is the donor lifetime in the absence of the acceptor,  $r$  is the distance between the donor and the acceptor molecules.  $R_0$  is called the Förster critical distance or in other words the maximum separation distance between the donor and the acceptor for FRET to still occur. This value depends on variety of factors which includes the extent of overlap between the donor emission and the acceptor

absorption spectra, relative molecular orientations between the donor and the acceptor and the refractive index of the medium.

Because of the extremely sensitive distance dependence, FRET based techniques have found applications ranging from fluorescence microscopy to studying different molecular interactions and conformational changes occurring in proteins. We shall however limit the application of FRET techniques to the biosensor design for further discussions.

### **1.2.2 FRET based biosensors**

The underlying principle in most of the FRET based biosensors that have been reported is based on the conformational changes that occur during the antigen – antibody bindings. Typically, the antibody and the antigen molecules are labeled with the donor and the acceptors molecules that can exhibit FRET behavior when within the Förster distance. The donor molecules are then excited and the fluorescence response captured. If there indeed is binding between the antigens and the antibody, the conformational changes that occur brings the labeled donor – acceptor molecules into close proximity thereby inducing FRET. Figure 1-3 illustrates a typical FRET based biosensor.

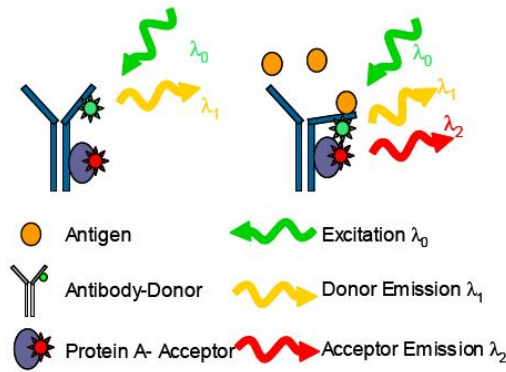


**Figure 1-3. Principle underlying a typical FRET based biosensor [4]**

As can be seen from Figure 1-3 the increased acceptor emission at the detection output would be an indicator of the antibody – antigen binding.

Pierce *et. al* reported a FRET based biosensor for the early detection of myocardial infarction [4]. In their biosensor design, the Fluorophores were conjugated to an antibody – Protein A complex and then immobilized onto the distal end of an optical fiber. The excitation of the donor Fluorophores was done with the optical fiber. Ko *et. al* reported a similar biosensor design for the rapid detection of *Salmonella typhimurum* [5]. Chew *et. al* reported a FRET based biosensor which could reveal the transient and regional myosin light chain kinase activation in lamella and cleavage furrows [6]. Juntao *et. al* reported a FRET based biosensor to detect the changes caused by viral protein-receptor binding [7]. In all these reported literatures, the biosensing is performed in an aqueous medium. The external excitation to the donor molecules is done via the evanescent field coupling from the optical fiber [4,5] or a solid core waveguide.

As we have seen above, the natural environment for bio molecules is an aqueous medium. Thus using aqueous medium as the core of a waveguide, especially for optical based sensing eliminates the need for additional bulk optics or expensive microscopes.

Signal to noise ratio will be greatly enhanced as the generated fluorescence signal is contained within the channel and coupled to the output detection system with minimal loss.

### 1.3 Liquid core waveguides

A waveguide in the simplest terms can be defined as a structure for guiding a wave from one point in space to the other with minimal loss. There are different kinds of waveguides; its structure depends on the type of wave that needs to be guided. We will be concerning ourselves with light waveguides as we are interested in optical based sensors. The most common design for these waveguides consist of a dielectric material with high refractive index (core) surrounded by a material of lower index of refraction (cladding). Light is guided in the core by means of total internal reflection.

Snell's law states that when a beam of light propagating in a medium (with refractive index  $n_1$ ) is incident on another medium (with a refractive index  $n_2$ ) the angles of incidence and refraction at the interface are related to each other by the expression

$$n_1 \sin \theta_1 = n_2 \sin \theta_2 \text{ (see Figure 1-4)} \quad 1-2$$

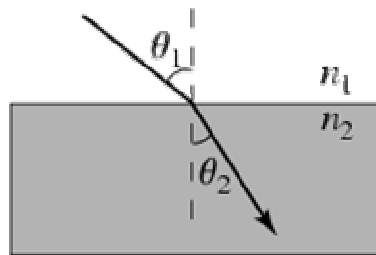


**Figure 1-4. Illustration of the light ray at the interface of two dielectric materials with different indices of refraction.**

Where  $q_1$  is called the incident angle and  $q_2$  the angle of refraction angle. The critical angle is defined as that value of the incident angle for which the angle of refraction is  $90^\circ$ . Hence from equation 2,  $q_1$  can be calculated as

$$q_1 = \sin^{-1}\left(\frac{n_2}{n_1}\right) \quad 1-3$$

Equation 3 further puts the constraint on the relative refractive indices of the two medium in order to obtain a solution for  $q_1$ . The refractive index of medium 2 ( $n_2$ ) should be lower than the refractive index of medium 1 ( $n_1$ ). For all angles greater than the critical angle, the light ray is said to be total internally reflected. These aspects of the laws of refraction have been exploited in the design of an optical waveguides. The most common form of an optical waveguide is an optical fiber. Figure 1-5 Illustrates an optical waveguide design. The most common form of the optical waveguide is an optical fiber.

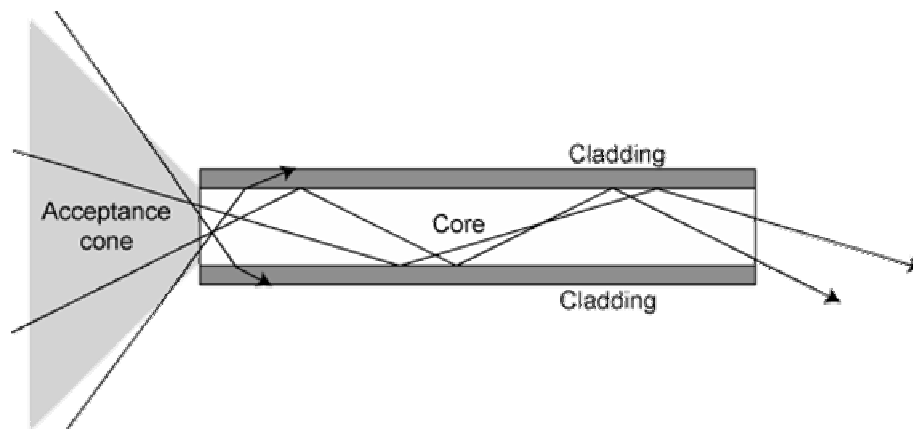


**Figure 1-5. Light guiding through an optical waveguide**

The refractive index contrast between the core and the cladding determines the acceptance angle cone for the light beam. Rays that approach the waveguide with angles within the acceptance cone are guided through the waveguide, while those with angles

greater than the acceptance cone are reflected. Acceptance cone is normally reported as numerical aperture (NA) for a waveguide which is defined as

$$NA = \sqrt{n_{core}^2 - n_{clad}^2} \quad 1-4$$

### 1.3.1 Losses in a waveguide

Careful consideration has to be made in the design of the waveguide system so as to minimize the losses during light guiding.

#### *Choice of core material*

The choice of the core material itself plays an important role. As we have seen in section (About absorption), different materials have different absorption spectra. The material of choice for the core of the waveguide ideally should have 100 percent transmission across the whole light spectrum. However, it is practically not feasible to achieve this so the choice of the core material depends on the specific application and what wavelengths of light that are being transmitted. Cost issues also influence the choice of core material.

#### *Interface between the core – cladding*

The interface between the core and cladding is another important factor which effects the light guiding properties of the waveguide. Surface roughness at the core – cladding interface would result in light scattering and eventual loss during light guiding. Figure 1-6 illustrates the loss due to a bad core – cladding interface in a waveguide.

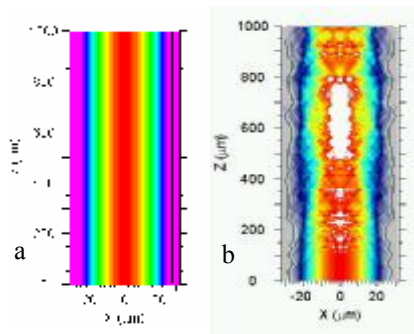


**Figure 1-6. BeamProp simulation of a waveguide. a. good interface between core – cladding, b. roughness of ± 3mm roughness at the interface.**

*Thickness of the cladding material*

Concept of the evanescent field

We have already seen that Light is a form of an electromagnetic radiation. A propagating light wave sets up electric and magnetic fields in the medium of propagation. Maxwell's equation states that the electric and magnetic fields cannot be discontinuous at the interface of two dielectric materials. In the case of total internal reflection, the simple ray model introduces the discontinuities in electric and magnetic fields at the interface of the core and the cladding. Therefore in order to satisfy the boundary conditions due to Maxwell's equations and the law of conservation of momentum, there has to be a matching field on the far side (the cladding). It has been shown that, there indeed is an exponentially decaying field that is established on the far side with a penetration depth given by

$$d = \frac{\lambda}{2p \sqrt{n_{core}^2 \sin^2(q_i) - n_{clad}^2}} \quad 1-5$$

Where 'd' is the penetration depth of the decaying field, 'λ' is the wavelength of the incident light, and 'q<sub>i</sub>' the angle of incidence. It has to be noted that even with the

presence of the evanescent field during the total internal reflection, the reflected wave has the same energy as the incident wave. Therefore, no net transfer of energy across the interface occurs unless another dense medium is brought in close proximity to the interface [8].

When a medium of higher refractive index (than the cladding material) is brought into the proximity of the evanescent field, a phenomenon called frustrated total internal reflection (FTR) takes place. For FTR to take place, the third medium should have a refractive index such that the light (within the acceptance cone determined by the core-cladding refractive indices) would not undergo a total internal reflection when the core and the third medium is placed in direct contact. The evanescent field will then escape into the third medium exciting propagating fields in the third medium thus perturbing the total internal reflection in the core.

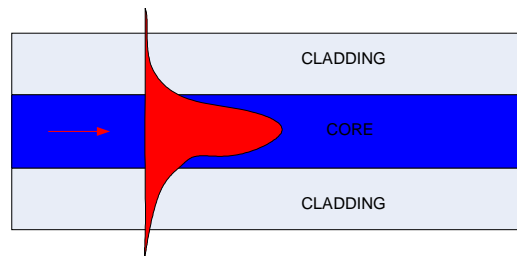


**Figure 1-7. Illustration of the evanescent field. Note that it decays exponentially into the cladding**

material given by Eqn 
$$d = \frac{l}{2p \sqrt{n_{core}^2 \sin^2(q_i) - n_{clad}^2}}$$
 1-5

Thus the thickness of the cladding material plays an important factor in the design of the waveguide system. In order to minimize the leakage of light from the core via FTIR, the waveguide has to be designed to have a cladding thickness greater than the evanescent wave penetration depth.

### **1.3.2 The liquid core waveguides**

#### *A Historical perspective*

Liquid core waveguide as the name suggests is an optical waveguide with a liquid medium as the core. The first scientific study of light guiding in liquids was done in the 19th century when Colladon, Babinet, Tyndall, and others investigated light propagation by total internal reflection in streams of water [9]. These waveguides were initially considered for optical communications before the arrival of the optical fibers. Small diameter glass tubes filled with high refractive index liquids were developed for this purpose. However, with the advent of the optical fiber technology, which offered low loss solid core optical fibers coupled with easy handling capabilities, the liquid core waveguides for communication purposes died a natural death.

The unavailability of suitable cladding materials put a huge constraint on the choice of the liquid to be considered as a core. Glass capillaries were considered for the waveguides which had a refractive index of  $n \geq 1.46$ . The waveguiding in the case of glass capillaries filled with liquid happened at the glass-air interface. Although these waveguides were reported to have a relatively low loss lying between 18 and 8dB/m [10], there were many disadvantages associated with using them. As the guiding was done at the air-glass interface, the glass surface had to be kept optically clean [9] to avoid any scattering based losses from the surface of the capillary tube. The dimensions of the capillary wall had to be significantly lower than the core diameter so as to confine the dominant modes of propagation in the liquid core making these capillaries extremely fragile to handle. Thus the choice of liquids was limited to those having a refractive index greater than that of water (1.33). Waveguides which are based on highly reflective

surfaces have also been considered for the liquid core waveguide design. Glass capillaries coated with metallic coatings to act as reflecting surfaces or glass capillaries externally coated with metal surface were studied. As these waveguides do not depend on the refractive indices, these designs could accept light over a very large solid angle. Such waveguides have been used successfully in the microwave and infrared regions for visible absorbance spectroscopy [11]. However, these waveguides have reported to have large losses and were rendered unsuitable for fluorescence collection and Raman applications [12]. Long path length waveguides could not be constructed with this arrangement owing to the large attenuation in a very short distance. Losses as high as 250 dB/m were reported for capillaries externally coated with silver filled with water [10]. In addition to these, the possibility of tarnishing of the metallic coatings by the liquids of interest is always present which would eventually ruin the waveguiding properties of the system. For externally metallized glass/quartz tubes, this aspect of metal tarnishing is reduced; however the attenuation is even higher.

Although liquid core waveguides were never put to use for optical communications, these waveguides show a great promise in various optical spectroscopic methods. For example, we have already seen in the previous section about the feasibility of using such waveguides as fluorescence based biosensors. With the development of a new class of polymeric materials of the class tetraFluoroethane (PTFE) – type Teflon and amorphous Fluoropolymer (Teflon AF 2400) with lower refractive indices than water, interest in aqueous core waveguides have once again picked up. Teflon AF 2400 has been reported to have a refractive index of  $n = 1.29$  which was the lowest reported

refractive index for any known polymer. Use of liquid core waveguides based on these polymeric materials for Raman spectroscopy has already been demonstrated [13,14].

Teflon tubes [9,15,16] or glass capillaries internally/externally coated with Teflon [17,18] were used for various spectroscopic applications. With a surge of interest in the MEMS based lab-on-chip devices, many attempts in the microfabrication of Teflon AF based liquid core waveguides have been made. Datta et. al reports a microfabricated Teflon AF based liquid core waveguide system which is formed by etching channels in silicon followed by coating and bonding them with Teflon AF 2400 coated glass substrates [19]. Manor et. al reports a similar microfabrication design with channels formed in soda lime glass [20].

#### **1.4 Liquid core optical waveguides with nanoporous dielectric cladding - The Motivation**

Although Teflon has established itself as a versatile material for LCW design, it is not the ideal material, especially in applications in fluorescence based biosensor design and Raman spectroscopy. Teflon offers little chance for chemical functionalization desired in most biosensing applications. The refractive index contrast between Teflon and water is at most 0.04 which translates to an acceptance angle of just  $18^\circ$ . For applications in biosensors and Raman based chemical sensors, this poses a big limitation. As the fluorescence is generated in all directions within the waveguide, it is advantageous for the waveguide to have a large acceptance cone thus guiding most of the generated fluorescence through the length of the waveguide.

Thus for a more efficient liquid core waveguide bio/chemical sensor, new materials with ultra low refractive indices have to be engineered. Nanoporous silica is one such

material which would be an ideal choice as the cladding material. With pores in the order of 2 – 4 nm diameters, these materials have an extremely low refractive index. Refractive index as low as 1.15 has been reported [21] which correspond to an acceptance angle of  $42^\circ$ . These dielectric materials have excellent adhesion to the common substrates and easy functionalization of these surfaces with well established methods makes them all the more attractive for biosensor applications. The feasibility of using nanoporous dielectric as low-index cladding material for aqueous core planar waveguides has already been demonstrated by Risk et. al [212]. In their experiments, two fused silica substrates coated with nanoporous dielectric (0.8  $\mu\text{m}$  thick) were held facing each other, separated by 50  $\mu\text{m}$  thick polyester spacing. The space between the two substrates was filled with an aqueous solution containing fluorescent beads. Waveguide loss characterization for the set-up was done by transversely illuminating the aqueous core with the excitation signal. Fluorescence was collected at the edge of the waveguide by coupling an optical fiber connected to a spectrometer. A waveguide loss of 0.55 – 0.56 dB/mm has been reported.

Exploiting the properties of nanoporous dielectric in the design of the liquid core waveguides is the motivation behind this project. No compact microfabricated system employing nanoporous silica has been reported till date. Thus the attractive properties of the nanoporous dielectric combined with the massive multiplexing capability provided by the MEMS based technologies would result in novel and cost effective sensors. The aim of this project is to fabricate such a sensor with extreme sensitivity and at the same time which is suitable for mass production.

## **1.5 Organization of the dissertation**

In the present dissertation, the work has been focused on the integration of nanoporous dielectric films in liquid core waveguide designs. Two designs of the liquid core waveguide are considered. The material aspects with regards to the preparation and characterization of nanoporous dielectric films are presented in chapter 2. A brief literature review on the development of nanoporous silica dielectric, different coatings methods to apply them on to substrates will be discussed. A new method of formation of nanoporous dielectric films based on organosilicate nanoparticles is presented with a possible hypothetical formation model.

Chapter 3 describes the design and fabrication aspects of the ‘physical channel’ design of the liquid core waveguide. The problems encountered and the drawbacks of this design are stated. This chapter especially deals with the challenges of integrating nanoporous dielectric films with MEMS fabrication techniques.

Chapter 4 presents an improved design of the liquid core waveguide system based on ‘virtual channels’ for liquid containment. Equations governing the virtual channels with regards to conditions for no flow, virtual channel rupture are derived. Various design considerations that have to be met for the LCW system to function are presented. Fabrication flow chart for this design is also included in this chapter.

Chapter 5 presents the results and discussion obtained from this research. Results obtained from the nanoporous dielectrics and the integration problems to the LCW are presented. Nanoporous organosilicate nanoparticles based films are probed for their electrical and surface properties. The performance of the two types of nanoporous dielectric clad liquid core waveguides is presented.

Chapter 6 provides a future direction to this research along with conclusions.

## CHAPTER 2: NANOPOROUS DIELECTRICS

### 2.1 Introduction

It is well known that as the size of the matter approaches atomic scale, material properties such as electrical and nonlinear optical properties changes significantly from its bulk counterpart. With the recent advances in nanotechnology, new materials with tailored optical and dielectric properties are currently being engineered. These materials are called nanostructured materials as properties of bulk material are tailored and fine tuned by changes made at the atomic scale. Nanoporous dielectric materials are a class of nanostructured materials consisting of tiny air pockets or voids in the nanoscale. Nanoporous dielectric materials are gaining prominence in the recent years as they are finding applications in a wide range of fields including photonics [22], catalysis [23] and semiconductor processing [24]. Because of their extremely low refractive index, these materials have been considered as a better and a cheaper alternative to Teflon AF in liquid core waveguide applications [22]. With decreasing feature sizes, new materials with ultra low dielectric constant is a huge requirement in the semiconductor industry at present to replace conventional silicon dioxide as the interconnect insulation material<sup>24</sup>. Suitable materials with ultra low dielectric constant have to be obtained in order to minimize the RC interconnect delays. Depending on the processing conditions, it is

possible to obtain such materials with ordered or random pore distributions. As the pore size of these materials lies well below the wavelength of light, scattering of light by the presence of these pores does not occur.

Of all the known dielectric materials, air has the lowest dielectric constant, which translates to having the lowest refractive index. Thus by incorporating nanosized voids in a dielectric material, for ex silica, the effective dielectric constant of the composite material then become a function of porosity and the dielectric constant of the first material. This way the effective dielectric constant can be reduced and controlled by changing the porosity of the nanoporous material. There are different ways to prepare nanoporous dielectrics. The most widely used methods are the surfactant templating method for ordered porous structures and the porogen extraction method for random pore structures. Silica nanoparticles based thin films have also been explored for use as nanoporous dielectrics. In this chapter we propose a new method for the fabrication of organo silicate nanoporous dielectrics (NPO) coatings based on Methyl silsesquioxane (MSSQ) nanoparticles. Nanoporous silica and organosilicate films are the most widely and extensively studied materials and we will confine our discussion to these two kinds of materials. Methods of preparation of such materials are described in the subsequent sections.

## **2.2 Ordered nanoporous silica (ONPS)**

These materials are prepared via the so – called liquid crystal templating method [25]. A template can be defined as “A central structure about which a network forms such that the removal of the template results in a cavity with morphological and/or stereo chemical features related to those of the template”<sup>25</sup>. In the formation of ordered

nanoporous materials, supramolecular surfactant templates are employed. Surfactants are bi functional molecules containing a solvent loving (lyophilic head) and a solvent hating (lyophobic) head (See Figure 2-1). Because of this property, they can associate into supramolecular arrays in a solvent. Depending on the concentration of the surfactant, there are different phases associated with the surfactant molecules in the solution. Figure 2-1 illustrates the different phases associated with the surfactant molecules in a solution.

*Low concentrations*

At low concentrations, the solution behaves as an electrolyte and the surfactant molecules exist as free molecules

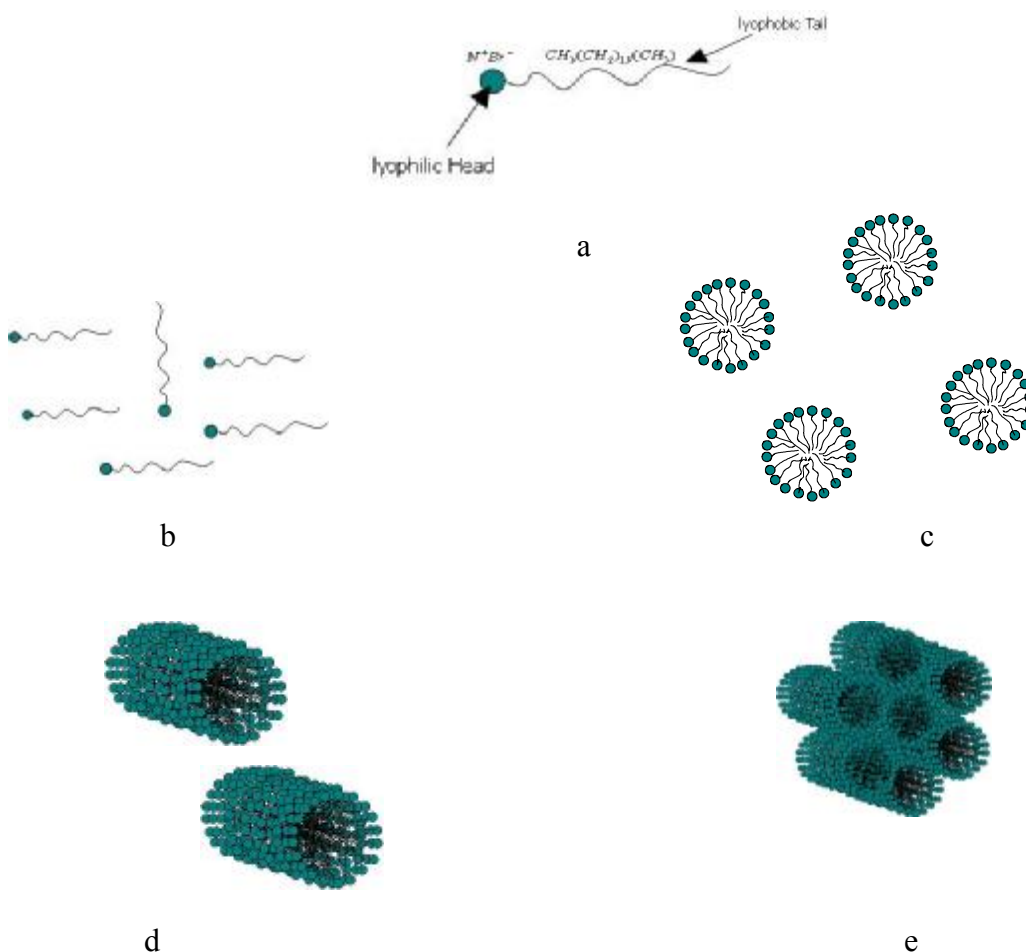


**Figure 2-1** Surfactant molecules in solution at different concentrations a. single surfactant molecule, b. surfactant molecules at low concentrations, c. surfactant molecules at the critical micellar concentration d. the cylindrical phase e. the hexagonal phase.

*Higher concentrations (Critical Micelle concentration, CMC1)*

At slightly higher concentrations (CMC1), the surfactant molecules arrange into a spherical micelle such that the lyophilic head group forms the outer surface and the lyophobic tail points towards the center. This arrangement minimizes the surface area of the tails exposed to the solvent.

*Higher concentrations (Critical Micelle concentration, CMC2 > CMC1)*

At higher concentrations than the CMC1 (CMC2), the spherical micelles coalesce to form elongated cylindrical rods.

*Higher Concentrations (Slightly higher than CMC2)*

At slightly higher concentrations, the elongated rod like micelles aggregate to form hexagonal close packed liquid crystal arrays. This phase is also called the liquid crystalline phase and this is the phase which acts like a template for the synthesis of the nanoporous structures. Ordered nanoporous silica based structures can be synthesized from these templates by dissolving silica sources around the surfactant arrays. The resulting silica/surfactant mesophases is condensed so that silica polymerizes around the surfactant array and the surfactant can then be burned off at high temperatures in a later process called calcination.

Thus the pore size can be tailored by tailoring the carbon chain length of the surfactant molecule or by dissolving auxiliary organics in the hydrophobic core of the surfactant hexagonal phase formation [26]. In certain cases, tri block copolymers were used in place of the surfactant molecules to yield highly ordered nanoporous dielectric. Pore sizes ranging from 2nm to 20nm have been reported based on the different preparation route employed.

### 2.2.1 Sol – Gel chemistry

The basic fabrication technology of these nanostructures follows the so called ‘sol-gel’ chemistry. Sol-gel as the name implies is a colloidal suspension of the inorganic matrix species (sol), usually nanoparticles in the size range 1-100nm, which is eventually gelled to form a network in a continuous liquid phase (gel)[27]. This technique has risen in popularity because of the ease of production and controllability of various aspects of the properties of glasses like hardness, optical transparency, chemical durability, porosity, and thermal resistance. Unlike the conventional way of preparation of inorganic glasses, which consists of melting at high temperatures, Sol-gel based glasses could be prepared at room temperatures.

Metal Alkoxides are the most common precursors for the preparation of the sol-gel based matrix as they react readily with water. Typically metal alkoxides of silica, for ex Tetraethyl Orthosilicate (TEOS) or Tetramethyl Orthosilicate (TMOS) are used for the preparation of silica based glasses [27]. The process typically consists of three reactions: hydrolysis of the alkoxides, alcohol condensation and water condensation Figure 2-2 gives the chemical reactions happening in a sol-gel process. In order to control the rate of condensation and hydrolysis, a suitable catalyst is added into the mixture. Conditions such as pH of the solution, Si/H<sub>2</sub>O molar ratio offer flexibility in the control of the reaction. As we can see from the reactions, the by product of the reactions is water. Since metal alkoxides are not miscible in water, a suitable solvent has to be used (ex. Ethanol). As the hydrolysis and condensation reactions proceed, the individual molecules are bridged gradually forming a network with entrapped alcohol and water. Upon gradual

drying, the volatile components are driven off from the matrix, shrinking the matrix in the process as further condensation can occur.

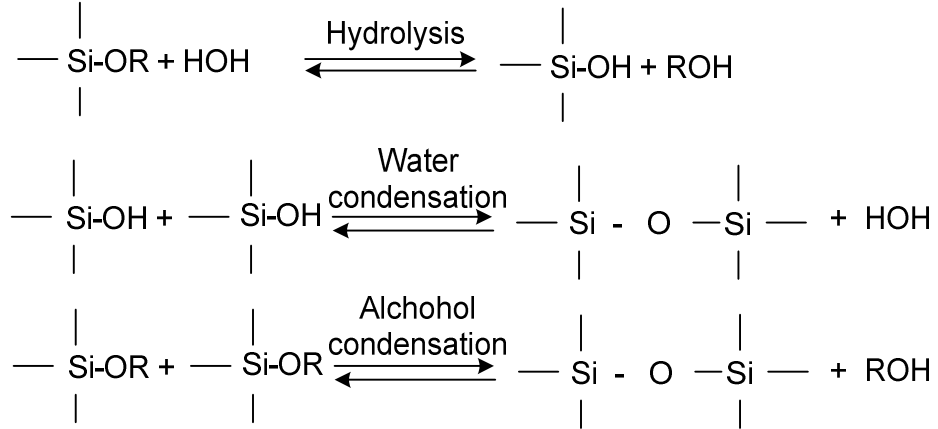


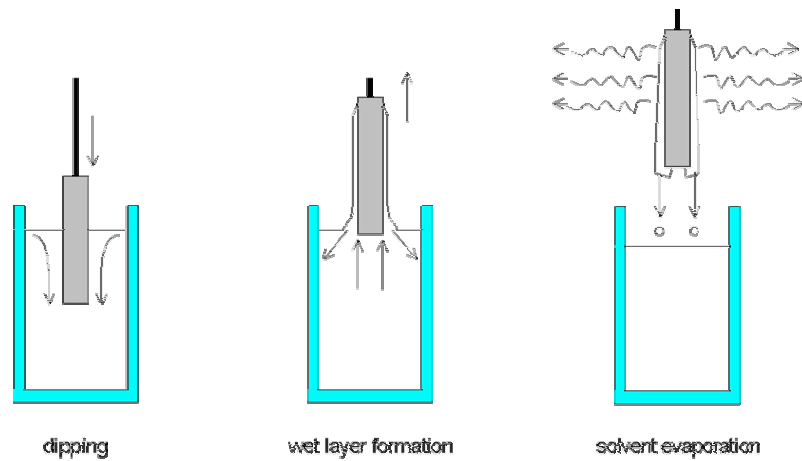
**Figure 2-2. The different reactions occurring in a Sol-gel process**

The sol-gel reactions can be either base catalyzed or acid catalyzed. Base catalyzed reactions are normally used to produce spherical particles. It has been reported that base catalyzed sol-gel reactions produce solutions which are not spinnable (to process thin films) compared to acid catalyzed reactions.[28,29]. For this reason we shall limit our discussion to acid catalyzed sol-gel reactions for the processing of thin films.

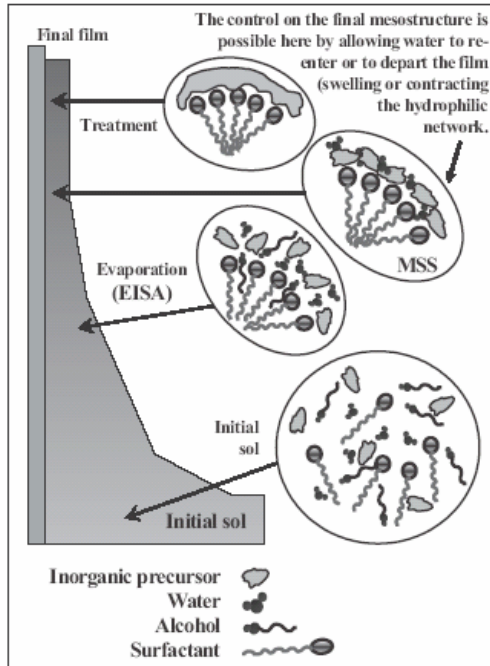
### 2.2.2 Sol-gel chemistry for Ordered Nanoporous Silica structures

As we have already seen in the above section, ONPS structures rely on the supramolecular assembly of surfactant molecules in solutions to obtain their structures. The difference between the regular sol-gel materials and these class of materials is the use of thermally labile, pre organized structures as structure directing agents over which the network cross linking occurs. The chemistry behind the formation of the matrix network is based on the sol-gel chemistry.

For the preparation of these organized structures, the precursor solution is prepared first which is either spin deposited or dip coated to produce the films. In addition to the chemical reagents for a typical sol-gel reaction, surfactant molecules are dissolved such that the initial surfactant concentration  $C_0 < C_{cmc}$ . Surfactant enrichment takes place only during the final stages of the coating process with the expulsion of the volatile components of the reaction mixture. As we have already seen above, when the surfactant concentration exceeds the CMC, it results in formation of the organized phases. Films coated employing the dip coating method has been reported to have an ordered structure for the pores. The dip coating process [30] and the self organization occurring among the inorganic and the surfactant species during a dip coating process is illustrated in Figure 2-3.



a



b

**Figure 2-3. a. Illustration of the Dip coating process.**  
[www.solgel.com/articles/Nov00/mennig.htm](http://www.solgel.com/articles/Nov00/mennig.htm),  
**b. Evaporation induced self assembly process for ONPS films [31]**

The precursor solution is taken in a beaker. The substrate is dipped in the precursor solution and gradually withdrawn at a constant withdrawal speed. During the coating process, the entrained solution experiences a preferential evaporation of the most volatile components, ethanol in this case, thereby increasing the concentration of water, HCl and the non volatile components – silica and the surfactant. The coating thickness depends on the withdrawal speed as well as the viscosity of the precursor solution. The higher the withdrawal rate, the thicker the film.

### 2.3 Nanoporous dielectrics by sacrificial porogen approach

The motivation for the preparation of nanoporous dielectric films arose in the microelectronics industries in their quest for low dielectric constant ( $k$ ) materials for semiconductor processing. One of the major considerations for these dielectric materials

is that the pore size has to be less than the feature size of the integrated circuit (<100nm) to avoid the “killer pores” [32]. Ideally these materials should be hydrophobic in nature so as to minimize the moisture intake which increases the dielectric constant and the refractive index of the film.

Of particular interest are the Methyl silsesquioxane (MSSQ) based nanoporous matrix materials as the methyl substituent provides for a low density and dielectric constant compared to pure SiO<sub>2</sub> matrix. The lower polarizability of the Si-CH<sub>3</sub> bonds in comparison to the Si-O bonds is another factor which has been attributed for the low dielectric constant [24]. Furthermore these materials possess high thermal and dimensional stability and are hydrophobic due to the predominance of the CH<sub>3</sub>- groups in the molecule[33] (See Figure 2-4).The hydrophobic nature of these films is important when these films are used as cladding material for the liquid core waveguide so as to keep the water from seeping into the pores of the material.

In this approach, nanopores are introduced in the solid dielectric matrix first by preparing a nanocomposite consisting of the matrix material and a pore generating agent (also called porogen) followed by the selective removal of the porogen from the composite. The porogen molecule is a thermally degradable material which can be easily burned off at elevated temperatures. The porogen and the matrix precursor material should satisfy the following conditions in order to be able to be used to successfully fabricate a nanoporous low-k dielectric material.

1. The degradation temperature of the porogen molecule should be lower than that of the matrix material.

2. The matrix material should be dimensionally stable during the porogen degradation process at high temperatures to avoid the collapse of the generated nanopores.
3. The porogen and the matrix precursor materials should dissolve homogeneously in a common solvent without any phase separations.
4. The miscibility of the matrix material and the porogen has to be maintained until the thermal degradation of the porogen is complete in the production of the final nanoporous dielectric film.

Different molecules have been considered for the porogen material and can be classified into dendrimers, star shaped polymers, hyper branched polymers and cross linked polymer nanoparticles [33]. Figure 2-4 illustrates the preparation scheme for the nanoporous dielectrics. The appropriate matrix precursor and the porogen are first mixed in a pre determined ratio in a common solvent and spin coated onto the substrate. The obtained film is baked following the spin coating to instigate the matrix cross linking. After the cross linking step, the film is heated at elevated temperatures to burn off the porogen leading to the nanoporous dielectric film.

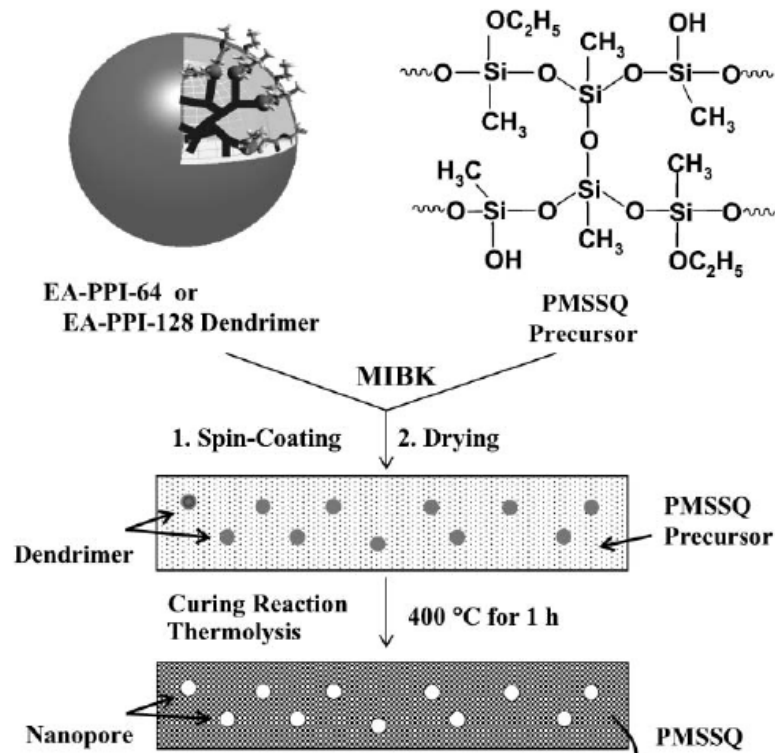


**Figure 2-4 Procedure for the preparation of a Nanoporous dielectric film using Polymethyl Silsesquioxane as the matrix material and EA-PPI-64 as the porogen [33]**

The morphology of the obtained film depends on its pore volume fraction or percentage porosity which in turn depends on the amount of porogen loading during the precursor preparation [33]. The greater the porogen loading, the higher the porosity (provided the pores haven't collapsed). There are two types of film morphologies 1. The open pore structure 2. Closed pore structure. The so called open pore structure refers to the films obtained with a higher amounts of porogen loading. These structures have interconnected pores through out the film cross section. Because of this structure, the mechanical strength of these films are significantly lower. The closed pore structures on the other hand are produced at relatively lower porogen loadings. The obtained pores are separated from each other and independent. Figure 2-5 shows the open pore and the closed pore morphologies for the nanoporous dielectric films.

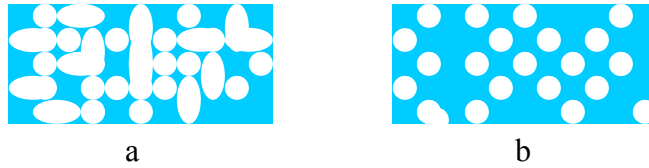


**Figure 2-5 a. the closed pore and b. the open pore structures for the nanoporous dielectric films by porogen approach.**

## **2.4 Silica Nanoparticles based thin films as nanoporous dielectrics**

There hasn't been much literature on the preparation of nanoporous dielectric films by the deposition of dielectric nanoparticles. The nanovoids are formed because of the nature of packing of the nanoparticles in the thin film. Si et. al reports nanoporous silica films formed by the gas evaporation of  $\text{SiO}_2$  nanoparticles in an Argon atmosphere [34]. Nozaki et. al reports nanoporous silica films formed by the oxidation of Silicon nanoparticles [35]. In his method of formation, silicon nanoparticles are first deposited by the evaporation of Silicon in an argon atmosphere. Low temperature dry oxidation of these nanoparticulate film is performed to form the nanoporous silica. In both the published literatures, the nanovoids formed are reported to be closed voids. Dielectric constant as low as 1.3 has been reported.

Another way of forming nanoparticulate thin films is by the deposition of well dispersed colloidal nanoparticles in the presence of a binder material. A small amount of plastisizer is added to facilitate the formation of crack free films. The precursor solution is spun coated followed by high temperature treatment step for binder burn out.

### **2.4.1 Rapid formation of Ultra low – refractive index nanoporous dielectric films based on PMSSQ nanoparticles**

We report a novel technique for the formation of ultra low refractive index PMSSQ nanoparticles based thin films. The nanoparticles of PMSSQ are formed in the

solution phase and films are spun coated from this precursor solution followed by a high temperature calcination step. It is well known that when macromolecules (polymer molecules) are dissolved in different solvents, they tend to get coiled to different degrees depending on the interaction between the repulsive and attractive forces in the solution as well as the temperature. In a good solvent, the chains are extended and in a poor solvent on the other hand, the chain molecules assume a highly coiled form [36]. A detailed mathematical analysis can be found in the paper published by Raos et. al [37]. Furthermore, as the solution temperature is gradually cooled, the molecules become progressively more coiled until they are no longer soluble and precipitation occurs. The temperature at which this occurs is called the “theta” temperature or Forley temperature. A good solvent can thus be defined as the solvent having a theta extremely lower than normal (room) temperature and a poor solvent as one having a theta close to normal temperature. There is a steric repulsion between the polymer segments in a good solvent and an attraction in a poor solvent [38].

This aspect has been well exploited by Yabu et. al [39] who reports on the formation of polymer nanoparticles from a clear solution containing nonvolatile poor solvent by slow evaporation of a volatile good solvent. In his method, a poor solvent is added to a polymer solution in a good solvent and the good solvent is slowly removed by evaporation. The choice of the solvents to be used in this method requires that the boiling point of the poor solvent is considerably higher than that of the good solvent and that they are miscible with each other [39]. They report on the preparation of polystyrene nanoparticles using this method using THF as the good solvent and water as the poor solvent for dissolving polystyrene.

According to their hypothesis, when the polymer molecules are dissolved in the good solvent, their chains are extended and are in a random coiled structure. However, with the addition of the poor solvent, and as the evaporation of the good solvent proceeds, the relative amount of poor solvent is increased. The repulsive forces acting on the polymer molecules due to the interactions by the surrounding poor solvent molecules force them into compact folding and the polymer molecules grow to small nuclei [37]. The dynamic equilibrium shifts towards the formation of small nuclei as the evaporation of the good solvent proceeds.

This phenomenon has been applied for the synthesis of PMSSQ nanoparticle dispersion. Propylene glycol monomethyl ether acetate (PM Acetate) was chosen as the good solvent. It is well documented that PPG, a linear molecule forms phase separations when mixed with a PMSSQ solution [40]. Thus PPG (Mn 425) was chosen as the poor solvent. PM Acetate is a good solvent for both PMSSQ and PPG. Furthermore, PPG has a higher boiling point than PM Acetate. A solution of PMSSQ is first formed in PM Acetate to which a separate solution of PPG in PM Acetate is added. The final solution is subjected to evaporation at slightly higher temperature. In addition to the various physical phenomena described above, PMSSQ molecules also cross link during the evaporation step. After appropriate amount of the good solvent is evaporated, PMSSQ nanoparticles are formed and well dispersed in the solution containing PPG. Figure 2-6 illustrates the hypothetical formation mechanism.

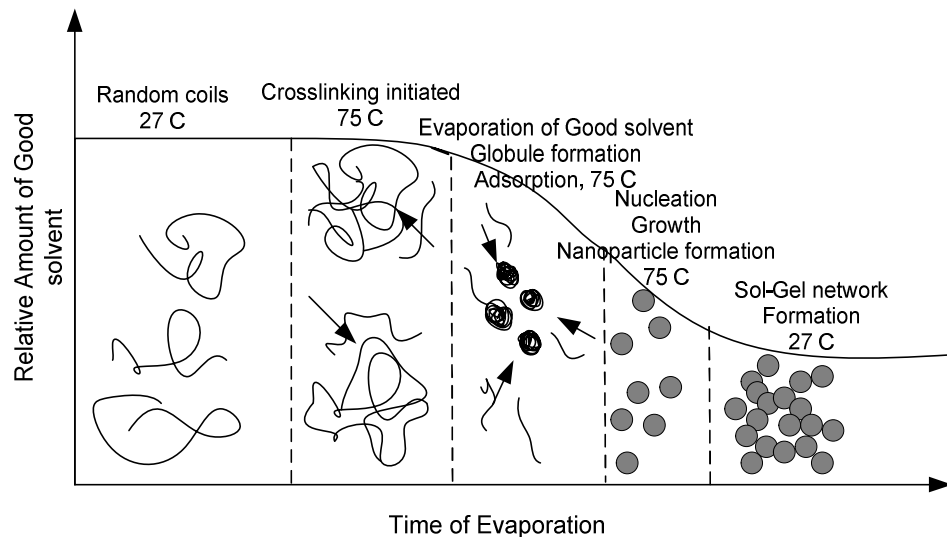


**Figure 2-6 Illustration of the PMSSQ nanoparticle dispersion formation mechanism**

This dispersion is then spin cast on to the substrates to form a thin film. The obtained thin film is calcinated to burn off the PPG molecules resulting in the nanoporous film. In addition to serving as the poor solvent, the PPG molecules act as a steric hindrance in keeping the nanoparticles from agglomerating. These molecules act as spacers during the final nanoporous film formation thus increasing the porosity in the final film. The cross linking rate is also increased significantly for the PMSSQ molecules and they continue to cross linking even after stopping the good solvent evaporation and ultimately form a clear gel. Further characterization of the gel is under process.

We believe that this technique of formation of nanoporous films should be applicable to the formation of other nanoparticulate films for instance Teflon AF with the right choice of the solvents and mixing ratios.

## 2.5 Experimental

We have worked on the preparation of the nonporous dielectric films employing the methods outlined above. The experimental details of the preparation method are given below.

### 2.5.1 Preparation of the Ordered Nanoporous silica films

We have followed the method outline by Lu et. al [41] for the processing of the ONPS films. All the chemical for the experiment were purchased from Sigma – Aldrich. TEOS ((Si(OC<sub>2</sub>H<sub>5</sub>)<sub>4</sub>)) is the silica source, Hydrochloric acid was used as the catalyst. Ethanol was used as the solvent for the reaction. Cetyl Trimethyl Ammonium Bromide (CTAB) was the structure directing agent. The preparation of the precursor solution followed a two step process to minimize the siloxane condensation rate. First, TEOS, Ethanol, DI water and HCl were mixed in the molar ratio 1:3:8:5\*10<sup>-5</sup>. This mixture was refluxed at 60° C for 90 minutes. After the first step, water and HCl was added to the mixture increasing the concentration of HCl to 7.34mM. the mixture was stirred at room temperature for 15 minutes, followed by aging at 50° C. CTAB and ethanol was then added to this mixture to obtain a final ratio of 1TEOS : 22 C<sub>2</sub>H<sub>5</sub>OH : 5H<sub>2</sub>O : 0.004 HCl : 0.046 CTAB.

Silicon substrates were subjected to an organic clean procedure to remove any organic contamination from the surface [42]. Films were prepared on these cleaned substrates through the dip coating process. After the initial coating of the film was complete, the coated substrates were kept at 130 C for 3 minutes inside an oven for solvent removal as well as facilitate further cross linkings in the film. These substrates

were later calcinated at 400 °C for one hour at a ramp rate of 1 °C/min inside a furnace. Ellipsometric characterization of these films was performed.

### **2.5.2 Nanoporous dielectric films through sacrificial porogen approach**

For the preparation of these films, PMSSQ (Gelest) has been used as the matrix material. PPG (Mn : 425, Dow) has been used as the porogen. Typically, 30% by wt of PPG in Polyglycol Methyl Ether Acetate was taken and ensured complete dissolution by sonicating for ~10 mins (Solution A). 30% by weight of PMSSQ was dissolved in Polyglycol Methyl Ether Acetate by sonication (Solution B). Solution A and B were mixed together in 50:50 ratio and sonicated for 10 mins.

Films were spun cast from these solutions onto organic cleaned [42] Silicon substrates at baking was performed 3000 rpm for 30s followed by a high temperature baking step in a gravity convection oven for 45 mins. baking temperatures of 200 °C and 300 °C were investigated

### **2.5.3 PMSSQ nanoparticles based Nanoporous dielectrics**

For the preparation of these films, PMSSQ (Mn 6000 – 9000, Gelest, Inc or Mn 5000, Technoglas ), PPG (Mn 425, Aldrich) and PM Acetate (Sigma-aldrich) are used as supplied. A 50 % by weight solution of PMSSQ is prepared by dissolving 5g of PMSSQ in 5 g of PM Acetate and designated as solution A. A 50 % by weight solution of PPG is prepared in PM Acetate by dissolving 5 g of PPG in 5 g of PM Acetate and designated as solution B. Solutions A and B are then sonicated separately for atleast 10 – 15 mins to ensure complete dissolution of the respective solutes. After obtaining clear solutions, Solution A is mixed with solution B and sonicated for an additional 5 mins to obtain a

homogenous solution. This solution is then taken in an open beaker and placed on a hot plate at 70 °C under constant stirring. The weight of the solution is continuously monitored and the solution is removed from the hot plate after the appropriate amount of the good solution is evaporated. Typically evaporations of 0.5g, 1g, 2g and 6g has been performed and experimented with. The resulting clear, viscous solution is then transferred into a glass bottle and sealed for further use. The solutions thus prepared are dynamic in nature and the solution gets more and more viscous with time. For thicker NPO coatings, longer aging times are recommended.

Films were spun cast from these solutions onto organic cleaned [42] Silicon substrates at 3000 rpm for 30s followed by a high temperature baking step in a furnace/contact hot plate at 470 C. The high temperature baking time of 10 min for the contact hot plate and 15 – 20 mins for the furnace were typically used. Baking times also varied with the thickness of the films. For thicker films and films spun coated on glass substrates, baking was performed in the furnace.

## **CHAPTER 3: DEVICE DESIGN AND FABRICATION**

### **PHYSICAL CHANNEL DESIGN**

#### **3.1 Device design**

The liquid core waveguide system has been designed to enable a rapid multiplexing capability by following the well established microfabrication techniques. The device essentially consists of straight microchannels etched in silicon to hold the liquid medium (Aqueous based). The channels are coated with a low refractive index nanoporous dielectric layer (~ 1 – 2 microns thick) to act as the cladding material. Appropriate surface treatment techniques are performed on the coated films to render them hydrophobic and/or seal the top few nanometers of the film to prevent the liquid from seeping inside the nanopores. A nanoporous dielectric coated glass substrate with the appropriate surface treatment performed, is used to seal the channels. Figure 3-1 shows the schematic of the proposed liquid core waveguide system.

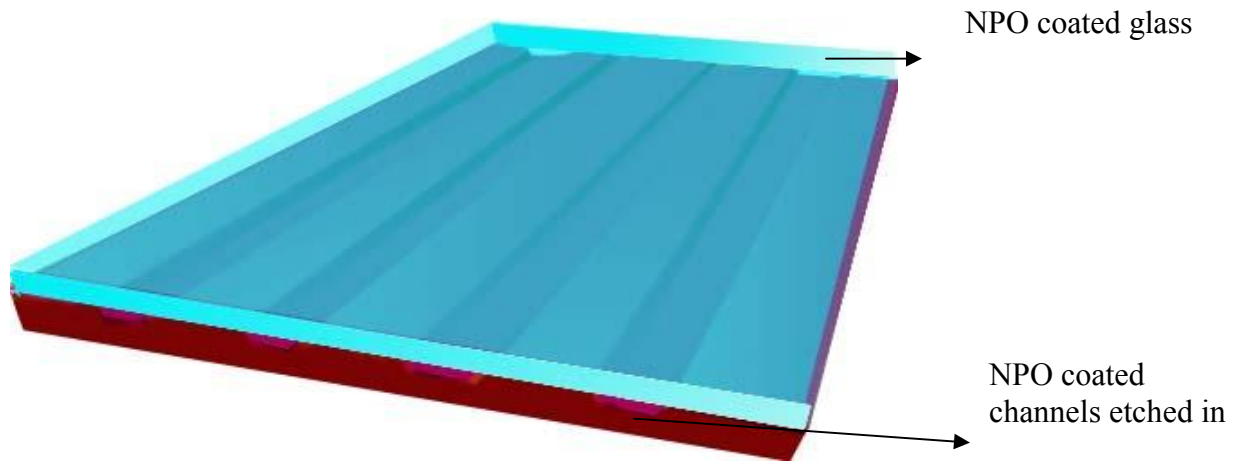


**Figure 3-1. Conceptual design of the microfabricated liquid core waveguide system**

## **3.2 Device fabrication**

The entire steps for the fabrication of the liquid core waveguide can be grouped in to three sections : 1. Fabrication of channels in silicon 2. Preparation of smooth, crackfree nanoporous dielectric films followed by surface treatment 3. Bonding of nanoporous dielectric coated silicon channels and glass.

### **3.2.1 Fabrication of channels in Silicon**

The etching of channels in silicon was performed following the techniques that have been developed for conventional MEMS based devices. Anisotropic wet chemical etching techniques using potassium hydroxide as the etchant has been followed.

Figure 3-2 illustrates the process flow for the fabrication of channels in Silicon. Silicon Carbide thin film has been used as the hard mask during the etching process. The detailed processing steps are given below:

*Step 1: Cleaning of the Silicon wafer*

(1 0 0) 8” Silicon wafers (700 micron thick, P-type, boron doped, resistivity 3-4 Ohm - cm) are first thoroughly cleaned with acetone, methanol, isopropyl alcohol to remove any organic contamination from the surface. The cleaned wafers are air dried and prepared for further fabrication steps.

*Step 2: Plasma enhanced chemical vapor deposition of Silicon Carbide thin film*

The cleaned silicon wafer from step 1 is then coated with a 200 nm thick Silicon Carbide film to function as the hard mask during the KOH etching. Plasma enhanced chemical vapor deposition system (Precision 5000) has been used to deposit these films. Previous experiments have shown that Silicon Carbide is an excellent material to function as the etch mask as these films could withstand harsh KOH etching procedures without any noticeable degradation. A 50 nm thick Silicon Carbide film has also been experimented with there was no degradation of the film quality with etching.

*Step 3: Sputter deposition of Aluminum*

The Silicon Carbide coated silicon substrate is then sputter coated with a 130 nm Aluminum coating. The aluminum layer is used as the etch mask during patterning of the Silicon Carbide. Previous attempts at using photoresist as the etch mask wasn't effective as the photoresist tends to degrade in the presence of plasma and photoresist stripping would become a hassle. Aluminum proved to be a better alternative.

*Step 4: Preparing the substrates ready for patterning*

The processed substrate is later cleaved into 1.5” by 1.5” squares by scribing on the wafer with a diamond scribe and cleaving the wafer along the wafer planes.

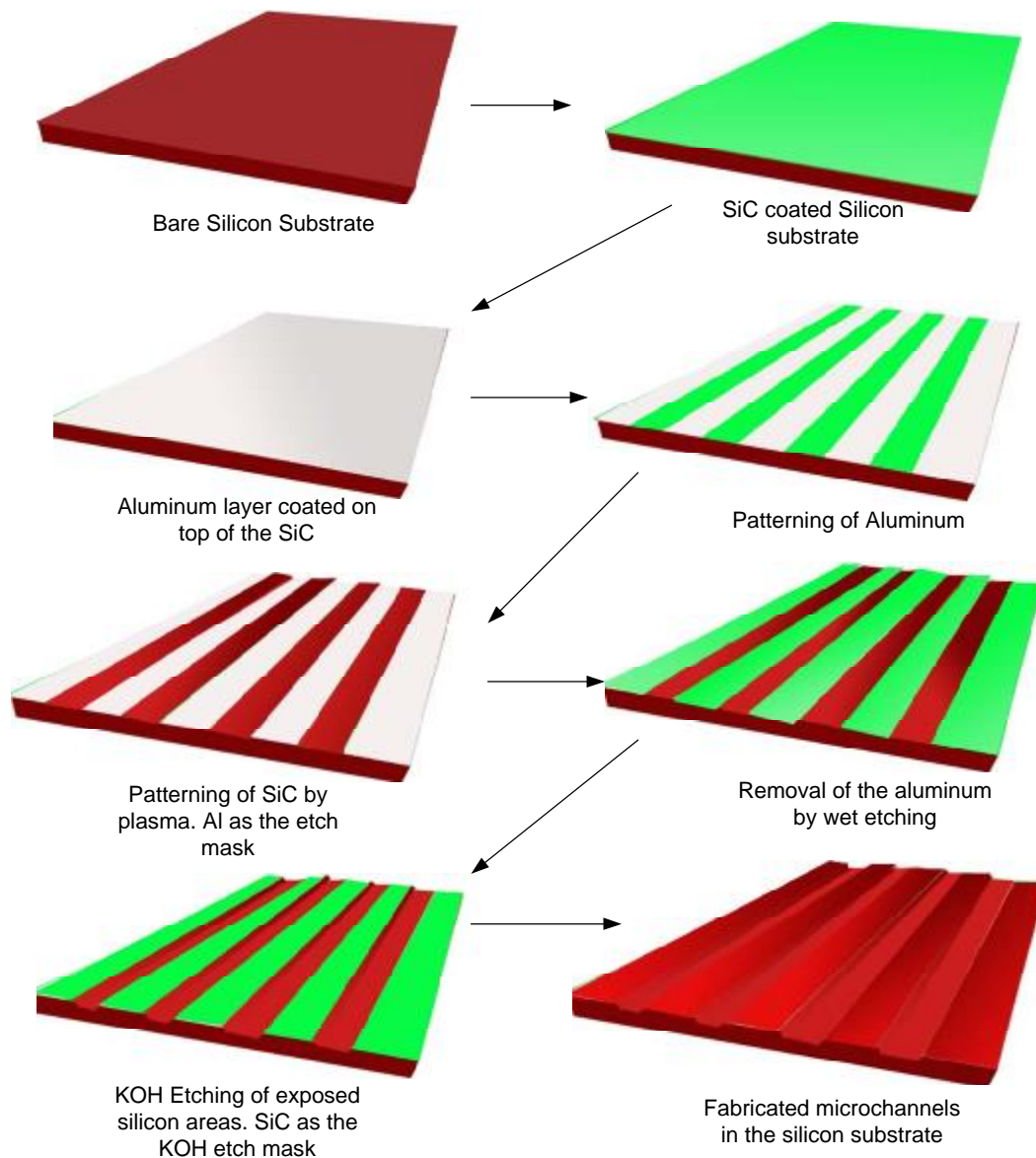


**Figure 3-2. Process flow diagram for the etching of microchannels in silicon**

*Step 4: Patterning channels, photolithography*

Patterning of the channels is done using AZ nLOF2020 (Clariant AZ Electronic Materials) which is a negative photoresist. The photoresist is first spun coated at 3000 rpm for 30 s followed by a pre bake at 110 C for 60s. OAI Mask aligner is used for UV exposure. The channel mask is a hard mask containing parallel patterns of the channels. Two widths (400 microns wide and 220 microns wire) have been considered in this particular design. Figure 3-3 shows the mask layout for the channels. We have used adobe illustrator 9.0 for the mask design.

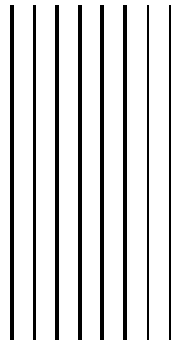


**Figure 3-3. Typical channel mask. the mask is designed to have two different channel widths. Channel widths of 400 microns and 200 microns were considered in this study.**

Since we were using a negative photoresist, the channel portions were darkened out and the non channel positions were transparent in the mask. The exposure time was calculated first by measuring the power output of the UV lamp. Dividing the required DTP for the photoresist (66mJ/Sq.cm) by the measured power intensity of the lamp gives the exposure time in seconds. The wafers were post exposure baked at 110 C for 60s. Developing of the wafers was done with AZ 300 MIF developer for 90 s. After this step,

the photoresist remains on the exposed areas. The masked areas are dissolved in the developer and the aluminum surface is exposed.

*Step 5: Wet etching of exposed aluminum areas*

A mixture of concentrated phosphoric acid (Sigma-aldrich), Nitric Acid (Sigma-aldrich), Acetic Acid and DI water in the ratio 85:5:5:5 by volume is used as the Aluminum etchant. The mixture is taken in a glass beaker and heated to ~ 70 C. The patterned substrates from step 4 are then dipped in this mixture. After the exposed aluminum is etched (when the silicon Carbide surface becomes visible in the exposed areas), the substrates are withdrawn from the etchant solution and immediately placed in D.I water. The substrates are later rinsed thoroughly in DI water and air dried.

*Step 6: Photoresist stripping*

The substrates from step 5 are then immersed in AZ Kwik Strip, to strip away the photoresist. AZ Kwik strip solution is heated to 60 C and the substrates immersed in it. Within 3-4 minutes, the excess photoresist gets stripped away from the substrate. The wafers are then rinsed thoroughly with DI water and air dried.

*Step 7: Plasma etching of Silicon Carbide*

The substrates from step 6 are later kept for plasma etching of the exposed Silicon Carbide. Plasma etching is performed in using the P-5000 in a different chamber set aside for etching.

*Step 8: Etching of Aluminum films*

The substrates from step 7 are later kept in the aluminum etchant to etch away the Aluminum following the procedure outlined in step 5.

*Step 9: Etching channels in Silicon*

Smooth channels are an absolute prerequisite for a good waveguide design. Roughness introduced in the channels during the etching step will increase the scattered light thus resulting in increased losses. Although nanoporous silica dielectric film also acts as a filler material, roughness of the channels has to be kept down. Etching channels in Silicon is accomplished by KOH which results in anisotropic channels. The channel profile obtained by anisotropic wet chemical etching using KOH is shown in Figure 3-4.



**Figure 3-4. Anisotropic etch profile of the channels obtained by KOH wet chemical etching.**

88 grams of KOH (88% KOH, Sigma-Aldrich) is mixed with 15 ml of DI water. The mixture is kept on a hot plate at 220 C and constantly stirred with a glass rod. As the stirring continues, there will be excess KOH sticking to the walls of the beaker. Controlled amount of DI water (~ 10ml) is squirted onto the sides of the beaker to let the KOH fall back into the solution. Once a homogenous solution is obtained, small amount of Antimony tri oxide (0.0015-0.0020 g) is added to the solution while the solution is being stirred. The hot plate temperature is reduced to 150 °C and the solution temperature is monitored. Once the solution temperature reaches 150 °C, the SiC patterned silicon substrates from step 8 are dipped and the beaker covered. We have observed that the measured etch rate is 1.1 – 1.3 microns/min. Thus etching is performed until a desired channel depth is obtained. Channel depth is measured using a profilometer.

*Step 10: Plasma etching of Silicon Carbide*

After the channel etching step, the substrate is then subjected to a SiC plasma etch to remove the SiC film. This is the final step in the process of fabricating channels in silicon. The Silicon channels are ready for further processing.

### **3.2.2 Nanoporous Dielectric cladding**

Three types of the nanoporous dielectric films have been investigated for use as the cladding material for the Liquid core waveguide - Ordered nanoporous silica films, Nanoporous PMSSQ films prepared by porogen extraction and PMSSQ nanoparticulate based nanoporous films. The theory and the experimental details for the preparation of these films is described in chapter 2.

Typically the channels are coated either through dip coating or spin coating process. The precursor viscosity is adjusted such that thick films with thickness greater than 1 micron are obtained. The silicon substrates with channels are first cleaved such that there are three channels in each piece. During the spin coating process, the silicon channels are aligned such that the middle channel is aligned with the axis of rotation of the spinning chuck. This is done to minimize the non uniformities in the channel coatings. Likewise, film coatings were performed on borosilicate glass substrates (pyrex 4470).

After the appropriate thermal treatment to incorporate pores, a photoresist film is coated on top of the surface. Typically S1813 (Shipley) positive photoresist is coated at 3000 rpm for 30 s. This photoresist film protects the nanoporous film present in the channels during the mechanical polishing step to remove the NPS film from the non channel portions.

### **3.2.3 Bonding of NPS coated channels and glass**

This is the final step in the fabrication of the whole liquid core waveguide system. The bonding is performed following the anodic bonding techniques. A brief description of the technique is given below.

#### ***3.2.3.1 Anodic Bonding***

Wafer level bonding techniques have been developed extensively over the past decade for various applications. They are currently being applied commercially in integrated circuits (IC) industry for packing pressure sensors, accelerometers as well as various other MEMS based devices [43]. They can be broadly classified into three types, 1. Direct bonding, 2. Intermediate layer bonding, 3. Anodic bonding. Direct bonding involves placing two substrates in intimate contact and subjecting the substrates to a high temperature annealing step using in the orders of thousands of degrees. Direct bonding places stringent requirements on the cleanliness and flatness of the substrates to be bonded. Intermediate layer bonding requires the deposition of an additional layer which acts as the adhesion layer between the substrates to be bonded. This requires lower temperatures than the direct bonding techniques. Anodic bonding technique on the other hand is similar to the direct bonding technique with out the stringent requirements of an atomically flat and clean substrates. Anodic bonding is performed at moderate temperatures (on the order of hundreds of degrees) under an external applied potential between the substrates to be bonded. This bonding technique was originally developed for bonding. Extremely high bond strengths can be obtained by this bonding technique.

Anodic bonding was discovered by Pomerantz in 1968 [44]. In this method, the substrates (glass – silicon or glass - metal) are kept in contact at high temperature

(usually 350 – 450 C) and a high electric potential is applied across them (usually 1000 V). Figure 3-5 shows the schematic of the Anodic bonding process.

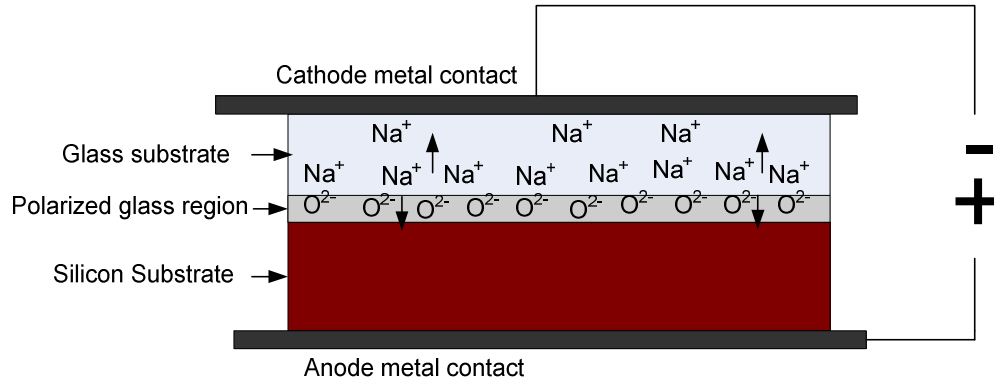


**Figure 3-5. Schematic of the Anodic bonding process**

When the substrates are subjected to a high temperature, the mobility of the sodium ions is increased. Upon the application of the high electric field between the substrates, migration of sodium ions takes place and the ions move towards the cathode creating a polarized region at the glass- silicon interface (see Figure 3-5). The oxygen ions present at the interface migrate towards the anode (silicon) and gets bonded to the silicon atoms forming a very strong bond at the interface.

This bonding technique has also been applied for bonding silicon wafers together with an intermediate glass layer [45] and glass substrates together with intermediate mediate metal layers. This method of bonding was chosen in this project because of the advantages it offered. Apart from the relatively low temperature requirement, this bonding technique is simple and does not require any additional intermediate layer which could be a source for waveguide losses. We have attempted to bond the NPS coated channels with NPS coated glass following the anodic bonding but it resulted either in no

bonding or very weak bonding between the substrates. The presence of the NPS surface at the interface creates a barrier for the oxygen ions from migrating towards the silicon and forming a bond. NPS coated glass substrates were attempted to be bonded with plain silicon wafers. In this case, we have tried bonding with two different types of the nanoporous dielectric coatings – the Ordered nanoporous silica and the PMSSQ nanoparticles based nanoporous dielectrics.

The substrates were washed following the organic clean procedure and the dielectrics were spun coated and processed to obtain the nanoporous films. The thickness of the obtained ONPS films was ~ 600nm. The anodic bonding arrangement of Figure 3-5 has been used for performing the bonding. Temperature of the substrates were ramped up to 350 C. once the temperature reached 350 C, the high voltage power supply was turned on and the voltage level was gradually increased to 1100 V. The bonding was performed for a total of 35 mins after which the power supply and the hot plate were turned off. The substrates were examined for quality of the bonds.

In the case of the ONPS coated glass wafer, it resulted in a good bond with a > 85 % bonded surface. The un bonded areas could be attributed to the presence of dust particles on the surface. The resulting bonds were extremely strong and the bonded substrates couldnot manually be separated. Figure 3-6 shows the picture of the bonded surfaces.

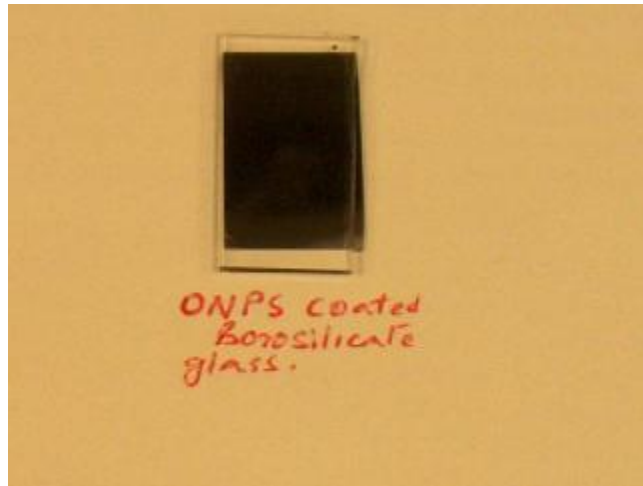


**Figure 3-6. Picture of the ONPS coated borosilicate glass bonded to a silicon substrate by the anodic bonding technique**

In the case of the bonding between the PMSSQ nanoparticulate film coated glass and silicon, the resulting bonding was weak and in most cases there wasn't any bonding at all. Varying the parameters like temperature and the voltage did not improve the bond quality. Because of the extremely low refractive index, (1.10 – 1.13), the available surface area for bonding is extremely less at the interface. Also the films were typically greater than a micron thick thus producing a, larger barrier for the oxygen ions from the glass substrate to migrate towards the interface. This may have been one of the reasons for the failed bonding. Thus patterning the NPS coated glass substrate and precise alignment with the Silicon channels is required for the LCW fabrication.

### **3.2.4 Fabrication of the whole device**

The fabrication steps for the whole device starting with the silicon microchannels is given in Figure 3-7.

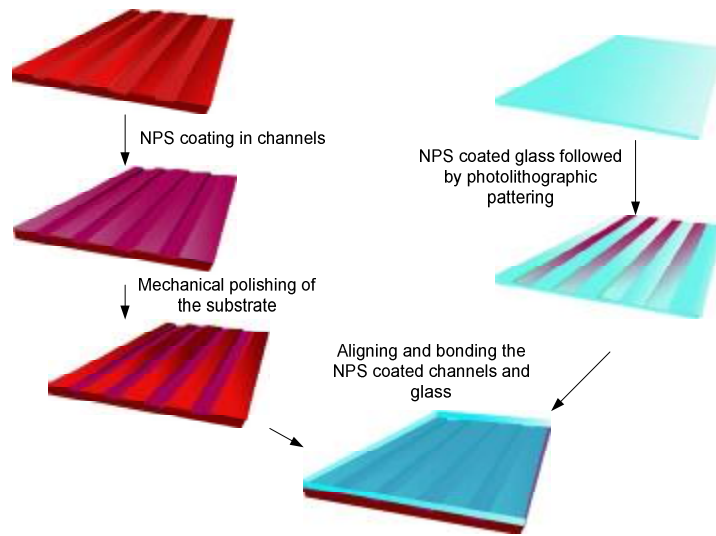


**Figure 3-7. Fabrication of the complete Liquid core waveguide system**

Nanoporous dielectric material from the non channel portions is removed by mechanical polishing. Polishing pads with particle size 0.3 -1 micron has been used to remove the nanoporous dielectric from the non channel parts. The glass substrate is coated and patterned via conventional lithographic techniques. For the patterning of the NPS on the glass substrate, plasma etching has been employed using CF<sub>4</sub> and CHF<sub>3</sub> plasma to etch the NPO film.

### **3.3 Drawbacks of the current design**

Although the design of the on-chip waveguide system is compatible with the traditional IC manufacturing technique, there are certain major drawbacks of the design.

1. Precise alignment of the patterned nanoporous dielectrics on glass with the etched channels in silicon is a requirement in the present design for a reliable bonding. It has been observed that in the case of slight misalignment in the order of a couple of microns, the NPO film comes in direct contact with the non channel parts of the silicon substrate. During the bonding, this misalignment induces stress in the films eventually leading to a cracked film on glass.

2. To get around this problem, 10 micron deep channels have been etched [46] in glass substrates and coated with NPO films similar to silicon channels. The substrates were later processed to remove the NPO coatings from the non channel regions by mechanical polishing. These substrates were later bonded with the silicon substrates with channel alignment. By having NPO coated channels on glass, slight misalignments in the channels wouldnot induce any stress in the films as the film is only confined to the channel portion on the glass substrates. However, this solution only increases the fabrication complexity as the channels had to be etched both in silicon as well as glass substrates.

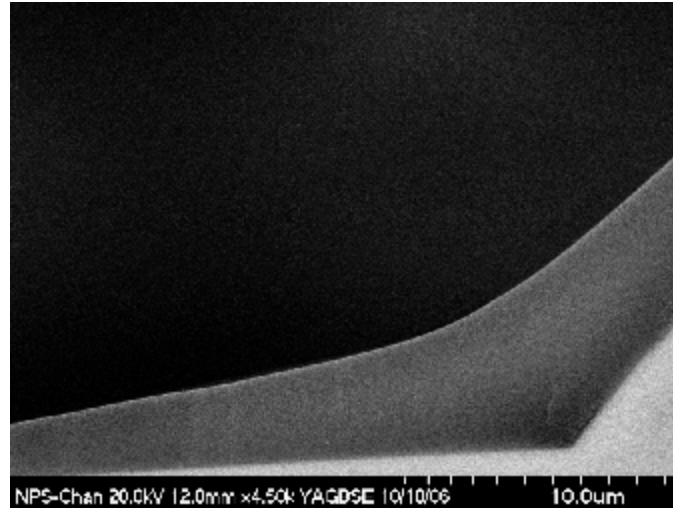
3. The method of coating the channels with NPO was through spin coating technique. We have observed that this method of coating yields highly non uniform films within the channels with the coatings on the edges being an order of magniture thicker than the coatings on the channel floor. Figure 3-8 shows the SEM of the NPO coatings in the channels through spin coating technique. The thickness on the channel floor was less than 500 nm even though the films prepared on flat substrates (without any channels) under similar conditions gave films with thickness greater than one micron. Two reasons could be attributed to this behaviour –1. the capillary effect arising due to the presence of the channel structures 2. Thermocapillary effect due to nature of the precursor solution and heat treatment steps.

*Capillary effect:* During the film deposition by spin coating, because of the channel confinement, saturated vapor of the solvent exists which prevents fast evaporation of the solvent within the channel, thus throwing out more solution out of the channels. This

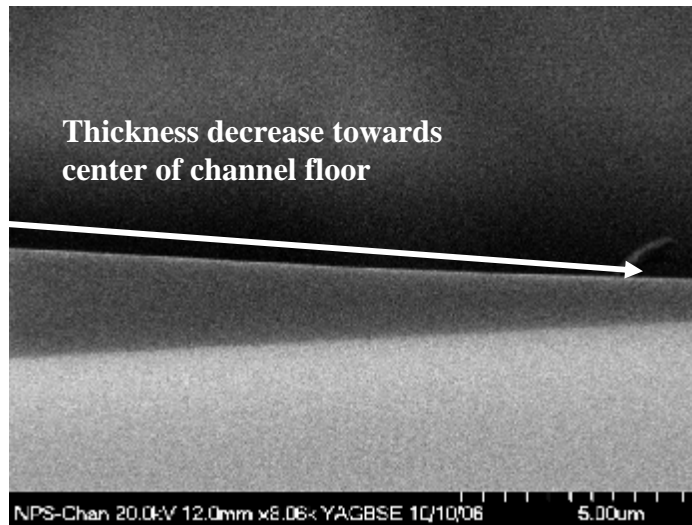
results in thinner films within the channels compared to films prepared on flat substrates where the solvent experiences faster evaporation.

*Thermocapillary effect:* Surface tension of a fluid is a function of temperature, higher the temperature, lower is the surface tension. Thus if we consider a fluid on a surface with different temperature profiles, a net force develops which results in fluid motion in a certain direction (towards cooler regions). A thermocapillary flow is induced in the bulk fluid due to the non-uniform heating of the free surface. This effect is more prominent in fluid confined to very small dimensions ( $< 1$  mm).

For the final film formation, the coated channels are kept for annealing at 470 C for 5mins. In the case of a flat substrate, the substrate is uniformly heated and hence there are minimum localised temperature variations. However, in the case of channels, at the instant the substrate is kept on the hotplate, the channel floor is at a higher temperature compared to the top surface (before equilibrium has been reached). This results in the thermocapillary effect. Also, even though the solvent evaporates during the spin coating itself, what is left behind is a nanoparticle dispersion in PPG. Thus the film can still be considered "fluidic" in nature. Thus during the final film formation, more of the fluid is pushed towards the channel wall regions (cooler regions) thus resulting in significantly thinner films on the channel floors and thicker films on the channel walls. Any attempt in increasing the thickness of the film on the channel floor by using a higher viscosity precursor solution (obtained by aging the precursor solution) resulted in ultra thick coatings on the sidewalls which eventually peeled off of the surface.



a



b

**Figure 3-8. SEM of the channel cross sections showing the non-uniform nature of the NPO coating obtained by spin coating**

4. Because of the 3D nature of the design, integrating solid core waveguides with the existing design would be a challenge for future prototypes. Solid core waveguides coupled to the liquid channels would improve the light coupling efficiency into and out of the LCW.

To overcome these design issues, the liquid core waveguide design has been modified to remove the sidewalls, and confine the liquid with only two sidewalls.

Confinement in the other sides is done through ‘virtual sidewalls’ the details of which are given in the next chapter.

## **CHAPTER 4: DEVICE DESIGN AND FABRICATION VIRTUAL CHANNEL DESIGN**

### **4.1 Improved design**

As we have seen in chapter 3, conventional microfabrication of liquid core waveguides involves etching channels in silicon/glass followed by coating of a low refractive index dielectric material and subsequent bonding with a similarly processed glass substrate. Although this design worked for liquid core waveguides employing Teflon AF as the cladding [47,48], integrating nanoporous organosilicate coatings to the design was a challenge. Thick coatings ( $> 4$ microns) of Teflon could easily be obtained by spin coating viscous precursor solutions. Because of the polymeric nature of these films, these films are resistant to cracking and peeling off. Although we have been successful in developing low stress organosilicate nanoparticle based films with refractive indices as low as 1.10 and as thick as 3 microns, integration of these films to the LCW design has still been a problem.

To circumvent these issues, a modification has been done in the basic design of the liquid core waveguide. In the improved design, the requirement of physical channels to hold the liquid is eliminated thereby eliminating the problems associated with coating these microchannels with the NPO layer. Surface tension and capillary effects alone are

exploited to form microchannels of water confined only by two physical channel walls. The other two sides of the channel are confined by ‘virtual walls’ formed by the unique design described in detail in the subsequent sections. These liquid channels are used as the light waveguides.

#### **4.1.1 Description of the new design**

The new design relies on interaction of water with patterned hydrophobic-hydrophilic regions. In this design, a substrate is patterned such that it consists of super hydrophilic regions separated by hydrophobic regions. Two such patterned substrates are aligned and placed on top of each other with a finite spacing between them such that the hydrophilic regions on substrate 1 are well aligned with the hydrophilic regions on substrate 2. When an aqueous solution is introduced at one end of the substrates, under given circumstances, the water can be forced to be confined within the hydrophilic regions through capillary forces. Thus a channel of water is formed which is confined only by two physical sidewalls –top and bottom, the other two sides of the water column can be thought of as being confined by ‘virtual walls’ owing to the surface tension of the liquid. Figure 4-1 illustrates the concept.

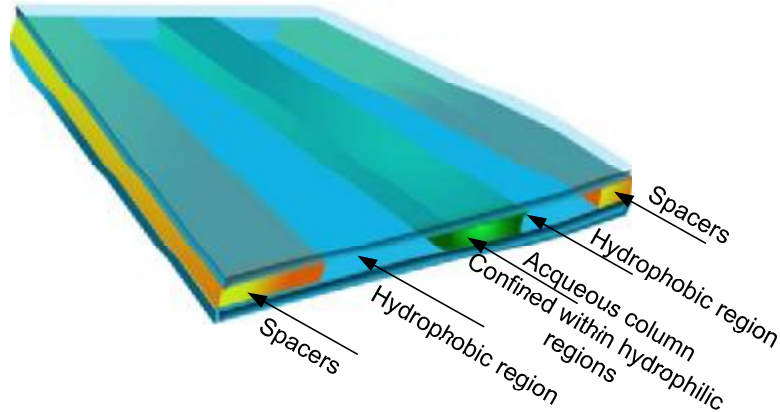


**Figure 4-1. Illustration of the confinement of the liquid column by ‘virtual channels’**

Thus, this design can be for applied for liquid core waveguides by having a coating of low refractive index material in the hydrophilic regions of the patterned substrate. Nanoporous dielectric coatings are the best choice as the surface of these coatings can be easily modified to be hydrophilic while maintaining the hydrophobic nature in the bulk film. Thus for the liquid core waveguide, the nanoporous dielectric coatings form the cladding on the top and bottom sides while the cladding on either side of the liquid column is formed by air (See Figure 4-2).

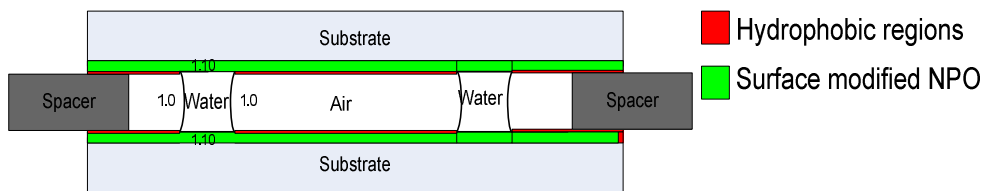


**Figure 4-2. Cross section view of the conceptual design of the liquid core waveguide**

### 4.1.2 Design considerations

Certain design considerations have to be followed in order to restrict the liquid within the hydrophilic regions and also to control the cross sectional shape of the liquid column confined within the two substrates. The details are given below.

#### 4.1.2.1 Conditions for no flow in hydrophobic regions

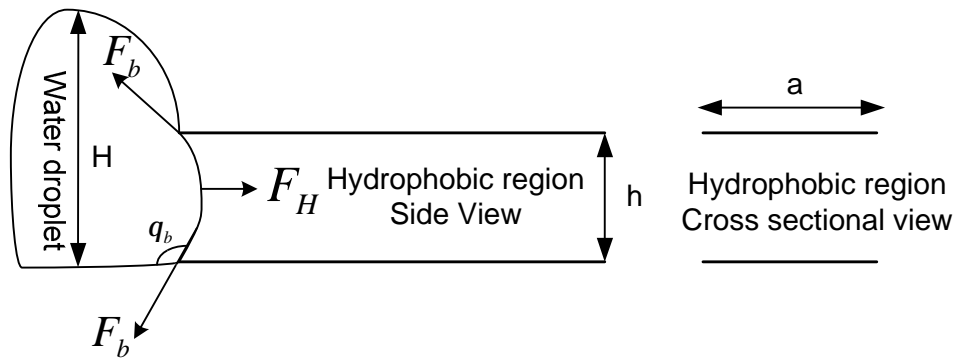


Figure 4-3. Forces acting on the liquid surface at the entrance of the hydrophobic region. The spacing between the substrates is 'h' and the width of the hydrophobic region is 'a'

As shown in Figure 4-3, the forces acting on the liquid surface at the entrance of the hydrophobic region are the capillary force acting ' $F_b$ ' and the force due to the hydrostatic pressure ' $F_H$ ' of the water droplet kept at the entrance. The respective forces are given by the expressions [49]

$$F_b = 2ag \cos(180^\circ - q_b) \quad 4-1$$

$$F_H = (\partial g H) a . h \quad 4-2$$

Where ' $g$ ' is the surface tension of the solution, ' $q_b$ ' the contact angle the solution makes with the hydrophobic surface. ' $\partial$ ' is the density of the solution and ' $g$ ' is the acceleration due to gravity. As long as the force due to the hydrostatic pressure is lower

in magnitude than the capillary force, there will be no flow of aqueous solution into the hydrophobic regions. Thus the critical condition would then be

$$H = \frac{1}{h} \left[ \frac{2g \cos(180^\circ - \theta_b)}{\partial g} \right] \quad 4-3$$

Thus having smaller gaps between the substrates requires a larger water head to induce flow within the hydrophobic regions. The discussion can be extended to the case of the water droplet at the entrance of the hydrophilic regions. In this case, the hydrostatic force as well as the capillary forces act together (in the same direction) on the liquid surface at the entrance. Thus the liquid readily fills the hydrophilic region to form the liquid column.

#### ***4.1.2.2 Curvature of the liquid column and virtual wall rupture***

The pressure within the liquid column also determines its curvature at the hydrophilic-hydrophobic regions. The pressure difference can be readily obtained from the Young-Laplace [50] equation given by

$$\Delta P = g \left( \frac{1}{R_1} + \frac{1}{R_2} \right) \quad 4-4$$

Where ‘ $\Delta P$ ’ is the pressure difference across the interface between air and the liquid column, ‘ $R_1$ ’ and ‘ $R_2$ ’ are the principle radii of curvature of the liquid surface (see Figure 4-4). The pressure inside the water column ‘ $P_H$ ’ is the hydrostatic pressure equal to the water head at the entrance of the channels (see Figure 4-3). Note that the pressure differences occurring within the liquid column between the substrates due to height are

neglected. From Figure 4-4 it can be seen that the radii ‘R<sub>2</sub>’ is infinity if we consider straight microcolumns.

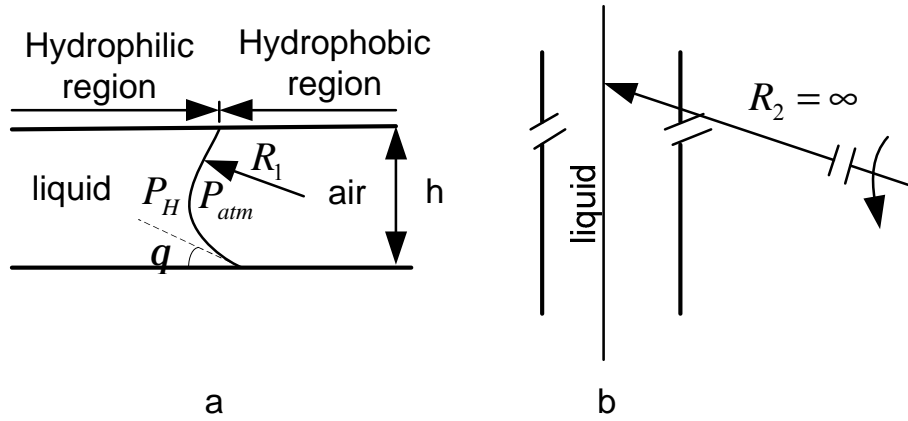


**Figure 4-4. a. Illustrates the curvature of the liquid column confined within the hydrophilic regions b. the top view of the straight column suggesting the other principle radii  $R_2$  to be  $\infty$ .**

From basic geometrical considerations, ‘R<sub>1</sub>’ can be expressed in terms of the spacing distance ‘h’ as well as the contact angle ‘q’ as

$$R_1 = \frac{h}{2 \sin(90^\circ - q)} \quad 4-5$$

Thus the expression for the pressure difference ‘ $\Delta P$ ’ can be expressed as

$$\Delta P = - \left( \frac{2g \sin(90^\circ - q)}{h} \right) \quad 4-6$$

Also, for  $q < 90^\circ$ ,  $R_1$  is negative in sign making the pressure difference ‘ $\Delta P$ ’ negative, or in other words, the pressure within the liquid column ‘ $P_H$ ’ is less than the pressure outside, ‘ $P_{atm}$ ’. Liquid columns with rectangular cross sections can be formed when the contact angle ‘ $q$ ’ =  $90^\circ$ . This condition occurs when the pressure difference ‘ $\Delta P$ ’ is zero, or in other words, by choosing the height of the liquid drop (column) at the entrance of the channels to exert a pressure equal to the atmospheric pressure. For  $q > 90^\circ$ ,  $R_1$  is positive making ‘ $P_H$ ’ positive and the profile of the liquid column (Figure 4-4a)

becomes convex from the initial concave curvature. There is however a limit on how much the angle can increase beyond  $90^0$ . Once the angle approaches the advancing contact angle of the liquid on the hydrophobic surface, ' $P_H$ ' becomes so high that the surface tension cannot hold the liquid and the virtual wall ruptures flowing the liquid into the hydrophobic regions [51]. Advancing contact angle can be explained as follows - when the liquid is added to a drop on the surface, the contact angle reaches a critical value ' $q_m$ ' and any excess liquid added after this point would spread the base of the droplet. This critical value of the contact angle is called advancing contact angle of the liquid drop on the surface [52]. The critical value of the pressure difference at which this occurs is given by the expression

$$\Delta P_{\max} = \left( \frac{2g \sin(q_m - 90^0)}{h} \right) \quad 4-7$$

Where ' $q_m$ ' is the advancing contact angle of the liquid on the hydrophobic surface.

#### ***4.1.2.3 Input ports and spacing between hydrophilic 'virtual' channels***

If the design incorporates separate input ports for each virtual channel, the spacing between the channels can be sufficiently small. However, if the device design is such that the channels are not isolated from each other by having a single input port, then the spacing between the channels have to be carefully designed. In the latter case, even with a careful design of the device with respect to virtual wall rupture and curvature, there arises a situation in which the liquid can enter the hydrophobic regions due to the capillary forces from the virtual walls of the liquid column. This situation is illustrated in Figure 4-5.

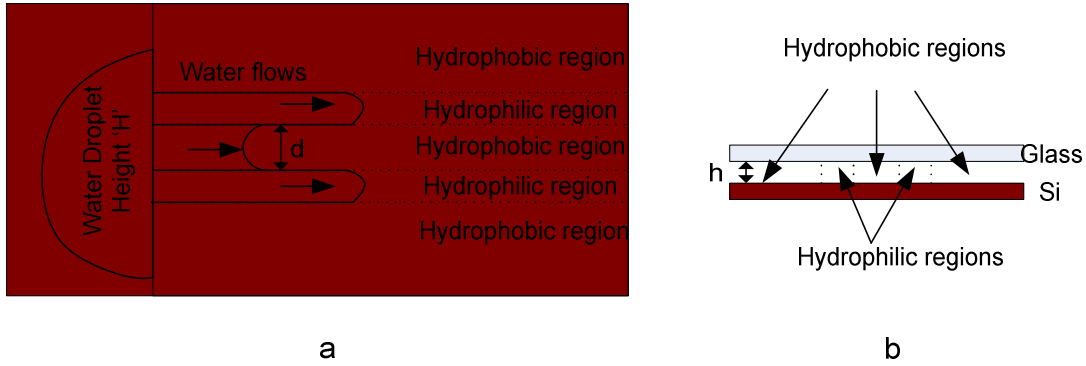


**Figure 4-5. a. Top view and b. cross sectional view of the single port device illustrating the wetting of the hydrophobic regions by water due to the surface tension forces from the virtual walls of the liquid column within the substrates.**

As in section 4.1.2.1 the forces on the liquid column at the entrance to the hydrophobic region (see Figure 4-5) are the surface tension forces due to the hydrophobic bottom and top regions, ' $F_B$ ', surface tension forces due to the liquid virtual walls on either side, ' $F_P$ ' and the force due to the pressure from the water droplet head, ' $F_H$ '. Thus for no liquid flow inside the hydrophobic region to occur

$$F_B = F_P + F_H \quad 4-8$$

or

$$2g \cos(180^\circ - q_b).d = 2g.h + (\partial gH).dh \quad 4-9$$

Or the critical value of the separation ' $d$ ' for a given spacing ' $h$ ' between the substrates and a given height ' $H$ ' of the water droplet at the entrance of the channels to prevent water flowing into the hydrophobic regions is given by the expression

$$d = \frac{2g.h}{2g \cos(180^\circ - q_b) - (\partial gH).h} \quad 4-10$$

### 4.1.3 Device fabrication

Teflon AF coatings have been used to define the hydrophobic regions. Teflon coatings with their low surface energies are hydrophobic with contact angles  $\sim 115^\circ$ . The details of patterning Teflon is are given below.

#### 4.1.3.1 Teflon patterning

Although Teflon is an ideal material for this purpose with its high chemical resistance, durability and low surface energies, patterning Teflon is nevertheless a challenge. Because of its low surface energy, photoresist doesn't stick to the surface forming highly discontinuous films. Multiple coatings (at least 3) have to be performed in order to have a photoresist coating with  $> 95\%$  coverage on the Teflon coated substrate. Even with multiple coats, photoresist merely adsorbs on the surface with no actual adhesion. Thus stresses in the film during the UV-exposure results in partial buckling of the photoresist layer in the exposed regions. This buckling gets manifested as large protrusion in the otherwise straight channels (see Figure 4-6).

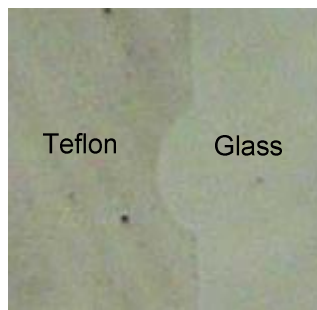


**Figure 4-6. Teflon pattern obtained by photoresist coating on Teflon, patterning and Teflon etching showing the unintended protrusions in the straight channels.**

In another approach we have attempted to use aluminum as the hard mask for Teflon patterning (similar to patterning SiC, Chapter 3). In this procedure, Aluminum

was first sputter coated on Teflon coated substrates. Photoresist was later spun coated on top of the Aluminum coating. As Aluminum had poor adhesion to the Teflon coating and better adhesion to the photoresist coating, during the pre-bake process, the thermal stresses in the photoresist coating resulted in the buckling of the whole film, including the underlying aluminum layer. Thus this approach could not be used for Teflon patterning.

Lift off process, which is a common photolithographic process for metal patterning is another approach that has been investigated for Teflon patterning. In this process, photoresist is first patterned following the conventional photolithography techniques. Metal layer is then coated on to the patterned substrate either through sputtering or metal evaporation. Following metal deposition, the photoresist coating is lifted off of the substrate by immersion in the respective solvents. Thus the metal coating that was present on the photoresist layer gets lifted off while the metal deposited in the regions with no photoresist stays.

The problem with using lift off process with polymers is that polymers tend to form continuous films unlike metal coatings on the photoresist patterned substrates. Thus lift off of polymeric films doesn't result in sharp features as in the metal lift off case. Also, for the formation of a stable well cross linked Teflon film, Teflon AF coatings have to be subjected to a high temperature heating step (temperature 330 °C) [53]. Conventional photoresists cannot withstand that temperature.

To overcome these, issues, we have used ultra thin Teflon coatings (thickness of the order 10nm) and used patterned aluminum coatings (instead of photoresist) for Teflon lift off. Aluminum can be safely subjected to the curing temperature of Teflon without the problem of degradation. Even with coatings with thickness less than 20nm, the

Teflon films displayed the same properties of low surface energies typical of bulk Teflon films. Such thin coatings of Teflon are expected to form discontinuous films on the aluminum patterns such that liftoff of aluminum results in sharp Teflon patterns on the substrate.

Having established reliable patterning of Teflon films using the lift off procedure, the process was finally applied in the fabrication of the virtual channel liquid core waveguides.

#### ***4.1.3.2 Fabrication flow chart***

The fabrication of the device starts with the deposition of nanoporous organosilicate (NPO) films (~2 microns thick) on 1”/1.5” silicon and borosilicate glass substrates. One property of the organosilicate coatings is that sputter coating aluminum on top of these films followed by chemical etching renders the surface super hydrophilic. More details of the properties of the nanoporous organosilicate coatings can be found in chapter 5. For the present design, only organosilicate nanoparticulate films have been investigated as cladding material. The wafers are cleaned through an organic wash process (see section 3.2.1). The films are then spin coated from a day old NPO precursor solution at 3000 rpm/30s followed by a high temperature heating step of 470 °C for 5 mins inside a furnace. For best results, a 1:10 diluted HF dip is performed on the silicon wafers to remove any native oxide just prior to spin coating. It has been observed that the presence of hydroxyl (-OH) groups on the substrate surface has an effect of collapsing the pores thereby increasing the refractive index of the films. For similar reason, on glass substrates, a 4nm thick amorphous silicon film is deposited prior to the deposition of the NPO coating.

The NPO coated substrates are then sputter coated with a ~ 330 nm aluminum layer. The substrates are now ready for patterning. Channel patterns are fabricated on top of the Aluminum coated substrates using a positive photoresist (S1813). The masks for the fabrication of the channels is shown in **Error! Reference source not found.** The channels to be fabricated are 500 micron in width. The thick bars on either end (1mm wide) will be used for alignment of the bottom (silicon) to top (glass) substrates for the final device.

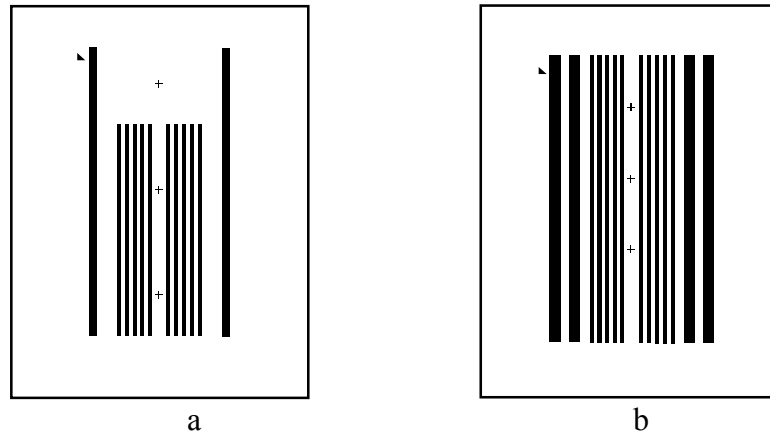


**Figure 4-7. Mask design for patterning Channels on a. Silicon substrates, b. Glass substrates**

The fabrication flow chart for the process is given in Figure 4-8. After patterning the photoresist with the above masks, the substrates are dipped in an aluminum etchant solution (refer section 3.2.1) to pattern the aluminum coating. At this point the channels to be used for the liquid core waveguide are the central regions containing aluminum strips (the black portions of Figure 4-7). Photoresist is then washed off with acetone following the aluminum etch. In order to prevent etching of the aluminum bars to be used for substrate alignment in the subsequent steps, photoresist is carefully applied onto them with a cotton bud.

For Teflon patterning, the aluminum patterned substrates from the previous step are first coated with a thin (monolayer) of FSM (0.4% fluoro silane coating, FSM 660, 3M Corp.) and baked at 95 C for 10 mins as prescribed by the manufacturer. A 0.05 % Teflon solution (Teflon AF 1600) is prepared in FC 75 solvent (3M Corp.) and films are spin coated at 3000 rpm for 30s to obtain ultra thin coatings of Teflon (< 10nm thick). A 0.5 % Teflon coating prepared in similar way gave a thickness of 40 nm. The surface properties are characteristic of Teflon surfaces, having contact angles with water ~ 115 degrees. The substrates are then heated at 135 C for 5 mins, 225 C for 5 mins and 300 C for 10 min steps to cure Teflon and improve its adhesion properties with the substrates. After the heat treatment step, the substrates are allowed to cool down before being taken off from the hot plate for further processing.

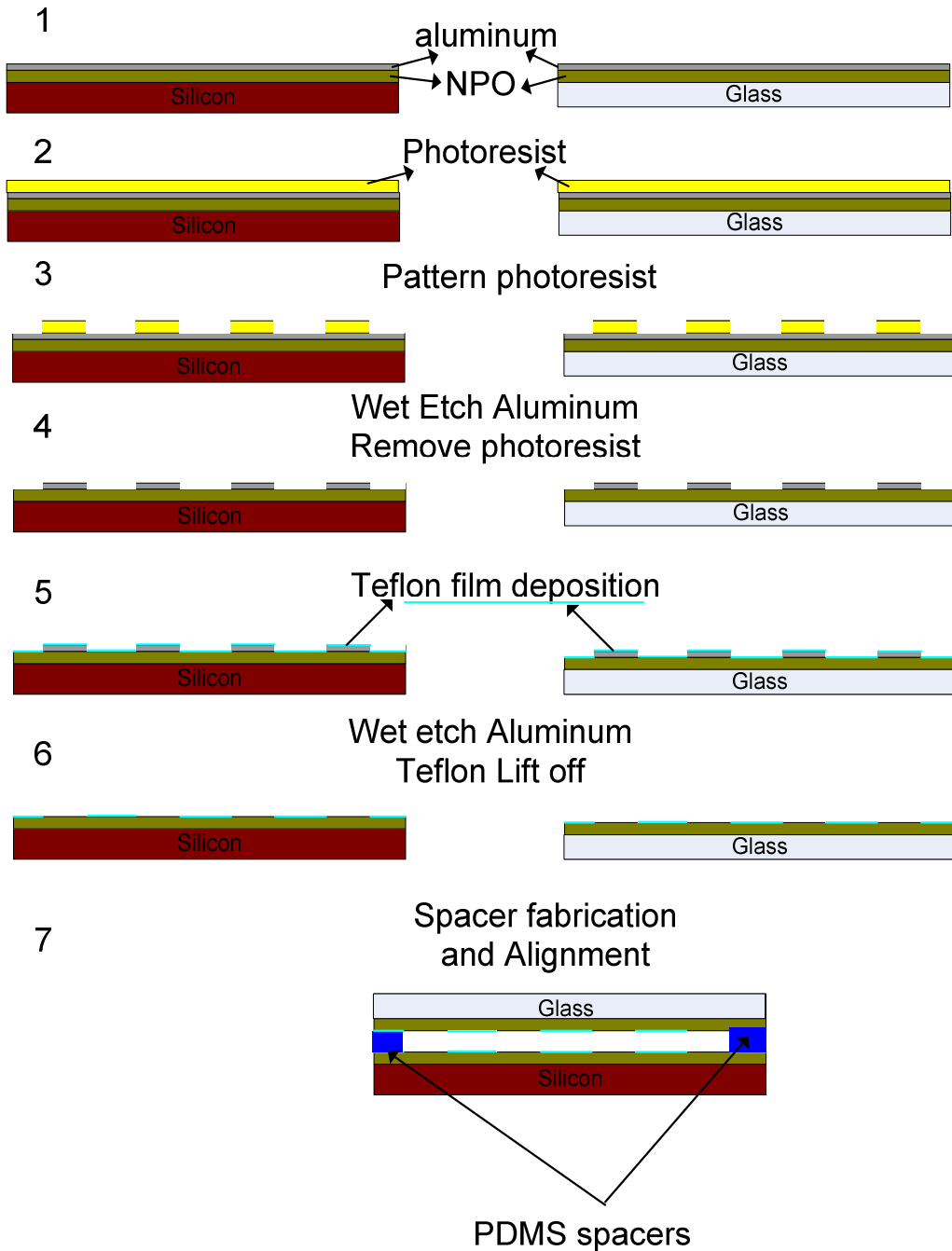


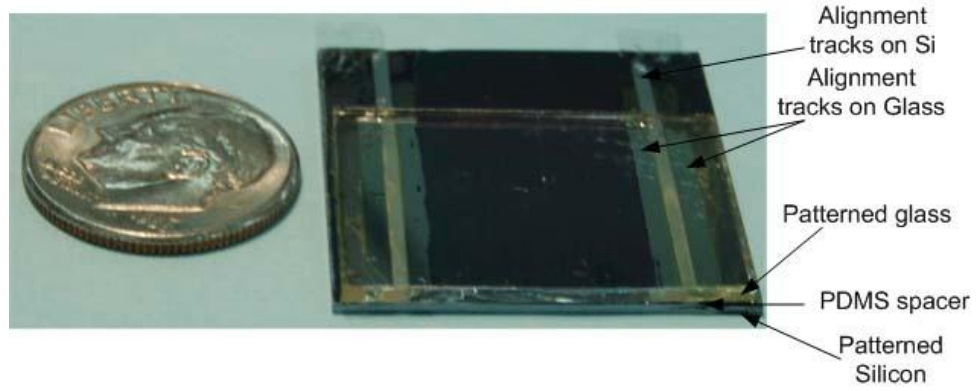
**Figure 4-8. Fabrication flow chart for the new LCW design**

The Teflon coated substrates are later dipped in the aluminum etchant solution to lift off aluminum thereby patterning Teflon. Also, the regions on the NPO coating that are not exposed to Teflon are rendered superhydrophilic with the etching of aluminum stripes. Thus the NPO substrate is patterned to have superhydrophilic regions (the central

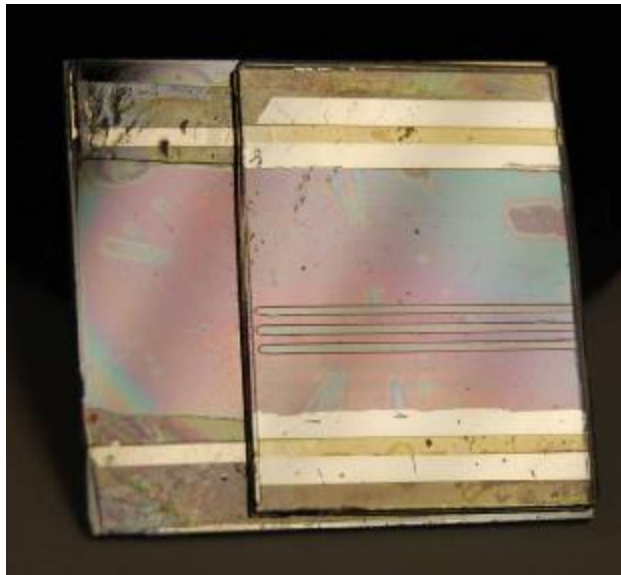
black stripes of Figure 4-7) separated by hydrophobic Teflon coated regions. The next step in the fabrication of the device is the spacer fabrication.

For the present prototypes, Polydimethylsiloxane (PDMS) spacers were fabricated and used. For the future devices, SU 8 spacers will be utilized such that the SU 8 waveguides coupling the liquid core waveguide as well as the spacers will be fabricated in a single lithography step. For the fabrication of the PDMS spacers, an adhesive tape of known thickness was used and stuck around the perimeter of a glass substrate to form a well of depth defined by the thickness of the adhesive tape. 1:10 PDMS mix was then poured into the well. Excess PDMS was carefully removed by traversing a flat blade across the surface of the glass substrate such that the level of PDMS in the well was flush with the top of the adhesive tape. PDMS within the well was later cured in a convection oven at 70 °C for 10 mins. PDMS was chosen in this case as the surface of PDMS is tacky which would prevent substrates from moving once they were aligned.

After curing, PDMS was carefully cut as rectangular stripes and carefully kept on the surface of the alignment bars on the silicon substrate. The glass substrate was cleaved into two halves and one of the half was carefully aligned and kept on top of the silicon substrate by using the alignment bars on the silicon and glass substrates. Figure 4-9 shows the picture of the final device.



a



b

**Figure 4-9 a** Picture of the final device with PDMS spacers **b.** picture of the device with DI water filled channels.

## **CHAPTER 5: RESULTS AND DISCUSSION**

### **5.1 Overview**

This chapter presents the results obtained from the processing of different nanoporous dielectrics. Ordered nanoporous silica, Nanoporous organosilicate films by porogen approach and nanoporous organosilicate nanoparticulate films have been investigated for application as the cladding material. Organosilicate nanoparticulate films in particular displayed some unique properties. These films were studied for their electrical and optical properties. Nanoindentation studies was performed to obtain the mechanical strength of these films. The films were also investigated for applications as high surface area films for biological probe immobilization. The high surface area of these films together with easy surface functionalization yielded high density of immobilization.

Two designs of the liquid core waveguide was considered and experimented with utilizing the organosilicate nanoparticulate films as cladding materials. The waveguide performance with respect to transmission losses are presented for both the designs.

## 5.2 Nanoporous dielectrics

We have worked on the preparation of the nonporous dielectric films employing the methods outlined in chapter 2. The experimental details of the preparation method are given in chapter 2. Thickness and refractive index measurements on the nanoporous dielectric films were performed with Variable angle spectroscopic ellipsometer system (VASE, JA Woollam).

### 5.2.1 Ordered Nanoporous silica (ONPS) films

Following the experimental methods outlined in chapter 2, films with Thicknesses 200 – 1500 nm and refractive index of 1.19 – 1.24 have been obtained. Figure 5-1 shows planar and cross-section TEM images of the spin-coated and dip-coated films. The spin coated films show randomly oriented (Figure 5-1a) pores and partial ordering with 3 nm pore diameter (Figure 5-1b). The dip-coated films on the other hand (Figure 5-1c) are highly ordered with a regular spacing of 2.2 nm between pores throughout the coating thickness (Figure 5-1e), The pore diameters for this film is 1.5 nm.

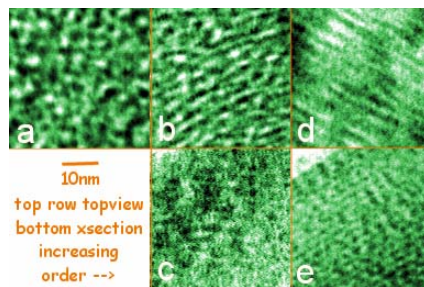
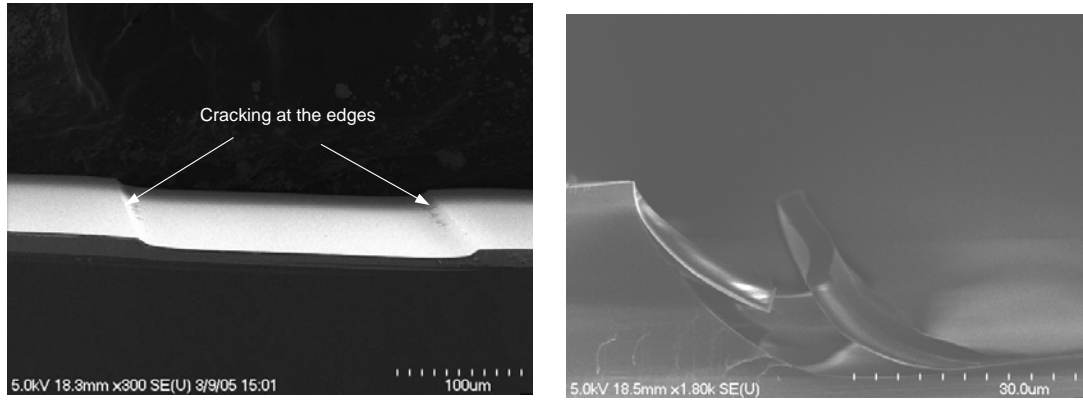


**Figure 5-1 Planar and cross sectional TEM images of the a ,b spin coated and c,d,e the Dip coated ONPS films**

For the fabrication of thick films as required for the liquid core waveguides, we have increased the viscosity of the precursor solution by solvent evaporation by keeping the solution in an open beaker inside an oven at 70 °C for evaporation. The evaporation was typically carried out until a 50% reduction in volume was obtained. Thicker films were obtained with thicknesses 1 micron to 1.5 microns and a refractive index of 1.19-1.22.

#### ***5.2.1.1 ONPS films as cladding material (Design 1)***

Ordered nanoporous silica films have been attempted to be used as the cladding material for the waveguides. Because of the ordered arrangement of the pores, these films were expected to have better mechanical strengths compared to the random nanoporous films. However these films suffered from the fact that the refractive index could not be tailored to be lower than 1.19. Higher CTAB/TEOS ratio would result in the collapse of pores, increasing the overall refractive index of the film greater than 1.20. Also, these films suffered from cracking when the thickness of the films was increased to be more than 1.2 – 1.3 microns. During the dip coating process of the channels, the channel edges invariably have thicker coatings (due to the edge effect) resulting in increased stress in the film in those areas. This resulted in cracking and/or delamination of the films from the channel surface. Figure 5-2 gives both the instances.



a b

**Figure 5-2. SEM pictures of ONPS coating in the channels a. cracking in the channels, b. delamination of the films from the channels**

Further, additional processing steps had to be performed on these films to render them hydrophobic. This motivated us for the search for alternative routes for the fabrication of low stress (crack free) ultra low refractive index nanoporous dielectric films.

### 5.2.2 Nanoporous dielectric films through sacrificial porogen approach

We have obtained thicknesses of  $\sim 500$  nm and a refractive index of 1.24-1.27 following the experimental procedures mentioned in chapter 2. The obtained films were further characterized by the contact angle method. A water droplet  $\sim 5$  microliters was dispensed on top of the film and a CCD camera with a zoom lens was used to capture the image.





clearly visible that there is a very narrow distribution of the size of the obtained nanoparticles.

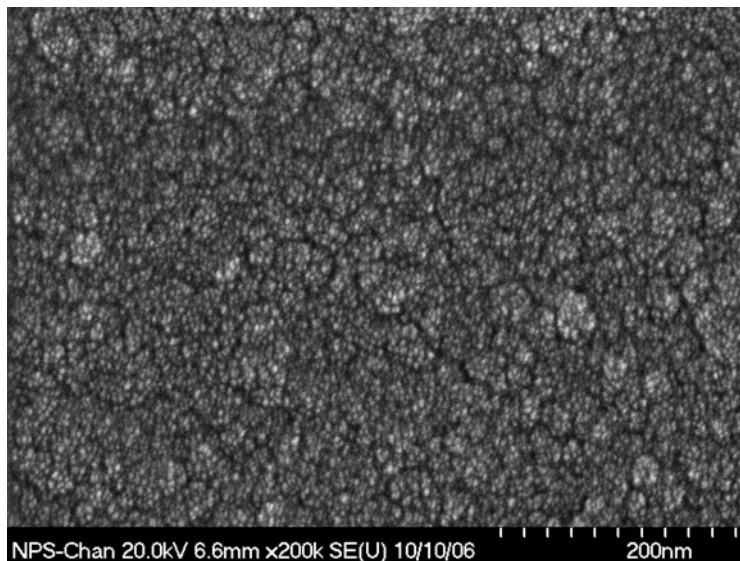


**Figure 5-4. High resolution SEM picture of the obtained nanoporous PMSSQ particulate based film.**

#### ***5.2.3.1 Mechanical Strength of the films***

It is well known that the mechanical strength of nanoporous materials depends on the porosity of the final matrix. Highly porous matrices are expected to suffer from very low mechanical strengths. However, as it can be seen from Figure 5-4 the unique morphology of these films, consisting of a stack of nanoparticles (of 2-5 nm) is expected to improve the mechanical strength of these films. Nanoindentation technique (TriboIndenter, Hysitron Inc.,) was used to study the mechanical properties of the film. Given below are the results of the measurement.

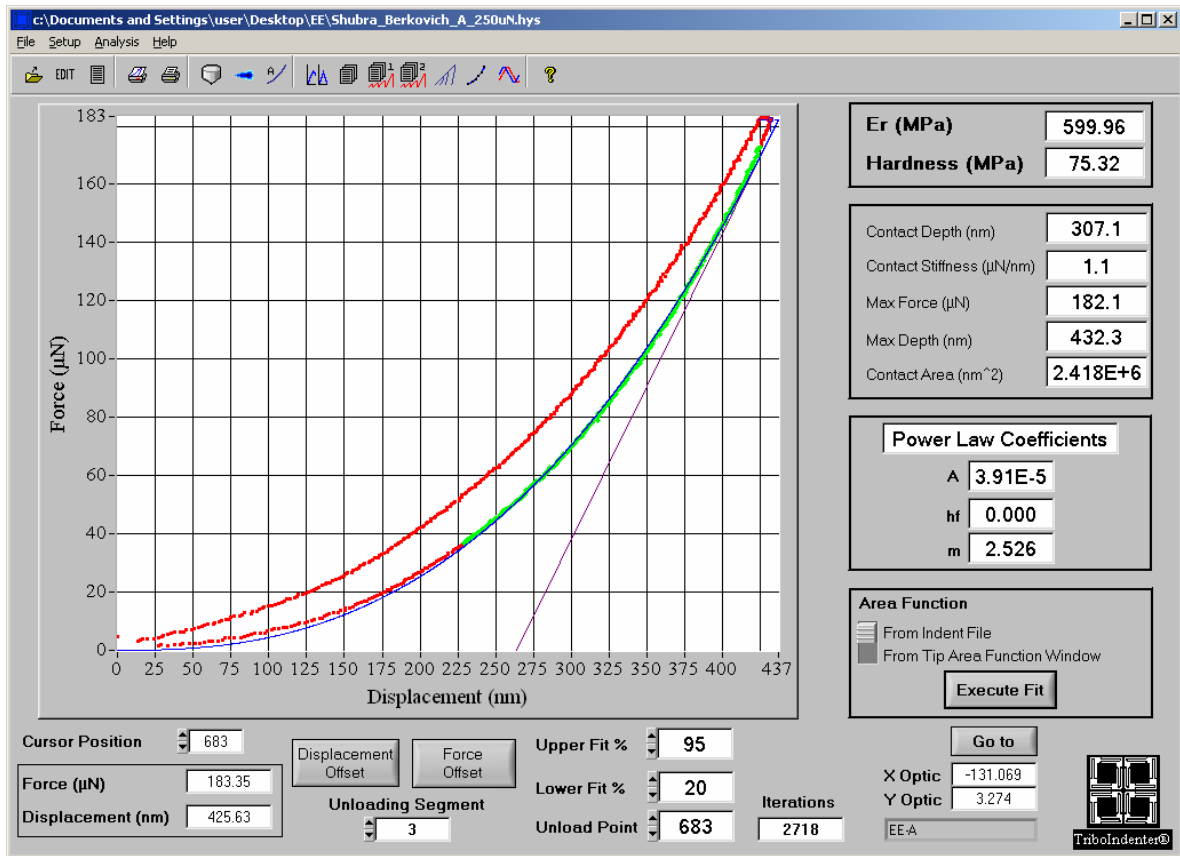


Figure 5-5. Results of the nanoindentation test on the films.

The Elastic modulus of the film has been deduced from the following equation (from contact mechanics)

$$\frac{1}{E_r} = \frac{(1 - \nu_i^2)}{E_i} + \frac{(1 - \nu_s^2)}{E_s} \quad 5-1$$

$E_r$  is the reduced modulus of Elasticity = 599.96 MPa (from the measurement)

$\nu_i = 0.07$  (for a diamond Tip)

$E_i = 1140$  GPa for the Diamond tip

$\nu_s =$  Poissons Ratio for the MSQ based material = 0.26 [54]

$E_s =$  Modulus of Elasticity for the material

From equation 5-1, the modulus of Elasticity for these films was calculated to be 0.56 GPa. It is well documented that the modulus of the nanoporous films drop rapidly with increasing porosity. The drop has been reported to be from 9GPa (2.5% porosity) to 0.6 GPa (50% porosity)[54]. Thus in comparison to the nanoporous films prepared by the porogen approach of the same porosity (70%), these films are higher in modulus and thus expected to be more robust.

### **5.2.3.2 Dielectric constant**

Electrical characterization of these films has been performed in a probe station on the metal/insulator/metal (MIM) structures at room temperature. Capacitance-voltage (C-V) measurements were carried out using an HP 4284A LCR meter at frequencies 100 kHz and 1 MHz. Nanoporous dielectric films were deposited on heavily doped, electrically conductive silicon substrates from one day aged solution. Aluminum dots were then sputter coated on these films through a shadow mask. Dielectric constant measurements performed in this manner gave a value of 1.4 at 100 KHz and 1.42 at 1MHz. The diameter of the aluminum dot (top contact) being 500 microns. Figure 5-6 C-V curves for the Nanoporous dielectric MIM structures at two different frequencies on dot1 (500 micron diameter) Aluminum dot.

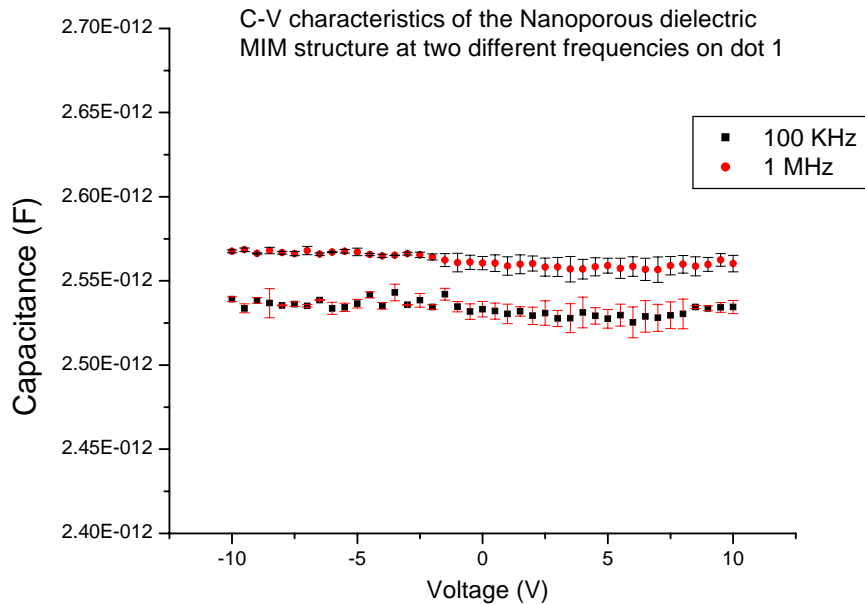


**Figure 5-6 C-V curves for the Nanoporous dielectric MIM structures at two different frequencies on dot1 (500 micron diameter)**

### 5.2.3.3 Surface treatment of the NPO films

#### 5.2.3.3.1 Hydrophobic to hydrophilic conversion

These films offer some unique surface properties and the surface modification of these films to render them hydrophilic or hydrophobic have already been established in our labs. Conventional techniques of surface modification of such films involve oxidation of the surface to introduce silanol groups by exposure to oxygen plasma. We have developed a new modification technique which doesn't require any oxygen plasma treatment of the films. Aluminum film deposition on these films followed by wet chemical etching of aluminum has been observed to render these films hydrophilic. Contact angle picture of a water droplet on top of the NPS film surface is shown in Figure 5-7a. Figure 5-7b clearly illustrates this. The contact angle changes from 110 degree to less than 10 degrees with this treatment. Ellipsometer results show that the

treatment does not have a significant effect on the thickness and the refractive index of the NPS film.

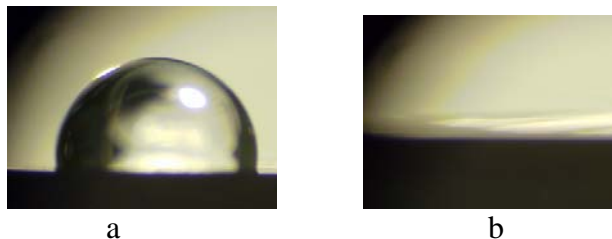


**Figure 5-7. Contact angle picture of a water droplet on the a. As prepared NPS surface showing that the surface is hydrophobic b. Aluminum surface treated NPS**

Aluminum deposition and etching process was similar to the process mentioned in chapter 3. The samples were sputter coated with Aluminum to obtain a thickness of 130nm. The conditions used for the sputtering process are as follows – D.C power of 200 W, base pressure of  $10^{-6}$  bar, argon flow 20 SCCM. The film is either rendered hydrophilic during the sputter coating during the initial few seconds of argon ion bombardment or we hypothesize that after the aluminum etching, there still remains a very thin Aluminum layer adsorbed on top of the NPO film which is oxidized rendering it hydrophilic. The aluminum etchant solution by itself did not have any effect with regard to the surface properties of the NPO films no introduced to the sputtering chamber. Two sets of NPO films were prepared. On the first set, a 130 nm thick Aluminum layer was sputter coated while no coating was done on the second set. Both the films were dipped in the Aluminum etchant solution and kept till aluminum coating etched away completely from the first set.

Contact angles and ATR FTIR data was taken. While the contact angle of the first film changed from 110 degrees to less than 10 degrees (See Figure 5-7), the contact angle for the second film did not change considerably. The hydrophobic nature of the film

surface must have prevented the acidic aqueous based etchant from entering inside the pores. Figure 5-8 shows the ATR FTIR plot of the NPS surface after various treatments. It can be clearly seen that the methyl groups are present after all the treatments. Thus only the top few nanometers of the film was modified to be hydrophilic while the bulk of the film with a predominant Si-CH<sub>3</sub> bonds remains hydrophobic. This property was well utilized in the “virtual channel” design of the liquid core waveguides basically saving on an extra fabrication step.

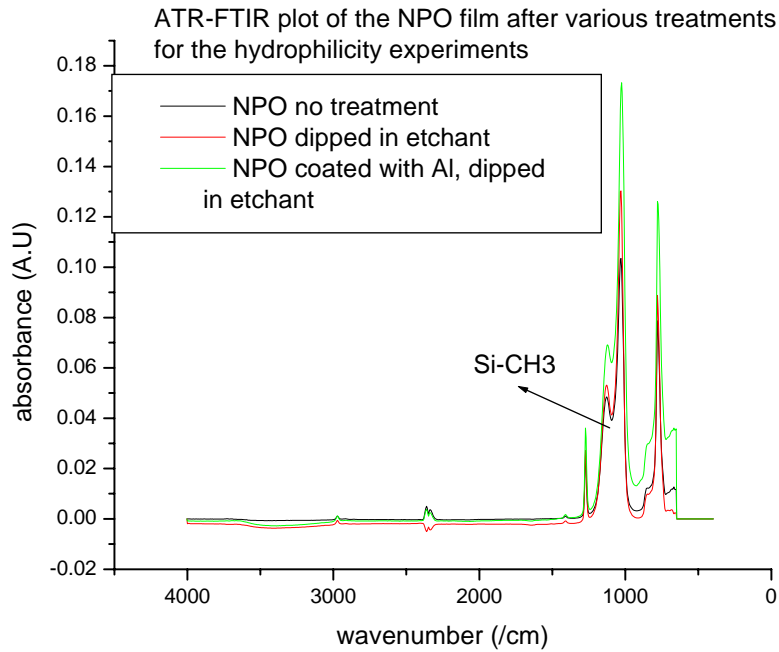


**Figure 5-8. ATR-FTIR spectra of the NPS films after various surface treatments**

#### 5.2.3.3.2 Plasma treatment of NPO films

It has been observed that the coating morphology of the NPO films in the channels (LCW design 1) improved when the channels were coated with a thin NPO layer [55], low power oxygen plasma treated [56] and immediately spin coated with the regular NPO coating. The plasma treated thin NPO layer acts like an adhesion layer for

the thick NPO coating thus improving the film coverage in the channels. However, this treatment has been shown to collapse the pores for on the top NPO layer. The refractive index has been found to increase tremendously by this treatment step. Table 5-1 gives the refractive index and thickness values of films prepared by normal deposition process and on plasma treated NPO surface.

**Table 5-1 Refractive index and thickness of films with and without adhesion layer**

Sample	Adhesion layer	Annealing conditions	Thickness	Refractive index
1	No	Hot plate 470 C 5 mins	760 nm	1.149
2	Yes	Hotplate 470 C 5 mins	1150 nm	1.37
Adhesion layer		Hot plate 470 C 5 mins	201	1.38

Hence this technique couldnot be used to improve the NPO coating morphology within the silicon channels. Alternative means of improving the coating coverage within the channels was by aging the solution to the point when it comes viscous and sticky and using this solution to coat the channels.

Selective exposure to oxygen plasma of the thin NPO coating followed by the regular NPO film deposition would give a surface with varying refractive indices. This aspect can be utilized for the preparation of buried solid core waveguides or preparation of buried nanoporous organosilicate channels for molecular level filtering applications.

#### **5.2.3.4 Surface functionalization**

The NPO films because of its nanoparticulate nature feature a large surface area. This large surface area could be utilized to obtain higher density of chemical/biological functionalization on these surfaces as against functionalization on regular (glass/Si)

substrates. Also because of the organosilicate framework, these surfaces could be easily functionalized with existing techniques. In order to experimentally verify this, fluorescently labeled protein molecules were successfully immobilized on the NPO coated and uncoated substrates and the intensity of fluorescence was compared. The immobilization procedure is described below –

Organic cleaned Silicon and Piranha cleaned borosilicate glass substrates were used for the experiments. A ~ 4nm thick amorphous silicon layer (deposited by a PECVD process) was coated on the piranha cleaned glass substrates prior to the NPO deposition. NPO films were later deposited on these substrates following the procedures outlined in section 2.5.3. For this set of experiments, PMSSQ from Technoglas was used for NPO precursor preparation which was specified to have 14-16% silanol content. The coated substrates were sealed under vacuum for further use.

The first step in the immobilization protocol is the surface modification of the substrate surfaces to incorporate a thiol functionality (-SH group). This is accomplished by reacting the surface with MPTMS (Mercaptopropyl trimethoxy Silane). Self assembled monolayers (SAMS) ending in thiol groups can be formed by reacting these molecules with the hydroxyl groups on the substrate surface (see Figure 5-9).

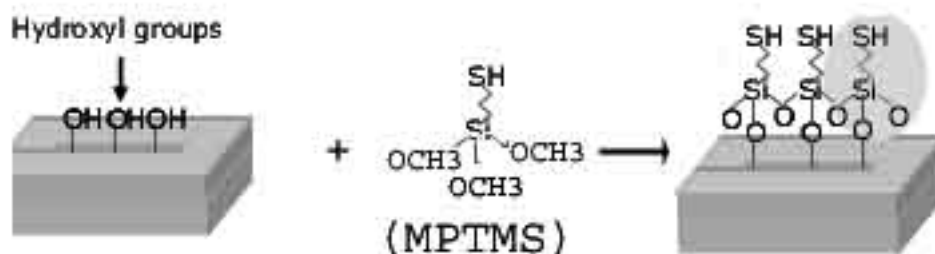


**Figure 5-9. Surface functionalization to obtain -SH functionality a. Untreated surface with predominant hydroxyl groups, b. MPTMS treated substrate**

The organosilicate surface predominantly consists of Si-CH<sub>3</sub> groups. Thus these surfaces should be first primed to obtain hydroxyl groups (-OH). A mild oxygen plasma treatment of the NPO films renders them hydrophilic by replacing the Si-CH<sub>3</sub> groups on the surface with Si-OH. For these set of experiments, the oxygen plasma treatment was typically done for 35 seconds at an RF power of 12 W and a base and working pressures of 90 and 880 mTorr. Following the treatment, the contact angle drops from 110 degrees to less than 10 degrees.

The oxygen plasma treated NPO samples are then treated with MPTMS by placing them in a 2% by volume solution of MPTMS in Toluene. The substrates are incubated for 90 mins under a nitrogen environment. Following the incubation step, the substrates are repeatedly rinsed with toluene and dried with nitrogen.

Protien A/ AF546 (protein A molecules tagged with Alexa Fluor 546) molecules have been used for the immobilization studies. In order to immobilize the protein A molecule, an intermediate crosslinker GMBS [N-(g-Maleimidobutyryloxy)succinimide ester] is needed, one of which bonds to the -SH bonds on the substrate and the other other end bonding to the protein A molecule. The bonding of the GMBS molecule was done by dissolving GMBS in ~ 50 µl of DMF (*N,N*-Dimethylformamide). The dissolved GMBS was added to ethanol to create a 2mM GMBS solution. The -SH functionalized substrates were placed in this solution for one hour at room temperature (care was taken to prevent the evaporation of ethanol). The substrates were later rinsed with PBS (phosphate buffered saline) buffer to remove excess GMBS from the surface.

The protein immobilization was done by placing approximately 200 - 400  $\mu\text{l}$  of 35 $\mu\text{g/ml}$  Protein A/AF546 on top of the substrates from the previous step. The substrates were incubated overnight at 4 $^{\circ}\text{C}$ . Following the incubation, the substrates were rinsed thoroughly with PBS buffer. In the final step, 3% BSA (Bovine serum albumin) in PBS solution was kept on top of the substrates for 1 hour following which the substrates were washed with PBS and kept immersed in fresh PBS for future analysis.

Flourescence spectra of the samples were taken with a Jasco spectrofluorometer. A custom holder was used to mount the samples such that the samples were placed at an angle 33 $^{\circ}$  with respect to the excitation source. Figure 5-10 illustrates the set-up.

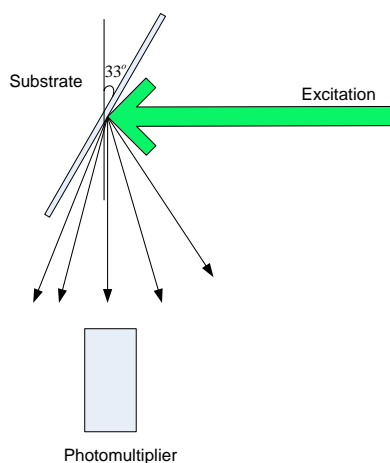


**Figure 5-10. Experimental set-up for the measurement of fluorescence from the protein A/AF546 tagged substrates**

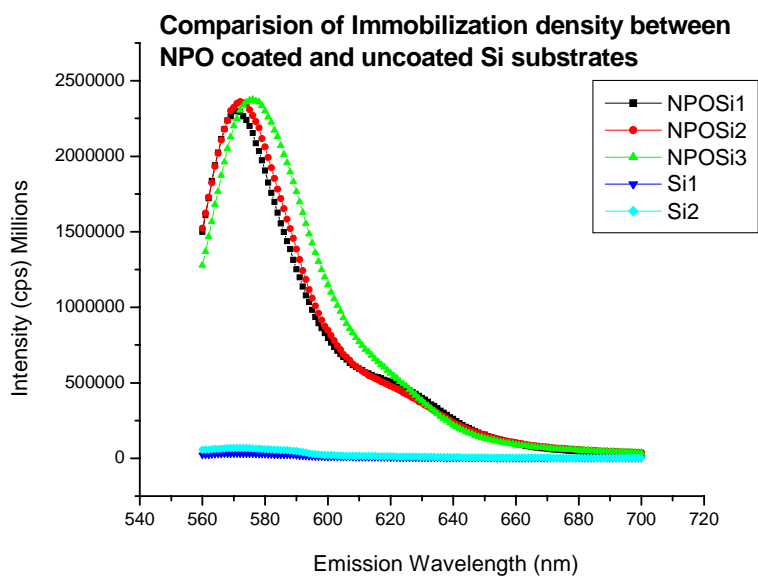
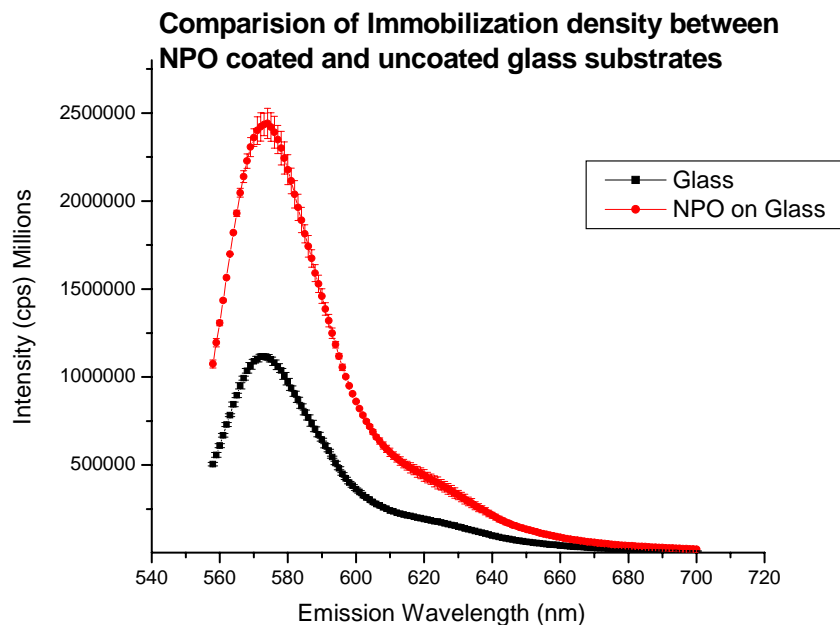


**Figure 5-11. Fluorescence emission spectra of Immobilized protein A/AF546 on a. NPO coated and uncoated glass substrates (note that there is a thin coating of amorphous silicon ~ 4nm thick between the glass and the NPO layer) b. NPO Coated and uncoated Si substrates**

The plots clearly indicate that there is a huge increase in the density of immobilization in the case of the NPO coated substrates. This is especially true for silicon substrates as the number of hydroxyl groups on a silicon substrate would be less in comparison to the glass substrates. Therefore the density of immobilization of MPTMS on the substrate also decreases.

#### ***5.2.3.5 PMSSQ nanoparticles based nanoporous dielectric films as cladding***

The films produced by this method were the most stable of all the nanoporous dielectric films investigated as liquid core waveguide cladding. Thick, smooth and crack free films with thicknesses in excess of 3 microns were obtained. As we have seen in Figure 5-7 these films are hydrophobic thus additional surface treatments are not necessary. An extensive study on tailoring the refractive index of the films has not yet been done but we believe that it is possible to tailor the refractive index of these films by varying the processing parameters. The channels are coated with this material through spin deposition technique. Figure 5-12 shows the nanoporous dielectric coating by this method.

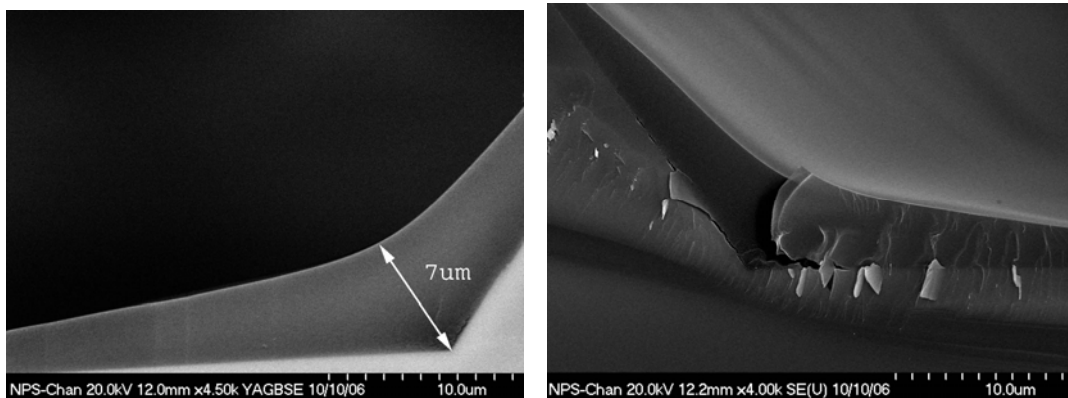


**Figure 5-12. Cross sectional view of a channel etched in silicon and coated with the PMSSQ nanoparticle based nanoporous dielectric.**

#### 5.2.4 Liquid Core waveguide characterization

For the characterization of the waveguides, the channels were first filled with fluorescein dye and transversely illuminated with a Blue LED light (470 nm wavelength). A microscopic objective (20X) was used to focus the light onto the channels. The excitation source was moved through the length of the waveguide and the fluorescence counts were recorded using a spectrometer (Ocean Optics, USB 4000). A 600 micron core fiber optical cable coupled to one end of the channels was used to collect the fluorescence signal from the waveguide into the spectrometer. Figure 5-13 gives a picture of the experimental set-up. The equation governing the intensity of the fluorescent light collected at a distance 'x' from the origin of fluorescence is given by Beer-Lambert's law [57] as

$$I(x) = I_0 e^{-(\alpha+\beta)x} \quad 5-2$$

Where,  $I(x)$  is the intensity of the collected light at a distance 'x' from the origin of fluorescence.  $I_0$  is the intensity at the origin. For the present experiments, 'x' is the horizontal distance between the transverse illumination source and the output end of the waveguide (coupled to the optical fiber). ' $\alpha$ ' is the molar absorption coefficient of the dye solution at the emission wavelength (due to re-absorption, expressed as  $\text{cm}^{-1}$ ) and ' $\beta$ ' is the intrinsic loss coefficient of the waveguide due to imperfections.

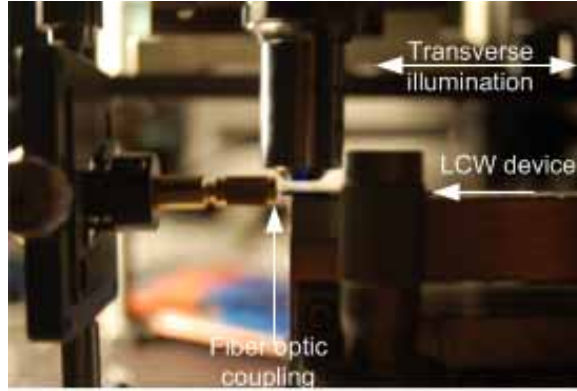


**Figure 5-13. Experimental setup for loss characterization of the liquid core waveguide**

' $\alpha$ ' is obtained from the UV-Vis spectra from the absorbance values of the dye solution (of a particular concentration 'c' due to re-absorption) at a given wavelength (For the loss measurements, the absorbance values are read at the emission wavelength of the dye).

' $\alpha$ ' is given by

$$\alpha = \frac{A}{l} \quad 5-3$$

Where 'A' is the absorbance of the solution at a specific wavelength and 'l' is the path length of the cell (= 1cm for standard cuvettes). The exponent ' $\alpha + \beta$ ' of equation

$$I(x) = I_0 e^{-(\alpha+\beta)x}$$

5-2 is then the slope of the linear fit between the natural logarithm values of the obtained intensities at different positions of the excitation source and the position 'x'. Thus ' $\beta$ ', the intrinsic loss of the LCW can be obtained once ' $\alpha$ ' is known. Note that ' $\beta$ ' is expressed as  $\text{cm}^{-1}$ . To obtain loss in dB, the following conversion factor is used [58]

$$\beta_{dB} = 4.34\beta \quad 5-4$$

#### 5.2.4.1 LCW characterization – 'physical channel' design

NPO coated silicon channels and glass substrates were stacked together and a tape was applied across the back of the silicon substrate, clamping it to the glass substrate. Care was taken to well align the channel end edges of the substrates during the application of the adhesive tape. Holes of 1mm diameter were then drilled laterally to a depth of approximately 1mm along the channel length. Figure 5-14 illustrates the set-up.

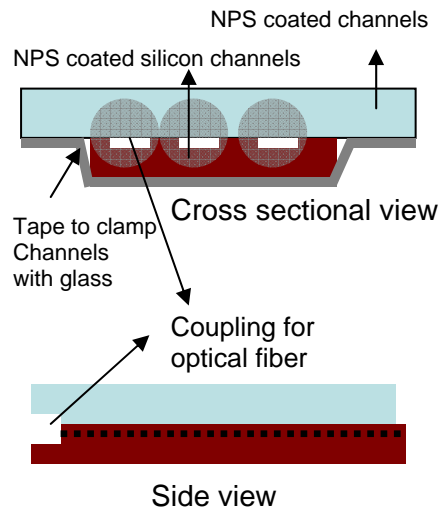


**Figure 5-14 Arrangement of the LCW device for loss characterization.**

Waveguide loss characterization has been performed on these waveguides by filling the channels with  $0.5 \mu\text{M}$  Fluorescein dye. The plot of the fluorescence intensity from the output of the waveguide as a function of the distance of the excitation source from the output end of the waveguide is given in Figure 5-15. From the linear fits of the data, the loss was measured to be  $1.56 \text{ dB} \cdot \text{cm}^{-1}$  for the coated channels and  $6.94 \text{ dB} \cdot \text{cm}^{-1}$  for the uncoated ones. Note that the absorption coefficient due to re-absorption for the  $0.5 \mu\text{M}$  fluorescein dye was too low to be accounted for.

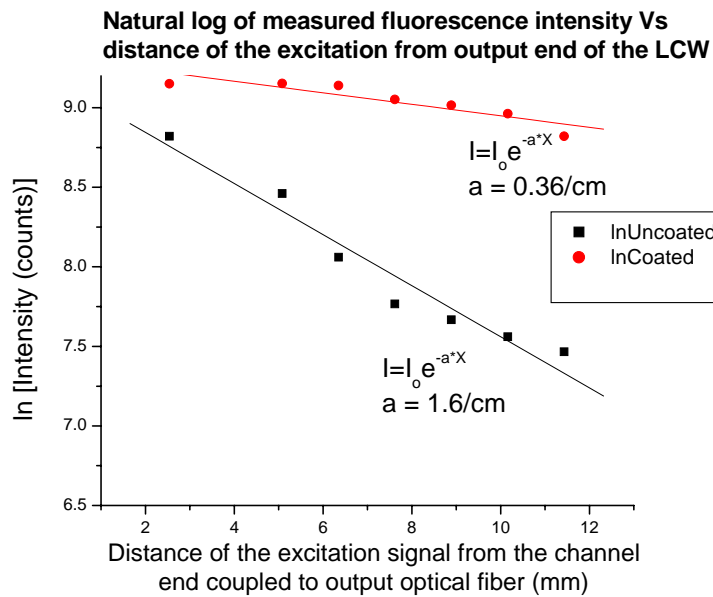


**Figure 5-15. Waveguide loss characterization plot – Design 1**

#### 5.2.4.2 LCW characterization – ‘Virtual channel’ design

For these experiments, a PDMS spacer having a thickness of 150 microns (as defined by the adhesive tape) was used. The top and the bottom substrates were carefully aligned and placed on top of each other separated by the PDMS spacers. Loss characterization of the waveguides was performed by filling the channels with a 0.05 mM concentration fluorescein dye. Approximately 10  $\mu$ l of the dye was taken and introduced into the hydrophilic channels of the waveguide. Capillary action from the hydrophilic channels together with the hydrostatic force pushes the solution to completely fill the channels. The waveguide effect is illustrated in Figure 5-16. The waveguide was illuminated transversally and the illumination source was moved across the width of the device from right to left, traversing three liquid channels in the process.

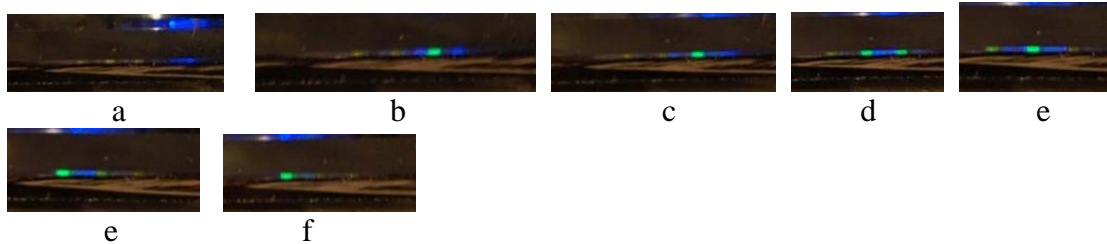


**Figure 5-16. Illustration of the waveguiding effect. The illumination of the channels was performed transversally and the light source was moved across the width of the device from right to left traversing three liquid columns in the process.**

The plot of the loss characteristics of the waveguide is shown in Figure 5-17. From the linear fit of the data, the loss coefficient was obtained to be  $0.139 \text{ cm}^{-1}$ . The absorption coefficient for the .05 mM Fluorescein solution was measured to be  $0.021 \text{ cm}^{-1}$  at 528nm wavelength (Emission peak of the solution) from the UV-Vis spectra. Thus the intrinsic loss of the waveguide was calculated to be  $0.118 \text{ cm}^{-1}$  or  $0.51 \text{ dB.cm}^{-1}$ .

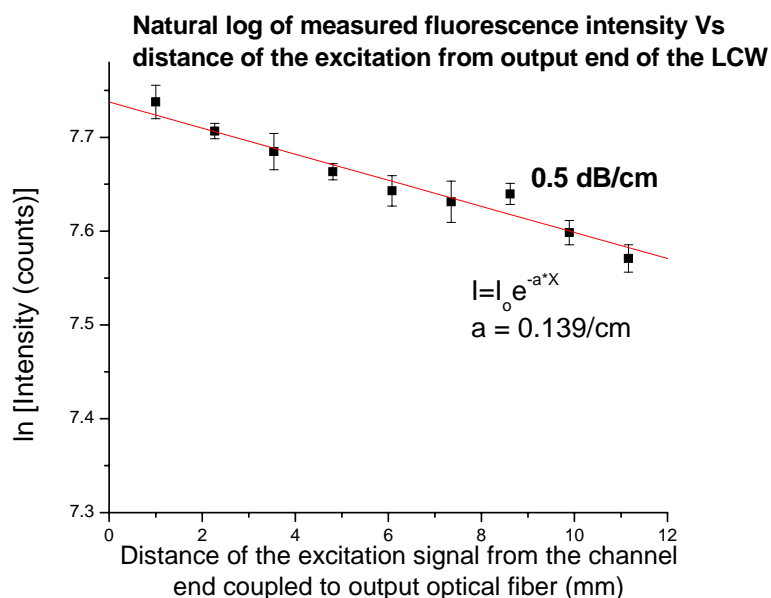


**Figure 5-17. Waveguide loss characterization plot – Design 2**

## **CHAPTER 6: CONCLUSIONS AND FUTURE RESEARCH**

### **6.1 Conclusions**

A novel method for the rapid formation of ultra low – refractive index, thick and smooth nanoporous dielectric films based on PMSSQ nanoparticles has been presented. The unique surface properties and the morphology of these films make them attractive for applications as a cladding material for liquid core waveguides. The obtained films are naturally hydrophobic thus requiring no additional surface treatment steps. We have shown that the large surface area arising from the unique surface morphology together with the easy functionalization of the film surface with existing methods can be exploited for larger density of immobilization of biomolecules. Furthermore, we have shown that these films have a greater mechanical strength owing to its nanoparticulate structure than same porosity nanoporous dielectric films obtain by porogen extraction method. The ultra low dielectric constant of these films is attractive for the semiconductor and the flexible electronics industries.

We have successfully integrated these novel coatings into the design of the on-chip liquid core waveguide system. We have tested two designs of the LCW system, one with physical channels and the other, an improved version, with virtual channels for liquid containment. The loss characteristics of both the LCW designs lie on par or exceed the

performance of on-chip LCWs reported so far. The fabrication complexity has been significantly lowered for the virtual channel design in part by the surface properties of the NPO films. The virtual channel LCWs are designed to be multi use devices. The absence of permanent bonding between the top and bottom substrates help for easy cleaning of the device after each operation.

## 6.2 Future research

### 6.2.1 Nanoparticle research

The method of fabrication of the NPO films is currently being applied to form fluorescent dielectric nanoparticles. Encapsulating fluorescent dye molecules within the nanoparticles is possible by introducing the dye during the formation of these nanoparticles. Preliminary results have shown that these nanoparticles are biocompatible and have high fluorescent intensities. Thus such nanoparticles can find applications as biomarkers for disease diagnosis. These nanoparticles will also be investigated for applications in dye sensitized solar cells.



**Figure 6-1. Dye incorporated organosilicate nanoparticles a. scraped from films treated to 150 C for 5 hrs, b. gelled solution.**

It has been observed that aging of the nanoporous organosilicate precursor solutions at ambient conditions results in the formation of gel with time. The gelation occurs within 7 days time and is strongly dependant on the amount of the evaporated solvent as well as the amount of  $-OH$  content in the PMSSQ starting material. Greater the amount evaporated, quicker the solution gels. Increased  $-OH$  content in the PMSSQ starting material results in a quicker gelling precursor solution. The gels have been dried to remove all the solvents and washed and filtered with ethanol to remove most of the PPG. These gels are later subjected to calcinations to result in a fine white powdery substance. When examined under a TEM, it has been formed that the white substance consists of a network of nanorods which can be separated if sonicated in a suspension. These nanorods will be investigated for use as bio scaffolds for tissue repair. Figure 6-2 gives the TEM of the obtained nanorods.

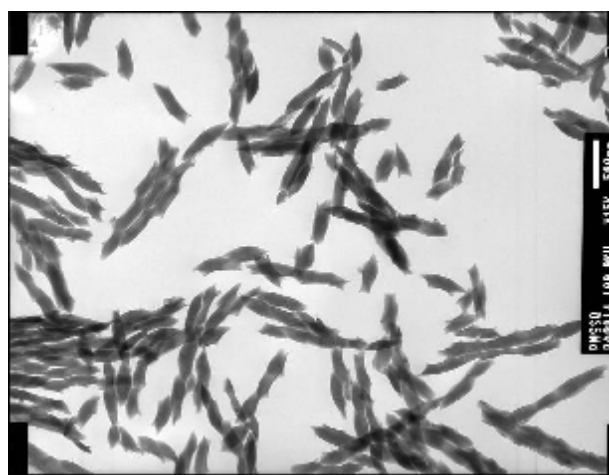


**Figure 6-2. TEM image of organosilicate nanorods**

### **6.2.2 Further improvements in LCW**

We are currently working on integrating solid core SU 8 waveguides with the ‘virtual channel’ design for better coupling of light into and out of the Liquid core waveguide channels. SU 8 spacers and the waveguides will be fabricated in a single lithographic exposure step. The SU 8 spacer thickness would eventually determine the thickness of the liquid core waveguide channel. A continuous flow liquid core waveguide will be the next step to study the fluorescent binding kinetics of fluorescently tagged antigen molecules binding with the immobilized antibody molecules on the NPO coating within the channels.

Also, we are currently working on an alternative fabrication method for the liquid core waveguide system using this method and want to apply this method for the inner coating of glass microchannels. Glass microchannels coated internally with this material can be utilized as the liquid (Aqueous) core waveguides.

# CHAPTER 7: OPTIMIZATION OF FABRICATION PROCESS FOR A PDMS-SOG-SILICON BASED PCR MICRO CHIP THROUGH SYSTEM IDENTIFICATION TECHNIQUES

## 7.1 Abstract

*A polymerase chain reaction (PCR) micro-chip with integrated thin film heaters and temperature detectors has been realized on a silicon-SOG-PDMS (poly-di(methyl) siloxane) platform. Accurate temperature sensing and control is important for a PCR reaction. This precludes the placement of the temperature sensor anywhere else but within the PCR chamber which can, in certain microchip designs complicate the fabrication methodology. This paper presents the design and optimal placement of a thin film resistance based temperature detector (RTD) for sensing of temperature response on the bottom of the chip (heater side) and predicting the temperature response on the top of the chip (PCR chamber side). Thermal modeling of the system has been performed using a parametric black-box approach based on the input-output data. From the steady state response of the system, Pseudo random binary sequences (PRBS) have been generated and used to excite it. Second and fourth order ARX (Auto regressive with exogenous inputs) models have been derived for optimal control and their performances have been compared. Reduction of fabrication complexity in regards to optimal placement of temperature sensor has been proposed.*

## 7.2 Introduction

Polymerase chain reaction (PCR) is a widely used technique for selective amplification of trace DNA segments [59]. It involves subjecting the DNA mix to three different temperatures (denaturation, annealing and extension) during multiple cycles. Motivation to reduce the sample volume, time of reaction and overall cost has led many

researchers to develop on-chip PCR systems[1,60,61]. Microchip PCR systems up to this date have witnessed three different design protocols. The first type of devices involved the use of a microchamber etched in polymer, glass or silicon with external heating sources like a conventional thermocycler[62] , Peltier heaters[63] , infra-red mediated heating [64] etc. These devices were not stand alone PCR microchips as the heaters and temperature sensors were not an integral part of the chip. The type II PCR devices were made on glass with three different constant heat zones with the PCR fluid rapidly being circulated among them [65]. Such devices eliminated the ramp up/down times during the thermal cycles at the expense of complex microfluidic designs. Furthermore, these devices required good thermal isolation from one heating zone to the other which further complicated the fabrication process. The third type has focused on confining a microfluidic volume of PCR mix to a single chamber with an integrated heater/ temperature sensor assembly on the same chip with external control to achieve rapid thermal cycling [66,67,68]. In type 3 devices, three different configurations with respect to the placement of heaters/temperature sensors were considered. Wolff et al [66] demonstrated a PCR device in which the heaters and temperature sensors are placed on the chamber side of the device. A 5 micron SU 8 layer isolates the heaters/temperature sensor from the PCR mix. Lagally et al [67] demonstrated a portable PCR chip in which the heaters are fabricated on the reverse side of the device and the temperature sensors within the PCR chamber. Yoon et. al [68] demonstrated a PCR device in which the chamber was etched into the silicon from the top side and the heaters/ temperature sensors were placed on the back side of the device.

Our group has previously reported an optimization scheme for the design and fabrication of a prototype using a glass-housed thermocouple integrated into a PDMS-SOG-Silicon made PCR chamber [69]. The aim of this paper is to present the integration of the RTD into this on-chip device, thus eliminating the need for the thermocouple. One of the major challenges has been an optimal placement of this RTD in the system. In the current configuration, the heaters are placed in the bottom of the chip and the sensing RTD is on the top surface. Our goal is to place the RTD on the bottom surface to simplify the overall fabrication process. For a desired control of the top-surface temperature as defined by the PCR process from the response of RTD situated at the bottom, we have performed parametric identification of the system based on the input-output data collected from thermal experiments. This helps us design an optimal thermal control system. A mathematical relation between the temperatures on either sides of the chip has been modeled. We envisage using this model for thermal control for our future prototypes.

### **7.3 Device details**

Essentially, the device consists of a replica molded PDMS chamber (volume = 3  $\mu$ l) with a set of inlet/outlet ports irreversibly bonded to an oxidized silicon substrate with an intermediate spin on glass (SOG) layer. Oxygen plasma bonding technique was used to bond PDMS to SOG coated silicon substrate [69]. Thin film serpentine platinum heaters were designed and patterned on the bottom surface of a silicon substrate Figure 7-1 shows the schematic of the device.

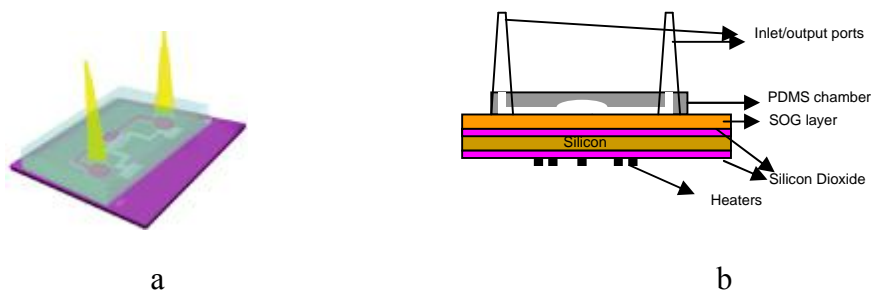


**Figure 7-1. Schematic of the device, b. cross-sectional view of the device.**

### **7.3.1 Integration of the RTD**

#### **7.3.1.1 RTD fabrication**

The patterning and fabrication of the RTD is done by conventional microfabrication techniques. A 700 microns thick double side polished silicon wafer is first cleaned rinsed with acetone, Methanol and Isopropyl alcohol in the order to remove the surface bound organics. A 700 nm thick silicon dioxide is then sputter coated both polished surfaces of the substrate to act as the insulation between the substrate itself and the heaters and RTD. 10 nm thick Titanium layer is then sputter followed by 180 nm thick platinum on either side of the substrate. The substrate is then annealed under vaccum ( $10^{-6}$  torr) at 450 C for 24 hours prior to using the substrate for PCR chip fabrication. Annealing of the platinum film is a crucial step in the fabrication of the RTD. Low temperature deposition of platinum films results in misaligned islands or grains leading to intrinsic stresses in the as – deposited films [70,71]. This leads to erratic resistance jumps and a good calibration curve cannot be obtained. High temperature annealing of these films helps reduce those stresses by re-aligning the mismatched grains.

The patterning of the platinum films for heaters and RTD is done by conventional photolithographic process. AZ nLOF 2020 (Clariant AZ Electronic Materials, negative photoresist) is used as the photoresist. The photoresist is first spun coated at 3000 rpm for 30 s followed by a pre bake at 110 C for 60s. OAI Mask aligner is used for UV exposure. The mask design for the RTD is shown in Figure 7-2.

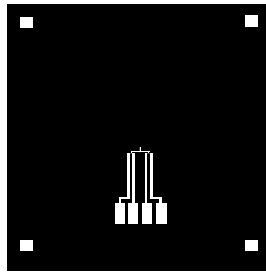


Figure 7-2. Mask design for the RTD

### 7.3.1.2 Placement considerations for the RTD

The placement of the RTD plays an important role as it has a direct effect on the overall sensitivity of the device. Different configurations of the RTD with respect to the heaters have been investigated. Following lists the arrangements.

#### 1. Heater and RTD on the back side, chamber on the front side.

Calibration of the RTD was performed with the thermocouple placed on the top-surface. The chip was heated using the heaters by supplying a voltage in steps of 5 V. The temperature read out of thermocouple and the resistance of the RTD was taken at steady state. This measurement yielded a highly nonlinear curve as there was a finite delay between the temperature on the heater side and the chamber side. Hence this arrangement was not the optimal arrangement for the PCR reaction.

#### 2. Heater, RTD and chamber on the same side

Although this arrangement is convenient because the heaters are on the top surface thus eliminating the delay in the ramp times of the device, it resulted in cracking of the SOG film. This resulted in an erratic resistance read out of the RTD and the calibration was not successful.

3. *Heaters on the bottom side, RTD and chamber on the top side.*

This arrangement gave a good correlation between the temperature of the chamber and the resistance of the RTD. Calibrations were performed with the thermocouple placed on top surface close to the RTD. Figure 7-3 shows a plot of the resistance Vs temperature.

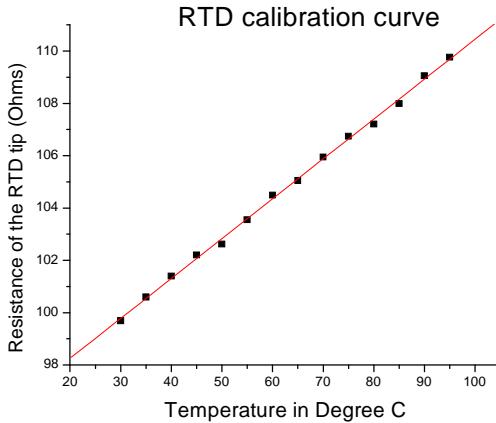


**Figure 7-3. RTD calibration curve in arrangement 3**

*Thermal control using RTD on top surface (configuration 3):*

Currently, we have used configuration 3 for realization of our device. The RTD has been designed and used in the 4 wire measurement mode to minimize the measurement errors due to lead resistances. Figure 7-4 shows the mask design and the temperature sensing in the 4 wire measurement mode using the RTD. A constant current of 1 mA was

passed through the outer leads and the voltage measurements were made across the inner leads of the RTD.

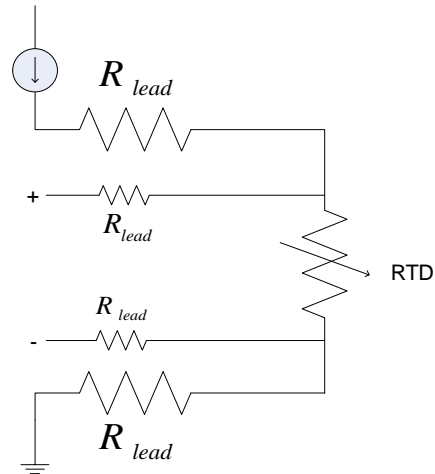


**Figure 7-4. Schematic for the 4-wire measurement**

### 7.3.2 PCR Runs

To test the fabricated device, 527-bp DNA of Infectious Bovine Rhinotracheitis (IBR) virus was used as a test assay for on chip studies. The PCR amplification was performed on chip with the RTD as the temperature sensor for two different template concentrations. A template DNA (7 ng/ $\mu$ l) and another one diluted to 100,000:1 with RNase free water were amplified on the micro-chip. Figure 7-5 shows the Slab-gel electrophoresis result for the amplified samples.

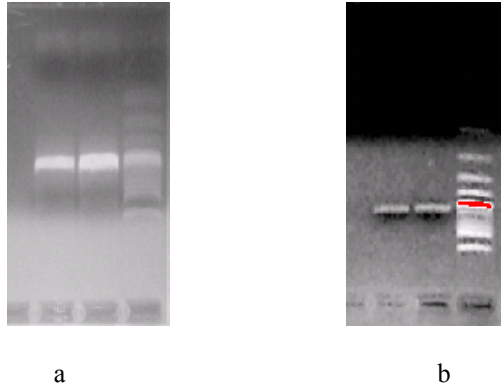


**Figure 7-5. Results of the PCR amplifications a. 1:1 sample, b. 100,000:1 sample**

#### **7.4 Parametric identification of the System**

Parametric identification of the system was performed using the ARX model assuming the system to be linear. The linearity of the system was investigated by providing three different linearly scaled voltage inputs. The corresponding temperature of the system was recorded. The steady state temperature was observed to be scaled up by the same amount as the voltage steps hence confirming the linearity. Figure 7-6 gives the plot of the step temperature responses on the heater side and the chamber side of the device. On-chip RTDs fabricated on both top and bottom surfaces were calibrated and used as temperature sensors. A LabVIEW (National Instruments) code was used to control the application of voltage as well as to acquire the temperature data.

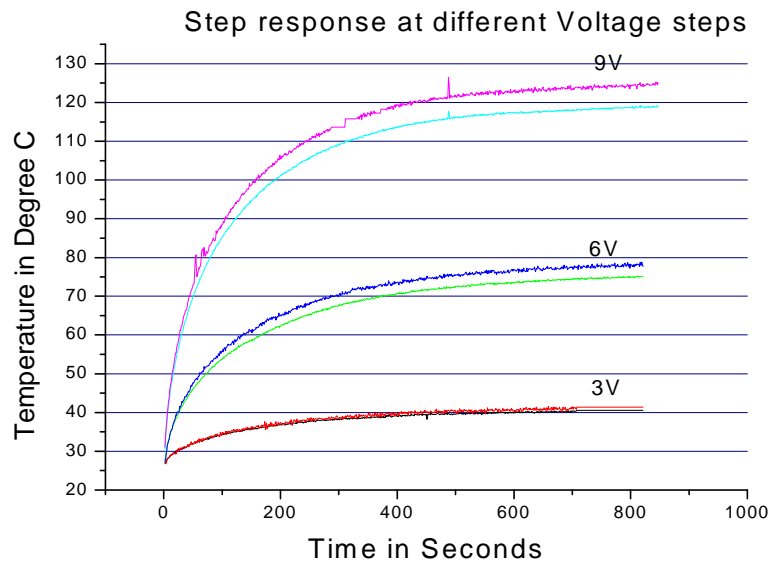


**Figure 7-6. Temperature responses to different voltage steps. At each voltage step, the temperature of the chamber lies above the temperature of the heater.**

#### **7.4.1 Design of the perturbation signal**

Extraction of model parameters using the black-box technique requires the excitation of the system with a perturbation signal and recording the output values [72]. The perturbation signal should ideally have an autocorrelation function similar to white noise [73]. A pseudo – random – binary sequence (PRBS) was chosen as the perturbation signal. The bit width for the PRBS signal was calculated from the estimated 3 dB bandwidth of the system. A voltage step of 7.5V was given to the system and the temperature response was recorded. An exponential curve was fitted to this response and the major time constants of the system were obtained. Figure 7-7 shows the step response to a 7.5 V step and the curve fit. The bit width was calculated as

$$t_{bitwidth} = \frac{2p}{3B}$$

7-1

$$B = \frac{1}{t}$$

7-2

where ‘B’ is the 3dB bandwidth of the system estimated from the temperature step response and ‘τ’ is the time constant. The following exponential equation was used to fit the data for the obtained step responses on the top and bottom surfaces. Table. 1 lists the curve fit parameters for these responses.

$$T = T_{\max} (1 - e^{-(t+t_0)/t})$$

7-3

**Table 7-1. Curve fit parameters**

	$T_{\max}$	$t_0$ (Seconds)	$t$
Heater Side	99.28	132	69.57
Chamber Side	95.17	136	74.81

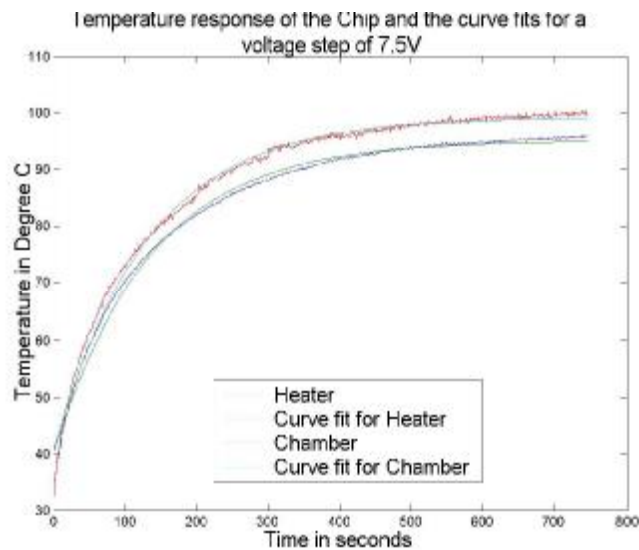


**Figure 7-7. Step response with an input voltage step of 7.5 V for the heater and chamber temperature and the corresponding curve fits**

A 7<sup>th</sup> order modulo-2 primitive polynomial was chosen for the generation of the PRBS signal. The output from the LabVIEW DAQ card was used to control the turn on/off times of the supply to the heater. The representative circuit diagram for the experimental set-up is shown in Fig 7. A 7.5 V D.C supply was used and the duty cycle

of the counter was switched between 1 and 0.25 corresponding to voltage values of 7.5V and 1.85 V. A duty cycle of 0.25 and 1 corresponded to a steady state chamber temperature of 60 °C and 96 °C respectively. Thus, the temperature of the chamber was switched between 96 and 60 °C [temperature range of interest for any standard PCR cycle] [66].

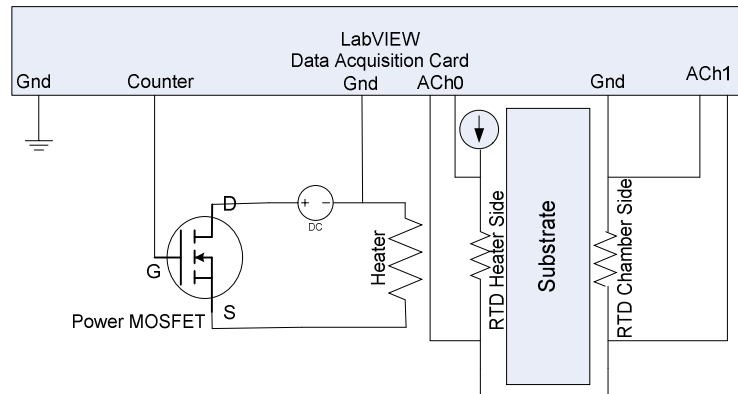


**Figure 7-8. Circuit diagram for the experimental set up**

Figure 7-9 gives the PRBS response of the system

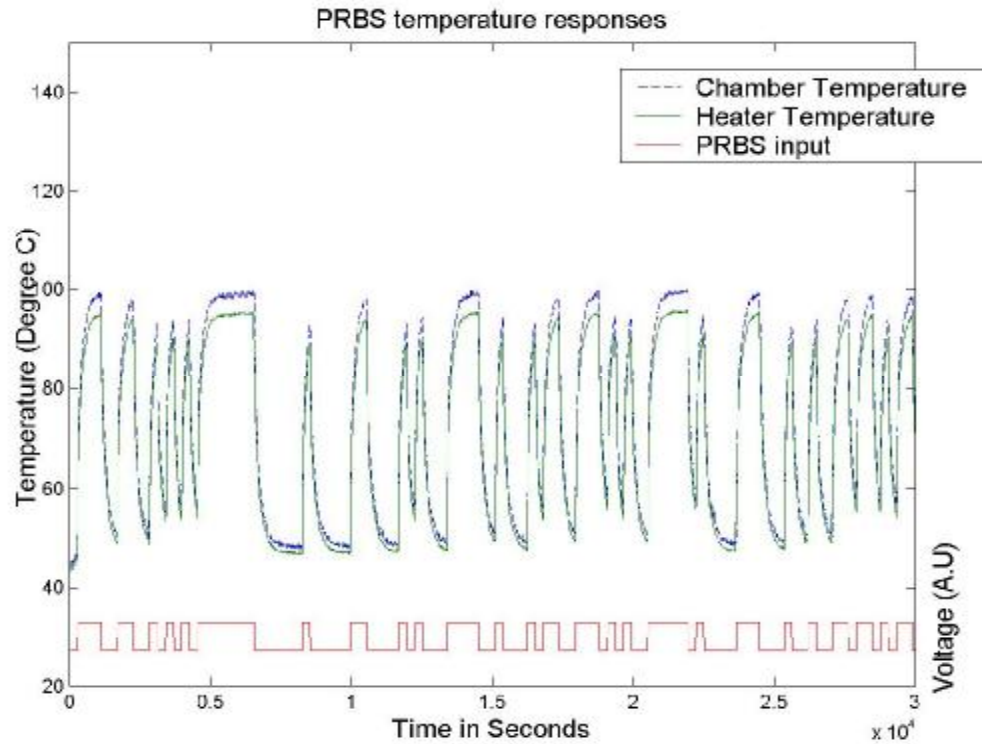


Figure 7-9. PRBS temperature response of the heater side and the chamber side

#### 7.4.2 Identification of the model parameters

The D.C component from the output response and the PRBS voltage input was removed by subtracting both these signals from their corresponding mean values prior to performing the parametric fits. Different order ARX models have been identified based on the PRBS input-output data. We observed a decrease in the mean squared error between the simulated and the experimental responses as the model order was increased.

#### 7.5 Results and discussion

Figure 7-10 gives the simulated data with a second order and a fourth order models for the chamber temperature. The mean squared error (MSE) for the second order model

was calculated to be 7.2691, while the MSE for the fourth order model was obtained to be 5.2924. The second order ARX model obtained can be presented by

$$A(q^{-1})y_{ch}(k) = B(q^{-1})U(k)$$

7-4

where

$$A(q^{-1}) = 1 - 0.8163 q^{-1} - 0.07538 q^{-2}$$

$$B(q^{-1}) = 0.8475 q^{-1}$$

The obtained parameters for the fourth order model were

$$A(q^{-1}) = 1 - 0.7508 q^{-1} + 0.00199 q^{-2} \\ + 0.06221 q^{-3} - 0.1781 q^{-4}$$

$$B(q^{-1}) = 1.087 q^{-1}$$

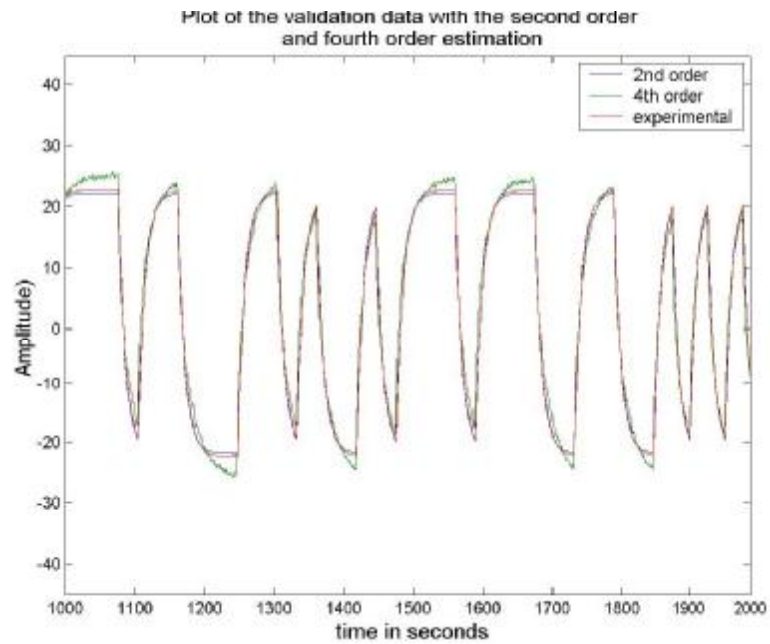


**Figure 7-10. Plot of the simulated response with second order model and fourth order model and the experimental data**

### 7.5.1 Reduction of fabrication complexity

In addition to the identification of the system parameters, a relation was derived between the chamber temperature and the heater temperature. This would facilitate the placement of the RTD on the bottom surface (heater side), thus significantly simplifying the fabrication process for the PCR microchip. The obtained PRBS responses for the bottom and the top surface temperatures were used and different models were assumed to fit the input- output relations using the least squares method. It has been observed that the relation between the chamber temperature and the temperature on the heater side can be accurately modeled by a simple first order equation. The model obtained can be described mathematically as

$$T_{\text{chamber}} = 1.049T_{\text{heater}} - 0.7748 \quad 7-5$$

This equation has been used to predict the chamber temperature from the temperature measured on the heater side. Figure 7-11 gives a plot of the predicted and the measured chamber temperature values.

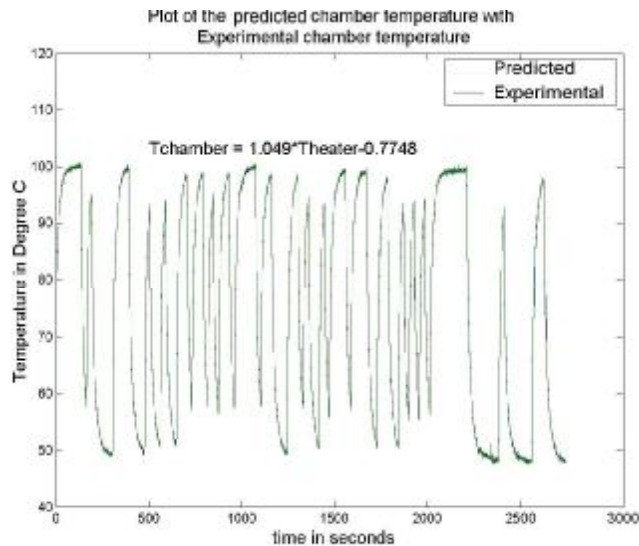


Figure 7-11. Plot of the predicted and the measured chamber temperature values

## 7.6 Conclusions and Future work

A PDMS-SOG-Silicon based micro-chip PCR system with integrated thin film heaters and temperature sensors has been presented. Various placements of the RTD have been investigated so as to obtain a linear correlation between the temperature of the chamber and the resistance of the RTD. Parametric identification of the system has been performed by ARX method and 2<sup>nd</sup> order and 4<sup>th</sup> order models have been derived. A method has been proposed to reduce the complexity of the fabrication process by deriving a relation between the chamber and the heater temperature. For the future work, an optimal control system will be designed based on the identified model and the RTD will be placed on the heater side. An attempt will be made to derive the heat transfer model using the bond-graph approach.

## References

- [1] Schmidt, W. (2005). *Optical Spectroscopy in Chemistry and Life sciences – An Introduction*, Wiley- VCH Verlag GmbH & Co. KGaA.
- [2] Jacco van Rheenen, M. L., and Kees Jalink (2004). "Correcting Confocal Acquisition to Optimize Imaging of Fluorescence Resonance Energy Transfer by Sensitized Emission." *Biophysical Journal* 86: 2517–2529.
- [3] Lakowicz, J. R. (1999). *Principles of Fluorescence Spectroscopy*. New York, Kluwer Academic/Plenum.
- [4] Mary E. Pierce, S. A. G. (2004). Development of a FRET based fiber-optic biosensor for early detection of myocardial infarction. Proceedings of the 26th Annual International Conference of the IEEE EMBS, San Francisco, CA, USA, IEEE.
- [5] Sungho Ko, S. A. G. (2006). "A novel FRET-based optical fiber biosensor for rapid detection of *Salmonella typhimurium*." *Biosensors and Bioelectronics* 21: 1283–1290.
- [6] Teng-Leong Chew, W. A. W., Patricia J. Gallagher, Fumio Matsumura, and Rex L. Chisholm (2002). "A fluorescent resonant energy transfer-based biosensor reveals transient and regional myosin light chain kinase activation in lamella and cleavage furrows." *The Journal of Cell Biology* 156(3): 543–553.
- [7] Xu, Juntao, Grant, Sheila A, "FRET-based biosensors to detect infectious agents", Proc. SPIE Vol. 4578, , Fiber Optic Sensor Technology and Applications, p. 108-116, 2001
- [8] N.S. Kapany, "Fiber Optics – Principles and Applications" Academic Press, New York, 1967
- [9] R. Altkorn, I. Koev, R. P. Van Duyne, and M. Litorja, "Low-loss liquid-core optical fiber for low refractive-index liquids: fabrication, characterization, and application in Raman spectroscopy" *APPLIED OPTICS* Vol. 36, No. 34, December 1997, 8992 - 8998
- [10] K. Tsunoda, A. N., J. Yamada, and S. Nishi, (1989). "The possibility of signal enhancement in liquid absorption spectrometry with a long capillary cell utilizing successive total reflection at the outer cell surface." *Appl. Spectrosc.* 43: 49–55
- [11] T. Wang, J. H. Aiken, C. W. Huie, and R. A. Hartwick, "Nanoliter-scale multireflection cell for absorption detection in capillary electrophoresis," *Anal. Chem.* 63, 1372–1376, 1991
- [12] K. Tsunoda, A. Nomura, J. Yamada, and S. Nishi, "Long capillary cell with the use of successive total reflection at outer cell surface for liquid absorption spectrometry," *Anal. Sci.* 4, 321– 323 ,1988.

- [13] E. P. Ippen, "Low-power quasi-cw Raman oscillator," *Appl. Phys. Lett.* 16, 303–305, 1970
- [14] G. E. Walrafen and J. Stone, "Intensification of spontaneous Raman spectra by use of liquid core optical fibers," *Appl. Spectrosc.* 26, 585–589 ~1972!
- [15] P. Dasgupta, Z. Genfa, S. Poruthoor, S. Caldwell, S. Dong, and S. Liu, "High-sensitivity gas sensors based on gas-permeable liquid core waveguides and long-path absorbance detection," *Anal. Chem.* 70, 4661–4669, 1998.
- [16] P. Dasgupta, G. Zhang, J. Li, C. Boring, S. Jambunathan, and R. Al-Horr, "Luminescence detection with a liquid core waveguide," *Anal. Chem.* 71, 1400–1407 (1999).
- [17] P. Dress and H. Franke, "Increasing the accuracy of liquid analysis and pH-value control using a liquid-core waveguide," *Rev. Sci. Instrum.* 68, 2167–2171 (1997).
- [18] P. Dress and H. Franke, "A cylindrical liquid-core waveguide," *Appl. Phys. B* 63, 12–19 (1996).
- [19] A. Datta, I. Eom, A. Dhar, P. Kuban, R. Manor, I. Ahmad, S. Gangopadhyay, T. Dallas, M. Holtz, F. Temkin, and P. Dasgupta, "Microfabrication and characterization of Teflon AF-coated liquid core waveguide channels in silicon," *IEEE Sensors Journal*, 3, 788–795 (2003).
- [20] R. Manor, A. Datta, I. Ahmad, M. Holtz, S. Gangopadhyay, and T. Dallas, "Microfabrication and characterization of liquid core waveguide glass channels coated with Teflon AF," *IEEE Sensors Journal* 3, 687–692 (2003).
- [21] W. P. Risk, H.-C. Kim, R. D. Miller, H. Temkin, S. Gangopadhyay, "Optical Waveguides with an aqueous core and a low index Nanoporous cladding"
- [22] W. P. Risk, H.-C. Kim, R. D. Miller, H. Temkin and S. Gangopadhyay, *Optics Express*, 12(26), 6446 (2004)
- [23] Li JJ, Xu XY, Jiang Z, Hao ZP and Hu C, *Environ Sci Technol.* 39(5):1319 (2005)
- [24] Maex. K, Baklanov M. R, Shamiryan. D, Lacopi. F, Brongersma S. H, Yanovitskaya Z. S, *J. Appl. Phys.* 93, 8793 (2003).
- [25] Narayan K. Raman, Mark T. Anderson, C. Jeffrey Brinker., "Template Based Approaches to the preparation of Amorphous Nanoporous Silicas" *Chem. Mater.* 1996, 8, 1682-1701

- [26] J. S. Beck, J. C. Vartuli, W. J. Roth, M. E. Leonowicz, C. T. Kresge, K. D. Schmitt, C. T.-W. Chu, D. H. Olson, E. W. Sheppard, S. B. McCullen, J. B. Higgins, and J. L. Schlenker, "A New Family of Mesoporous Molecular Sieves Prepared with Liquid Crystal Templates" *J. Am. Chem. Soc.* 1992, 114, 10834-10843
- [27] *Maryanne M. Collinson*, "Sol-Gel Strategies for the Preparation of Selective Materials for Chemical Analysis" *Critical Reviews in Analytical Chemistry*, 29(4):289–311 (1999)
- [28] Sakka, S.; Kamiya, K. *J. Non-Crystalline Solids*. 1982, 48, 31.
- [29] S. Sakka, in: *Better Ceramics Through Chemistry*, eds. C.J. Brinker, D.E. Clark, and D.R. Ullrich, (Elsevier-North Holland: New York, 1984) p. 91.
- [30] Brinker, C. J., Hurd, A. J., Schunk, P. R., Frye, G. C. & Ashley, C. S. "Review of sol-gel thin film formation." *J. Non-Cryst. Solids* 147, 148, 424–436 (1992).
- [31] David Gross, Florence Cagnol, Galo J. de A, A. Soler Illia, Eduardo L. Crepaldi, Heinz Amenitsch, Aline Brunet – Brineau, Alexi Burgeois, Clement Sanchez, "Fundamentals of mesostructuring through Evaporation Induced Self assembly", *Adv. Funct. Mater*, 2004, 14, 310 – 322.
- [32] Qingguo Wu, April D. Ross and Karen K. Gleason, *Plasma Process. Polym.* **2**, 401 (2005)
- [33] Moonhor Ree, Jinhwan Yoon and Kyuyoung Heo, "Imprinting well-controlled closed-nanopores in spin-on polymeric dielectric thin films" *J. Mater. Chem.*, 2006, 16, 685–697
- [34] J. J. Si, H. Ono, K. Uchida, S. Nozaki, and H. Morisaki, "Correlation between the dielectric constant and porosity of nanoporous silica thin films deposited by the gas evaporation technique" *Appl. Phys. Lett.*, Vol. 79, No. 19, 5 November 2001
- [35] Shinji Nozaki, Hiroshi Ono, Kazuo Uchida, Hiroshi Morisaki, Nobuo Ito, and Masaki Yoshimaru, "Ultralow K Nanoporous Silica by Oxidation of Silicon Nanoparticles" *Interconnect technology conference, proceedings of the IEEE 2002 International*.
- [36] Presentation Speech by Professor Stig Claesson of the Royal Academy of Sciences while awarding a nobel prize to Dr. Paul Flory, 1974.
- [37] Guido Raos and Giuseppe Allegra, "Macromolecular clusters in poor-solvent polymer solutions" *J. Chem. Phys.* 107 (16), 1997 6479-6490.

- [38] Matthias Schmidt and Alan R. Denton, "Demixing of colloid-polymer mixtures in poor solvents", *PHYSICAL REVIEW E*, VOLUME 65, 061410, 2002
- [39] Hiroshi Yabu, Takeshi Higuchi, Kuniharu Ijro, Masatsugu Shimomura, "Spontaneous formation of polymer nanoparticles by good-solvent evaporation as a nonequilibrium process" *CHAOS* 15, 047505, 2005
- [40] T. Rajagopalan, B. Lahlouh, J. A. Lubguban, N. Biswas, S. Gangopadhyay, J. Sun, D. H. Huang, S. L. Simon A. Mallikarjunan, H.-C. Kim, W. Volksen, M. F. Toney, E. Huang, P. M. Rice, E. Delenia, and R. D. Miller, "Super critical Carbon di Oxide extraction of porogens for the preparation of ultra-low dielectric constant films", *APPLIED PHYSICS LETTERS* VOLUME 82, NUMBER 24 16 JUNE 2003
- [41] Yunfeng Lu, Rahul Ganguli, Celeste A. Drewien, Mark T. Anderson, C. Jeffrey Brinker, Weilang Gong, Yongxing Guo, Hermes Soyez, Bruce Dunn, Michael H. Huang, Jeffrey I. Zink "Continuous formation of supported cubic and hexagonal mesoporous films by sol-gel dip-coating" *NATURE* |VOL 389 | 25 SEPTEMBER 1997
- [42] The substrates were rinsed in Acetone, methanol, Isopropyl alcohol and DI water in the given order. The rinsed substrates were air dried by blowing air from a compressed air supply. The substrates were visibly examined to see the presence of any dust particles. The procedure was repeated if there was any particulate matter present on the substrate surface.
- [43] Thomas M.H. Lee, Debbie H.Y. Lee, Connie Y.N. Liaw, Alex I.K. Lao, I-Ming Hsing, "Detailed characterization of anodic bonding process between glass and thin-film coated silicon substrates" *Sensors and Actuators* 86, 2000.103–107
- [44] D. I. Pomerantz, US Patent No. 3,397,287 ~1968!, US Patent No. 3,417,459 (1968).
- [45] H. J. Quenzer, C. Dell, B. Wagner, "Silicon - Silicon anodic-bonding with intermediate glass layers using spinon glasses", *IEEE* 1996.
- [46] The glass etching solution is prepared in the following ratio by volume, 85% Sulfuric acid, 0.8% HF in DI water. The mixture is heated 45 °C and the patterned substrates are immersed in this solution. The etch rate of borosilicate glass for this composition was 0.22 microns/min.
- [47] Arindom Datta, I.-Y. E., Achintya Dhar, Petr Kuban, Rosalynn Manor, Iftikhar Ahmad, Shubhra Gangopadhyay, and M. H. Tim Dallas, Henryk Temkin, (2003). "Microfabrication and Characterization of Teflon AF-Coated Liquid Core Waveguide Channels in Silicon." *IEEE SENSORS JOURNAL* 3(6): 788-795.

- [48] Rosalynn Manor, A. D., Iftikar Ahmad, Mark Holtz, Shubhra Gangopadhyay, and Tim Dallas (2003). "Microfabrication and Characterization of Liquid Core Waveguide Glass Channels Coated With Teflon AF." *IEEE SENSORS JOURNAL* 3(6): 687-692.
- [49] Sears, Zemansky and. Young. (1987). *College Physics*, Addison Wesley Publishing Company.
- [50] Adamson, A. W. (1960). *Physical Chemistry of Surfaces*, Interscience Publishers, Inc.
- [51] Bin Zhao, J. S. M., David J. Beebe (2001). "Surface-Directed Liquid Flow Inside Microchannels." *Science* 291: 1023-1026
- [52] T. C Ku, J. H. Ramsey, W. C. Clinton (1968). "Calculation of Liquid Droplet Profiles from Closed - Form Solution of Young-Laplace Equation." *IBM J. Res. Develop.*: 441-447.
- [53] "Teflon AF Amorphous Fluoropolymers," (1989) DuPont Fluoroproducts, Wilmington, DE, H-16 577-1
- [54] Christopher M. Stafford, Christopher Harrison, Kathryn L. Beers, Alamgir Karim, Eric J. Amis, Mark R. Vanlandingham, Ho-Cheol Kim, Willi Volksen, Robert D. Miller, Eva E. Simony, *Nature Mat.* Vol 3. 2004. 545.
- [55] Thin NPS solution was prepared by mixing 30:70 solution of PMSSQ : PM Acetate (Solution A) and 30:70 solution of PPG : PM Acetate (Solution B). Solution A and B were mixed in 50 : 50 ratio by weight.
- [56] The films were exposed to a low power oxygen plasma of 12 W with the following parameters - oxygen flow was kept at 180 SCCM, base pressure of 900 mTorr. The exposure was performed for 55 seconds.
- [57] Tim Dallas, Purnendu. K. Dasgupta. (2004). "Light at the end of the tunnel: recent analytical applications of liquid-core waveguides." *Trends in Analytical Chemistry* 23(5): 1-8.
- [58] Kasap, S. O. (2001). *Optoelectronics and Photonics Principles and Practices*. NJ, Prentice Hall.
- [59] M.A. Northrup, "DNA Amplification with a microfabricated reaction chamber", in the digest of technical papers of the 7th International conf. on the Solid State Sensors & actuators, *Transducers 93*, Yokohama, Japan, pp.924-926, 1993.
- [60] P.J. Obeid, T.K. Christipoulos, H.J. Crabtree and C.J. Backhouse, "Microfabricated Device for DNA and RNA amplification by continuous-flow polymerase chain reaction and reverse transcription-polymerase chain reaction with cycle no. selection", *Analytical Chemistry*, Vol.75, pp.288-295, 2003.

- [61] J. Lu, M. Enzelberger and S. Quake, "A nanoliter rotary device for polymerase chain reaction", *Electrophoresis*, Vol. 23, pp. 1531-1536, 2002.
- [62] J. Cheng, L. Walters, P. Fortina, G. Hvichia, S. Jacobson, J. Ramsey, L. Kricka, and P. Wilding, "Degenerate Oligonucleotide primed polymerase chain reaction and capillary electrophoretic analysis of human DNA on microchip based devices", *Analytical Biochemistry*, Vol. 257, pp. 101-106, 1998.
- [63] J. Khandurina, T. McKnight, S. Jacobson, L. Waters, R. Foote, and J. Ramsey, "Integrated system for rapid PCR-based DNA analysis in microfluidic devices", *Analytical Chemistry*, Vol. 72, pp. 2995-3000, 2000.
- [64] B.C. Giordano, J. Ferrance, S. Swedberg, A.F.R. Huhmer, and J.P. Landers, "Polymerase chain reaction in polymeric microchips: DNA amplification in less than 240 secs.", *Analytical Biochemistry*, Vol. 291, pp. no. 124-132, 2001.
- [65] M. Kopp, A. deMello, and A. Manz, "Chemical amplification: continuous flow PCR on a chip", *Science*, Vol. 280, pp. 1046-1048, 1998.
- [66] J. El -Ali, I.R. Perch- Nielsen, C.R. Poulsen, D.D Bang, P. Telleman, A. Wolff, "Simulation and experimental validation of a SU-8 based PCR thermocycler chip with integrated heaters and temperature sensor ", *Sensors and Actuators A* Vol 110, pp 3-10, 2004.
- [67] E. Lagally, P. Simpson, and R. Mathies, "Monolithic integrated microfluidic DNA amplification and capillary electrophoresis analysis system", *Sensor Actuator B-chemistry*, Vol. 63, pp. 138-146, 2000.
- [68] Dae Sung Yoon<sup>1</sup>, You-Seop Lee<sup>2</sup>, Youngsun Lee, Hye Jung Cho, Su Whan Sung, KwangWO<sup>1</sup>, Junhoe Cha<sup>1</sup> and Geunbae Lim, "Precise temperature control and rapid thermal cycling in a micromachined DNA polymerase chain reaction chip " *J. Micromech. Microeng.* Vol. 12, pp813-823, 2002
- [69] S.Bhattacharya, Y.Gao, V.Korampally, M.T. Othman, S.A. Grant, S.B Kleiboeker, K.Gangopadhyay, S. Gangopadhyay, "Optimization of design and fabrication process for realization of a PDMS-SOG-Silicon DNA amplification chip", submitted after 1<sup>st</sup> review, *Journal of MEMS*.
- [70] J. D. Wrbanek, K. L. H. Laster, "Preparation and Analysis of Platinum thin films for High temperature sensor applications" NASA TM - 2005 - 213433.
- [71] L.C. Martin and R. Holanda, "Applications of Thin Film Thermocouples for Surface Temperature Measurement," *Conference on Spin-Off Technologies for*

Commercial Sensors and Scientific Instrumentation (San Diego, CA, July 24–29, 1994), NASA TM-106714.

[72] Huaiyu Wu, Dong sun, Zhaoying Zhou, “Model Identification of a Micro Air Vehicle in Loitering Flight Based on Altitude Performance Evaluation”, IEEE Transactions on Robotics, Vol. 20, No. 4, pp.702-712, 2004.

[73] M. W. Braun, D. E. Rivera A. Stenman, W. Foslien, and C. Hrenya, “Multi-level Pseudo-Random Signal Design and “Model-on-Demand” Estimation Applied to Nonlinear Identification of a RTP Wafer Reactor ”, Proceedings of the American control conference, San Diego, California , pp 1573-1577, 1999.

## **VITA**

Venumadhav Korampally was born on July 17, 1979 in Karimnagar, Andhra Pradesh, India. He received his B. Tech degree in Electrical Engineering from Kakatiya University, Warangal, India in 2000 and M.S degree in Electrical Engineering from the University of Missouri-Columbia in 2004. He will be receiving his Ph.D in Electrical Engineering from the University of Missouri-Columbia in December 2007. His current research interests include development and integration of nanomaterials with MEMS based technologies, nanoparticles for targeted drug delivery and the development of microfluidic platforms for biosensor applications.